8-23-2017

Development of Radar Absorbing Materials (RAMs) based on Nano-Structured Magnetic Materials and Applications

Ahmet Teber
University of Connecticut - Storrs, ahmet.teber@uconn.edu

Development of Radar Absorbing Materials (RAMs) based on Nano-Structured Magnetic Materials and Applications

Ahmet Teber, Ph.D.

University of Connecticut, 2017

ABSTRACT

There has been a long-standing interest in the development of radar absorbing materials (RAMs) for military applications such as microwave absorbers for stealth technology, anechoic chambers, and morphing scenarios, as well as camouflaging ground-based hardware against airborne radar observation. Even so, there remain outstanding challenges in this area such as the selection of suitable material compositions, the available frequency bandwidth, and the required thickness of the materials.

The properties of materials at the nano-scale can change significantly. With only a reduction in size (no change in the substance itself), materials can exhibit new properties such as electrical conductivity, insulating behavior, and greater reactivity, characteristics that the same substance does not display at the micro/macro-scale. In addition, interactions at the interfaces of phases improve substantially when the dimensions reach the nanometer dimensions. That is very important to enhance material properties. Composite materials are multi-phased compositions of two or more components, which obtain new characteristic properties. They usually consist of a certain host matrix containing one or more fillers, which can be made up of nanoparticles/fibers. Many efforts by researchers have been made in recent years using novel nanoscience improvements in order to get nanostructured materials with enhanced performance.

Ahmet Teber- University of Connecticut, 2017

In this work, we investigate several approaches to design nano-structured composite materials, which would behave as suitable absorbers for normally indcident electromagnetic plane waves, and to enhance these properties consistent with the radar frequency bands. The thesis provides a useful sample of contemporary research activities in this field. It includes the related theory, fabrication, and characterization of various type of nanocomposites.

Development of Radar Absorbing Materials (RAMs) Based on Nano-structured Magnetic Materials and Applications

Ahmet Teber

B.A., Kocaeli University, TR, 2005

M.A., Gebze Institute of Technology, TR, 2010

A Dissertation

Submitted in Partial Fulfillment of the

Requirements for the Degree of

Doctor of Philosophy

at the

University of Connecticut

2017

APPROVAL PAGE

Doctor of Philosophy Dissertation

Development of Radar Absorbing Materials (RAMs) Based on Nano-structured Magnetic Materials and Applications

Presented by

Ahmet Teber, B.A., M.A.

Major Advisor

_____

Rajeev Bansal

Associate Advisor

_____

Helena Silva

Associate Advisor

_____

Ali Gokirmak

University of Connecticut
2017

Acknowledgments

I am grateful to all the people who contributed in some way to the work described in this thesis. Primarily, I would like to express my most sincere gratitude to my major academic advisor Dr. Rajeev Bansal, Professor & Department Head of Electrical and Computer Engineering at the University of Connecticut, for his many contributions, guidance and mentorship in the completion of this thesis. He always helped and answered my questions patiently, whenever or wherever I stopped by. I take him as an admirable example for my academic career. During my most difficult times, he gave me the moral support and the freedom I needed to continue.

I would also like to thank my associate advisors, Dr. Helena Silva and Dr. Ali Gokirmak, for their valuable feedback and suggestions on my thesis work. I would like to thank them for friendship throughout my Ph.D. program, spending their valuable time and building a very comfortable and friendly research environment, opening their house to me, cooking and sharing meals their three daughters Sofia, Aida and Mina, who have joined us over the years of my Ph.D.

I would like to acknowledge a special thanks to my mother, Fatma, and my father, Saim, my siblings, Kevser, Cigdem, and Sefa, Sefa`s wife, Zubeyde as well as my little nephews Yavuz Alp, M. Arda, and M. Emin for their endless love, support, confidence and patience throughout my education. Words cannot express how grateful I am for all of the sacrifices that they have made on my behalf. Then prayer for me was what sustained me thus far.

During my Ph.D., I met talented people, professionally and personally. I would like to thank friends from the Electronic, Photonics, and Bio-photonics group at Uconn: Lhacene Adnane (for his valuable help and contributions on measurements in the Biotechnology Bio-services Center, Uconn), Turgut Yilmaz (for his valuable help and contributions on measurements in the Department of Physics, Uconn), Kevin Kiarash Ahi (for his friendship and discussions at conferences where we met), Gokhan Bakan, Kadir Cil, and Faruk Dirisaglik (for his help on lab training and on the measurement setups). I also thank Phuong Ha Nguyen (for his cheerful conversations as an officemate and his contributions to theoretical issues in computation), Aaron Ciardullo, Jake Scoggin, Sadid Muneer and his wife Nafisa Noor as well as Adam Cywar (for working together as teaching assistants). I would like to thank each of them individually for their perfect friendship and support over the years of my Ph.D. program.

For this dissertation, I would like to thank the other committee members: Faquir Jain and John Ayers, for their time, interest, and helpful comments.

I also would like to thank my friends from the social environment; Aram Gokce, Murat Osmanoglu, Ozgur Oksuz, Faruk Kirac, and Huseyin Yer. A special thanks to Sadullah Yildirim and Emma Linstone for their support, fruitful discussions, and a very warm friendship environment.

I would like to thank Sefa Teber, Selami Karakas, and Zafer Kaya for their trust and for being guarantors for my graduate fellowship from The Republic of Turkey.

Forever and ever, I would like to acknowledge the graduate fellowship from the Republic of Turkey Ministry of National Education.

Contents and Subject Index

List of Figures and Tables

Tables

Symbols and Acronyms

RCS	Radar-Cross Section
RAM	Radar Absorbing Material
MWCNT	Multi-walled Carbon Nanotubes
PAN	Polyacrylonitrile
MZF NPs	Manganese/Zinc Spinel Ferrite Nanoparticles
EMC	Electromagnetic Compatibility
EMI	Electromagnetic Interference
XRD	X-Ray Diffraction and Scattering
SEM	Scanning Electron Microscope
FT-IR	Fourier Transform Infrared
VSM	Vibrating Sample Magnetometry
EDX	The Energy Dispersive X-Ray
VNA	Vector Network Analyzer
X Band	8-12 GHz
Ku Band	12-18 GHz
K Band	18-26.5 GHz
NRW	Nicolson-Ross-Weir Algorithm
E	The Electric Field Strength Vector
H	The Magnetic Field Strength Vector
B	The Magnetic Flux Density Vector
D	The Electric Displacement Vector
J	The Current Density Vector
ε	Permittivity of a Material

μ	Permeability of a Material
$\varepsilon_o = 8.854 \times 10^{-12}$	Permittivity of free space (F/m)
$\mu_o = 0.4\pi \times 10^{-6}$	Permeability of free space (H/m)
$\varepsilon_r = \varepsilon / \varepsilon_o$	Relative Permittivity
$\mu_r = \mu / \mu_o$	Relative Permeability
$\tan \delta_e$	Dielectric Loss Tangent
$\tan \delta_m$	Magnetic Loss Tangent
Z_0	The impedance of free space
dB	Decibel
S_{11} and S_{21}	Scattering Parameters of 2-Port Network
RL	Return Loss
Ms	Saturation Magnetization
Hc	Coercivity
Mr	Remnant Magnetization
(hkl)	Miller Indices
a_{exp}	The Lattice Constant

This page intentionally left blank

Chapter 1
Introduction

1. Introduction

There is a growing demand for protecting military assets using stealth technology. The primary objective of "stealth" and camouflage designs is to reduce the radar cross-section (RCS) of potential targets, i.e., to make aircrafts or hardware systems less detectable to hostile radar observation systems. Two different approaches exist to create "invisibility": (i) Reduction of radar cross section via shaping, which is a measure of a target`s ability to minimize backscattered radar signals in the direction of the radar receiver, and (ii) Radar Absorbing materials (RAMs), which cover the surface of the vehicles or hardware, that absorb the incoming radar signals. In morphing applications where the target shape changes dynamically, the first approach will have obvious limitations. Therefore, the design of adaptive/smart structures incorporating RAMs, constrained by factors such as weight [1, 2], becomes more important.

Microwave absorption can be achieved using nano-structured dielectric, magnetic, or composite materials. Nonmetallic materials have been used in aircraft construction, most commonly for wings, tails and control surfaces. Examples [3] include boron/epoxy horizontal tail skins (used in the production of F14 aircrafts), boron/epoxy horizontal and vertical tail skins (F15 skins), graphite-epoxy horizontal and vertical skins and control surfaces (F16 aircrafts), graphite-epoxy wing, forward fuselage and control surfaces (Av-8B), and graphite-epoxy control surfaces (Boeing 757). These materials can be integrated/covered with suitable RAMs to enhance microwave absorption or to minimize reflection.

Radar absorbing materials reduce the energy reflected back to the radar by means of absorption. The main requirements are an effective electromagnetic wave impedance

and good attenuation at the surfaces of a RAM that result in a good match for the incoming signal once it penetrates into the material. RAMs can be categorized into two types: dielectric and magnetic absorbers, which means that the absorption is primarily due to their dielectric and magnetic characteristics, respectively. The absorption by the dielectric materials depends on dielectric loss mechanisms, such as electronic/atomic polarization, orientation (dipolar) polarization, ionic conductivity, and interfacial or space charge polarization [4] . On the other hand, transition metals (Fe, Ni, Co, Mn and Zn) are magnetic materials, which depend on magnetic loss mechanisms. Magnetic loss mechanisms include *Hysteresis loop* (from irreversible magnetization, which is negligible in a weak applied field), *Domain wall resonance* (which usually occurs in the frequency range 1-100 MHz), *Natural Resonance,* and *Eddy current losses* [5]. Both dielectric and magnetic materials have relatively low absorption when they are used by themselves [6, 7]. For that reason, this thesis explorers nano-structured composite materials, which combine dielectric and magnetic absorption.

At the macroscopic level, energy absorption in materials may be described in terms of the complex permittivity ($\varepsilon_{r=} \varepsilon_r^{'}\text{-}j\varepsilon_r^{''}$) and the complex permeability ($\mu_{r=} \mu_r^{'}\text{-}j\mu_r^{''}$). The complex permittivity and permeability represent the dynamic dielectric and magnetic properties of materials. The real components (ε_r' and μ_r') of the complex permittivity and permeability denote the storage capability of electric and magnetic energy. The imaginary components (ε_r" and μ_r") of them represent the absorption of the electric and magnetic energy. Even a small difference in permeability can affect the microwave absorption properties of the materials significiantly [8]. Another set of

parameters used in the literature to present the losses in a material is the dielectric ($\tan\delta_\varepsilon$) and magnetic ($\tan\delta_\mu$) loss tangents, which are defined as $\tan\delta_\varepsilon=\varepsilon''/\varepsilon'$ and $\tan\delta_\mu=\mu''/\mu'$.

Nano-structured composite materials consist of a combination of materials that are mixed together to achieve specific structural and microwave absorption properties. However, designing nano-structured absorber materials is challenging. It requires selecting suitable filler materials and a host matrix, which is a continuous solid phase in which guest particles (atoms, molecules, ions, etc.) are embedded. The selection of the appropriate fabrication methods, and measurement techniques are the other requirements.

Finally, the electromagnetic characteristics and microwave absorption properties of specimens are investigated in the radar frequency bands by using a network analyzer in conjunction with a non-resonant method, including waveguide and coaxial line techniques.

1.1 Objectives

The first objective of this thesis is the development of flexible, lightweight, thin, and reconfigurable RAM for military applications such as camouflaging ground-based hardware against hostile airborne radar observation. Towards this goal, fabric-based RAMs, including nano-structured magnetic, transition metals such as Nickel (Ni) and Cobalt (Co) or their alloys [9] are investigated.

The second objective is to enhance the microwave absorption properties by blending nano-structured magnetic materials with appropriate dielectric materials.

The third objective is to determine the microwave absorption properties of RAMs consisting of a combination of dielectric and magnetic materials using two non-resonant methods: waveguide and coaxial line techniques.

1.2 Organization of Thesis

Chapter I includes the theoretical background for the electromagnetic behavior of materials.

Chapter II describes fabric-based RAMs, including Polyacrylonitrile (PAN) fabrics coated with Nickel and Cobalt magnetic materials. These nanoparticles (NPs) are embedded into PAN fabrics serving as a host matrix. There is limited information about the desirable relative amounts of Ni and Co materials, an optimization criterion, or a characterization technique in the literature. In this experimental investigation, different relative concentrations of Ni and Co as well as the coating time are used with a view to optimizing the microwave absorption characteristics of the resulting knitted PAN fabrics-based composite material in the radar-frequency bands (X, K_u, and K).

Based on the experimental studies in the literature, both dielectric and magnetic materials have relatively low microwave absorption properties when they are used by themselves. It is possible to enhance absorption characteristics when dielectric materials (multi-walled carbon nanotubes) are coated or blended with magnetic nanomaterials such as transition metals or their ferrites. Chapter III describes the enhancement of the microwave absorption properties of multi-walled carbon nanotubes (MWCNTs) when blended with synthesized manganese/zinc spinel nanoparticles (MZF NPs).

Chapter IV describes the measurement of microwave absorption properties of the samples of RAMs investigated in chapter III using a coaxial line technique. The RAM

samples are molded as toroid-shaped pellets to fit within a coaxial line and their properties measured in the frequency range of 2-18 GHz.

1.3 Electromagnetic Behavior of Materials

The study of the electromagnetic properties of materials is important for various fields of science and technology. Prior work on the electromagnetic properties of materials at microwave frequencies is briefly summarized below.

First, in the 1990s, researchers (Solymar and Walsh 1998 [10]; Kittel 1997 [11]; Von Hippel 1995[12, 13]; Jiles 1994 [14]; Robert 1988 [15]) were interested especially in magnetic materials (Jiles 1998 [16]), superconductors (Tinkham 1996 [17]), and ferroelectrics (Lines and Glass 1977 [18]). Even though magnetic materials are widely used in various fields, theoretical studies about magnetic materials lag behind their practical applications. This prevented researchers from developing the full potential of magnetic materials, especially for use at microwave frequencies [4].

Second, as the clock speeds of digital electronic devices approach microwave frequencies, it becomes necessary to study the microwave electronic properties of materials used in electronic. The development of electronic circuits at microwave frequencies requires a knowledge of accurate electromagnetic constitutive parameters of materials, such as permittivity and permeability. In addition, electromagnetic compatibility (EMC) and electromagnetic interference (EMI) have to be taken into account in the design of circuits [19].

Finally, microwave systems are playing very important roles in military and commercial applications. They require precise knowledge of the electromagnetic

properties of materials at microwave frequencies [20]. As an example, there is a growing demand for protecting military hardware and personnel using stealth technology. Microwave absorbing materials are widely used in various defense and aerospace applications, such as designing “stealth” aircraft, camouflaging ground-based military assets against air-based radar surveillance, and constructing anechoic chambers (where the radar signatures of aircraft and other targets are experimentally measured).

Next is a general introduction to the electromagnetic behavior of materials at microscopic and macroscopic scales in the context of the parameters describing their electromagnetic properties.

1.3.1 Microscopic Scale in Electromagnetics

Materials are studied at both the microscopic and the macroscopic scale in physics and material science. The energy bands for electrons and magnetic moments of the atoms and molecules in materials are investigated at the atomic scale. On the other hand, the response of bulk material to external electromagnetic fields is investigated at the macroscopic level. The electrical properties of a material are principally determined by the electron energy bands of the material at the microscopic scale. According to the energy gap between the valence band and the conduction band, materials can be classified as insulators, semiconductors, and conductors. Because of its electron spin and electron orbits around the nucleus, an atom also has a magnetic moment. According to the responses of these magnetic moments to an applied magnetic field, materials can be generally classified as diamagnetic, paramagnetic, and ordered magnetic materials [4].

1.3.2 Macroscopic Scale in Electromagnetics

The interactions between a bulk material and electromagnetic fields can be described by Maxwell`s equations [21]:

$$\nabla . \mathbf{D} = \rho \tag{1.1}$$

$$\nabla . \mathbf{B} = 0 \tag{1.2}$$

$$\nabla \times \mathbf{H} = \frac{\partial \boldsymbol{D}}{\partial t} + \boldsymbol{J} \tag{1.3}$$

$$\nabla \times \mathbf{E} = -\frac{\partial \boldsymbol{B}}{\partial t} \tag{1.4}$$

with the following constitutive relations:

$$\mathbf{D} = \varepsilon \mathbf{E} = (\varepsilon' - j\varepsilon'')\mathbf{E} \tag{1.5}$$

$$\mathbf{B} = \mu \mathbf{H} = (\mu' - j\mu'')\mathbf{H} \tag{1.6}$$

$$\mathbf{J} = \sigma \mathbf{E} \tag{1.7}$$

where **H** is the magnetic field strength vector, **E** is the electric field strength vector, **B** is the magnetic flux density vector, **D** is the electric displacement vector, **J** is the current density vector, ρ is the charge density, ε is the permittivity of the material, μ is the permeability of the material, and σ is the conductivity of the material. Equations (1.1) through (1.7) point that the responses of a material to electromagnetic fields are determined essentially by five constitutive parameters, namely the real parts of permittivity and permeability (ε', μ'), the imaginary parts of permittivity and permeability (ε", μ"), and conductivity (σ). These parameters also determine the spatial extent to which the electromagnetic field can penetrate into the material at a given frequency.

The question is how these parameters are interrelated. The answer requires a review of basic electromagnetics. It is assumed that one has a piece of arbitrary material. The material is made of atoms, ions, electrons, and molecules. The electrons will naturally want

to move, once an external electric is applied across a material. The conduction electric current density varies directly with the strength of the electric field. Within the given information, the parameters of permittivity and/or permeability can be described two general categories of materials; low-conductivity and high conductivity materials.

1.3.2.1 The Parameters for Low-Conductivity Materials

Electromagnetic waves can propagate readily into low-conductivity materials. Therefore, both the surface of the material and its interior part react to the electromagnetic waves. The parameters describing the electromagnetic properties of materials in this section can be categorized into constitutive and propagation parameters.

Constitutive Parameters

The constitutive parameters in Maxwell Equations from (1.5) to (1.7) are used to describe the electromagnetic properties of low-conductivity materials. When the value of the conductivity (σ) is small. The focus shifts to the imaginary parts of permittivity and permeability parameters.

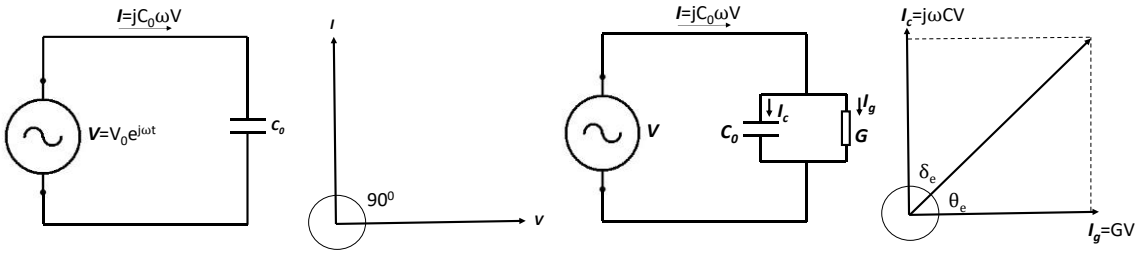

Figure 1.1 The current in a circuit with a capacitor (a) circuit layout (b) complex plane showing current and voltage: The relationship between charging current and loss current (c) the equivalent circuit (d) complex plane showing charging current and loss current.

Now, let us consider the dielectric response of low-conductivity materials. The vacuum capacitor with capacitance C_0 is connected to an AC voltage source. The circuit

(Fig. 1.1a) is shown with the current (I), which leads the voltage (V) by a phase angle of 90^0 (Fig. 1.1b). The charge storage in the capacitor is $Q=C_0V$, and the current flow (I) in the circuit is

$$I = \frac{dQ}{dt} = \frac{d}{dt}\left(C_0 V_0 e^{jwt}\right) = jC_0\omega V \tag{1.8}$$

Then, we insert a dielectric material into the capacitor to understand the relationship between permittivity and conductivity. Fig. 1.1c and 1.1d represent the equivalent circuit and the complex plane of the charging current and the loss current, respectively. The total current of the circuit has two parts, the charging current (I_c) and the loss current (I_g):

$$I = \left(I_c + I_g\right) = jC\omega V + GV = (jC\omega + G)V \tag{1.9}$$

where C is the capacitance of the capacitor loaded with the dielectric material and G is the conductance of the dielectric material. The loss current is in phase with the source voltage (V). The charging current, also, leads the loss current by a phase of 90^0 (Fig. 1d), and the total current leads the source voltage with an angle θ less than 90^0. After a dielectric material is inserted into the capacitor, the capacitance C of the capacitor becomes

$$C = \frac{\varepsilon C_0}{\varepsilon_0} = (\varepsilon' - j\varepsilon'')\frac{C_0}{\varepsilon_0} \tag{1.10}$$

The charging current is

$$I = j\omega(\varepsilon' - j\varepsilon'')\frac{C_0}{\varepsilon_0}V = (j\omega\varepsilon' + \omega\varepsilon'')\frac{C_0}{\varepsilon_0}V \tag{1.11}$$

Therefore, the current density (**J**), as shown in Fig. 2, transverse to the capacitor under the applied field strength E becomes

$$\mathbf{J} = (j\omega\varepsilon' + \omega\varepsilon'')\mathrm{E} = \varepsilon\frac{dE}{dt} \tag{1.12}$$

The parameter of ωε" is equivalent to the electric conductivity (σ). It may represent an actual conductivity produced by traveling charge carriers or it refer to an energy loss associated with the dispersion of ε'.

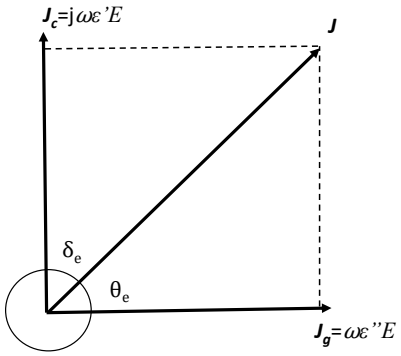

Figure 1.2 Complex plane showing the charging current density and the loss current density.

Fig. 1.2 represents that complex plane of the charging current density and the loss current density. According to Fig. 1.2, we can define the energy dissipation parameters of a dielectric material: the dielectric loss tangent and the dielectric power factor, which are given by, respectively

$$\tan\delta_e = \varepsilon''/\varepsilon' \tag{1.13}$$

$$\cos\theta_e = \varepsilon''/\sqrt{(\varepsilon')^2 + (\varepsilon'')^2} \tag{1.14}$$

It can be noted that cos (θ_e) ≈ tan (δ_e) for a small loss angle δ_e.

For microwave applications, the relative permittivity is often used as a dimensionless quantity, which is defined by

$$\varepsilon = \frac{\varepsilon}{\varepsilon_0} = \frac{(\varepsilon' - j\varepsilon'')}{\varepsilon_0} = \varepsilon_r' - j\varepsilon_r'' = \varepsilon_r'(1 - tan\delta_e) \tag{1.15}$$

where ε is the complex permittivity, ε_r is the relative permittivity, ε_0 is permittivity of free space (8.854x1e-12 [F/m]), and δ_e is the dielectric loss angle.

Now, let us consider the magnetic response of a low-conductivity material. According to Faraday`s inductance law

$$V = L\frac{dI}{dt} \tag{1.16}$$

The magnetization current I_m:

$$I_m = -j\frac{V}{\omega L_0} \tag{1.17}$$

where V is the magnetization voltage, L_0 is the inductance of an empty inductor, and ω is the angular frequency. Under lossless conditions air inductor with a magnetic material with a relative permeability ($\mu_r^{'}$) leads to

$$I_m = -j\frac{V}{\omega L_0 \mu_r'} \tag{1.18}$$

The relationship between the magnetization current and the voltage, as well as the relationship between the magnetization current and the loss current (I_g) are shown in Fig. 1.3.

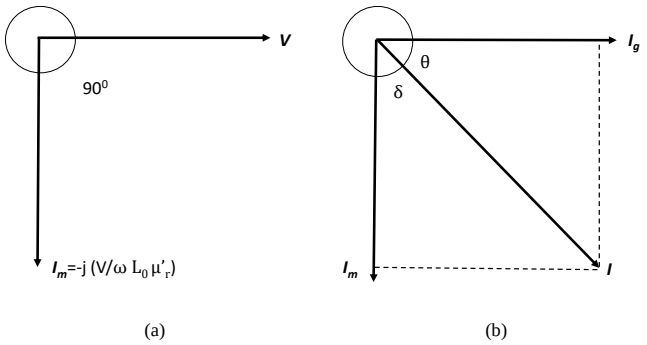

Figure 1.3 The magnetization current in a complex plane (a) The relationship between the magnetization current and the voltage (b) the relationship between the magnetization current and the loss current.

The magnetic loss current is caused by energy dissipation during the magnetization cycle. It is also in phase with magnetization voltage (V).

Now, let us consider the lossy situation in terms of the complex permeability. For a dielectric case, we can obtain the total magnetization current by introducing a complex permeability ($\mu = \mu' - j\mu''$) and a complex relative permeability ($\mu_r = \mu_r' - j\mu_r''$):

$$\mu = \frac{\mu}{\mu_0} = \frac{(\mu' - j\mu'')}{\mu_0} = \mu_r' - j\mu_r'' = \mu_r'(1 - \tan(\delta_m)) \tag{1.19}$$

$$I = I_m + I_1 = -\mathrm{j}\frac{V}{\omega L_0 \mu_r} = -\frac{JV(\,\mu r' - \mathrm{j}\mu r'')}{\omega(L_0/\mu_0)(\mu'^2 + \mu''^2)} \tag{1.20}$$

We can define the magnetic loss tangent and the magnetic power factor:

$$\tan\delta_m = \mu''/\mu' \tag{1.21}$$

$$\cos\theta_m = \mu''/\sqrt{(\mu')^2 + (\mu'')^2} \tag{1.22}$$

where μ is complex permeability, μ_r is the relative complex permeability, μ_0 is permeability of free space (4πx1e-7 [H/m]), and δ_m is the magnetic loss angle.

In conclusion, the macroscopic electric and magnetic behavior of low-conductivity materials is essentially obtained by permittivity and permeability. Energy absorption in materials is due to their dielectric and magnetic properties, which depend on the imaginary parts of the complex permittivity ($\varepsilon_r = \varepsilon_r' - j\varepsilon_r''$) and complex permeability ($\mu_r = \mu_r' - j\mu_r''$). The complex dielectric permittivity and magnetic permeability represent the dynamic dielectric and magnetic properties of materials. The real components (ε_r' and μ_r') of the complex dielectric permittivity and magnetic permeability denote the storage capability of electric

and magnetic energy. The imaginary components (ε_r" and μ_r") of them represent the loss of the electric and magnetic energy.

Propagation Parameters

There are two parameters to describe the propagation of electromagnetic waves in a medium, which are the characteristic wave impedance (η) and the complex propagation constant (γ). When a plane electromagnetic wave propagates with a velocity (υ) in the positive z-direction, the characteristic impedance is defined as the ratio of the total electric field to the total magnetic field in a z-plane. The characteristic wave impedance from the permittivity and the permeability of a medium:

$$\eta = \sqrt{\mu/\varepsilon} \tag{1.23}$$

The characteristic wave impedance of free–space is $\eta_0 = (\mu_0/\varepsilon_0)^{1/2} = 376.7$ ohm. The complex propagation coefficient:

$$\gamma = \alpha + j\beta = j\omega\sqrt{\mu\varepsilon} = j\frac{\omega}{c}\sqrt{\mu_r\varepsilon_r} \tag{1.24}$$

where ω is the angular frequency, α is the attenuation coefficient, β ($=2\pi/\lambda$) is the phase change coefficient, and λ is the operating wavelength in a medium, $c=3\text{x}10^8$ m/s is the wave velocity on free space.

1.3.2.2 The Parameters for High-Conductivity Materials

The complex propagation constant should be modified for a high conductivity material (a metal) as

$$\gamma = \alpha + j\beta = j\omega\sqrt{\mu\varepsilon}\sqrt{1 - j\frac{\sigma}{\omega\varepsilon}} \tag{1.25}$$

For a high conductivity material, we assume that the conducting current is much larger than the displacement current ($\sigma \gg \omega\varepsilon$). Therefore, the displacement current term in Eq. (1.25) can be ignored. Now, the complex propagation constant can be rewritten:

$$\gamma = \alpha + j\beta = j\omega\sqrt{\mu\varepsilon}\sqrt{j\frac{\sigma}{\omega\varepsilon}} = (1 + j)\sqrt{\frac{\omega\mu\sigma}{2}} \tag{1.26}$$

The skin depth is a measure of the depth in which electromagnetic waves can penetrate into the medium. For high-conductivity materials, the skin depth can be defined as

$$\delta_s = \frac{1}{\alpha} = \sqrt{\frac{2}{\omega\mu\sigma}} \tag{1.27}$$

The term meaning implies that the fields decay by an amount e^{-1} in a distance of a skin depth (δ_s). For good conductors, it is very small distance (micrometers) at microwave frequencies. Because of that, the behavior of a high-conductivity material at microwave frequencies is determined by its surface impedance Z_s:

$$Z_s = R_s + jX_s = \frac{E_t}{H_t} = (1 + j)\sqrt{\frac{\omega\mu}{2\sigma}} \tag{1.28}$$

where H_t is the tangential magnetic field, E_t is the tangential electric field, R_s is the surface resistance, and X_s is the surface reactance. σ is a real number for good conductors.

1.3.3 Classification of Materials

In this section, we explain further the electromagnetic behavior of typical materials, including dielectric, magnetic, and composite materials. The knowledge of the underlying

mechanisms can help understand the measurement results and is important for the design and application of these materials.

1.3.3.1 Dielectric Materials

A dielectric material is an insulator, which can be polarized by an applied electric field. When an external electric field is applied to a dielectric material, the electric charges do not flow through the material. However, certain changes in the charge configuration can happen at the atomic scale. The parameter of permittivity is the key to the behavior of dielectric materials. Fig. 1.4 represents a typical behavior of permittivity as a function of frequency.

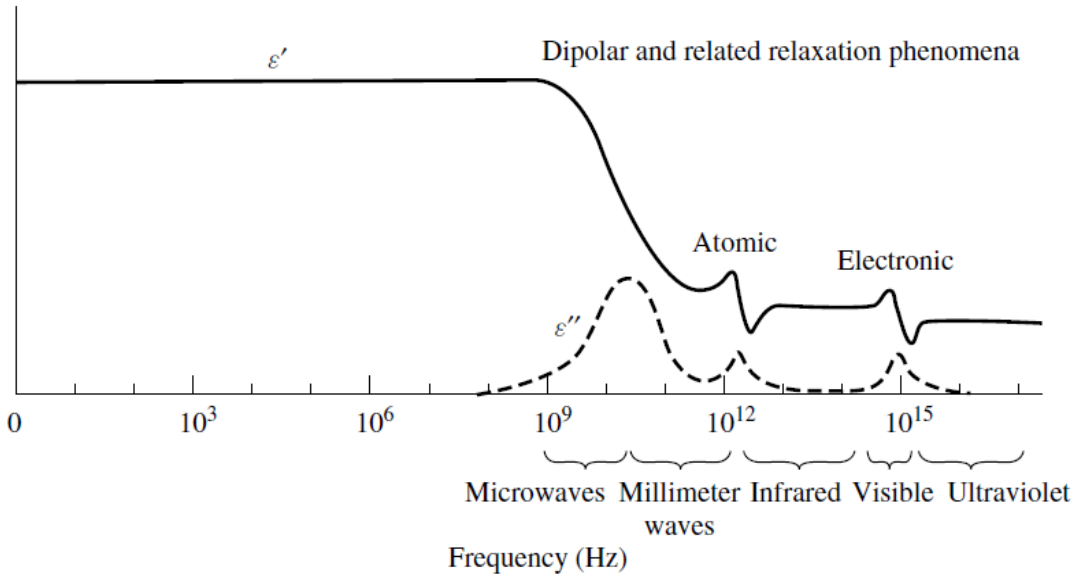

Figure 1.4 Typical behavior of the permittivity for a hypothetical dielectric as a function of frequency [20].

A material may have a variety of dielectric mechanisms or polarization effects, which contribute to its overall permittivity [22]. A dielectric material has an arrangement of electric charge carriers, which can be displaced by an external electric field. The material

becomes polarized to compensate for the applied electric field such that the positive and negative charges move in opposite directions. Different dielectric loss mechanisms can contribute to dielectric behavior. Electronic and atomic polarizations, small orientation (dipolar) polarizations, and ionic conductivity are the main mechanisms.

Electronic and atomic polarizations

Electronic polarization occurs in neutral atoms, when an external electric field displaces the nucleus with respect to the surrounding electrons. Atomic polarization occurs when adjacent positive and negative ions "stretch" under an applied electric field. Both polarizations are similar nature. Fig. 1.5 [23] represents the behavior of permittivity in the surrounding area of the resonant frequency (ω_0).

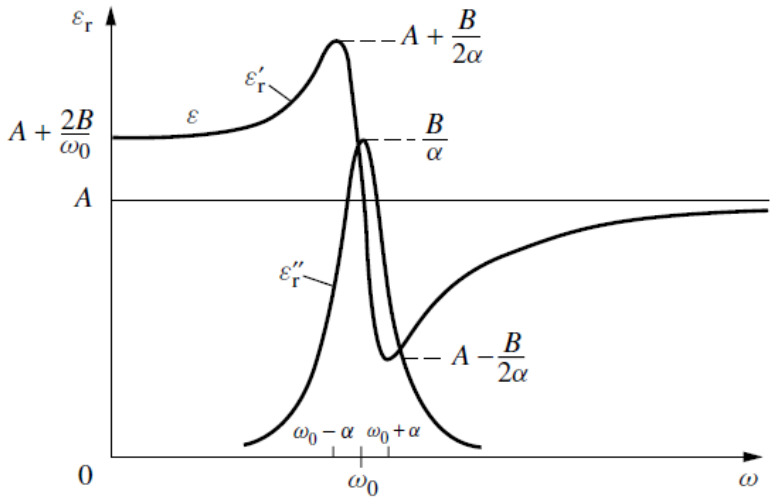

Figure 1.5 The behavior of permittivity due to electronic or atomic polarization [23]**.**

A is the contribution of higher resonance to ε_r' in the present frequency range. 2B/ ω_0 is the contribution of the present resonance to lower frequencies. These are the dominant polarization mechanisms to determine the permittivity for many dry solids at microwave

frequencies, even if the actual resonance occurs at a much higher frequency. If only these two polarizations are exist, the materials are almost lossless at microwave frequencies.

Orientation (dipolar) polarization

A molecule is formed when atoms combine to share one or more of their electrons. This rearrangement of electrons may cause an imbalance in charge distribution creating a permanent dipole moment. These moments are oriented in a random manner in the absence of an electric field so that no polarization exists. The electric field E will exercise a torque T on each electric dipole, and the dipoles will rotate to align with the electric field causing orientation polarization to occur (Fig. 1.6). If the field changes the direction, the torque will also change.

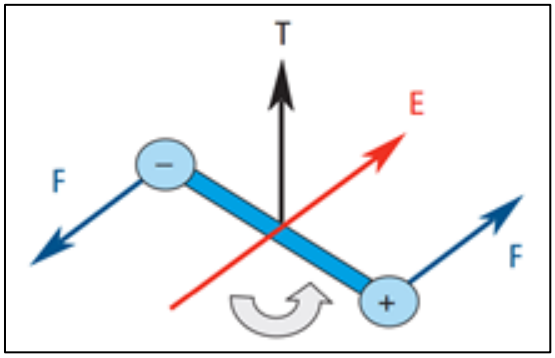

Figure 1.6 Dipole rotation, when an external field applied [22].

The friction accompanying the orientation of the dipole will contribute to the dielectric losses. The dipole rotation causes a variation in both ε_r' and ε_r'' at the relaxation frequency which usually occurs in the microwave region. Water is an example of a substance that exhibits a strong orientation polarization.

Ionic Conductivity

The measured loss of material can actually be expressed as a function of both dielectric loss (e_{rd}'') and conductivity (σ).

$$\varepsilon_r^{"} = \varepsilon_{rd}^{"} + \frac{\sigma}{\omega\varepsilon_0} \qquad (1.30)$$

At low frequencies, the overall conductivity can be made up of many different conduction mechanisms, but ionic conductivity is the most prevalent in moist materials. e_r'' is dominated by the influence of electrolytic conduction caused by free ions which exist in the presence of a solvent (usually water). Ionic conductivity only introduces losses into a material. At low frequencies the effect of ionic conductivity is inversely proportional to frequency and appears as a 1/f slope of the e_r'' curve

Interfacial or Space Charge Polarization

It occurs when the motion of these migrating charges is impeded. The charges can become trapped within the interfaces of a material. Motion may also be impeded when charges cannot be freely discharged or replaced at the electrodes. The field distortion caused by the accumulation of these charges increases the overall capacitance of a material which appears as an increase in ε_r '. Mixtures of materials with electrically conducting regions that are not in contact with each other (separated by non-conducting regions) exhibit the Maxwell-Wagner effect at low frequencies. If the charge layers are thin and much smaller than the particle dimensions, the charge responds independently of the charge on nearby particles. At low frequencies the charges have time to accumulate at the borders of the conducting regions causing εr ' to increase. At higher frequencies, the charges do not have the time to accumulate and polarization does not occur since the charge displacement is small compared with the dimensions of the conducting region. As the frequency increases, ε_r' decreases and the losses exhibit the same 1/f slope as normal ionic conductivity. Many other dielectric mechanisms can occur in the low frequency region

causing a significant variation in permittivity. For example, colloidal suspension occurs if the charge layer is of the same order of thickness or larger as the particle dimensions. The Maxwell-Wagner effect is no longer applicable since the response is now affected by the charge distribution of adjacent particles [23].

1.3.3.2 Magnetic Materials

In this part, we focus on magnetic materials with low conductivity because metallic magnetic materials are rarely utilized as magnetic materials at microwave frequencies. At microwave frequencies, the skin/ penetration depth of metals is about a few microns. The interior of a metallic magnetic material does not respond to a microwave magnetic field. Fig. 1.7 [27] indicates the typical magnetic spectrum of a magnetic material.

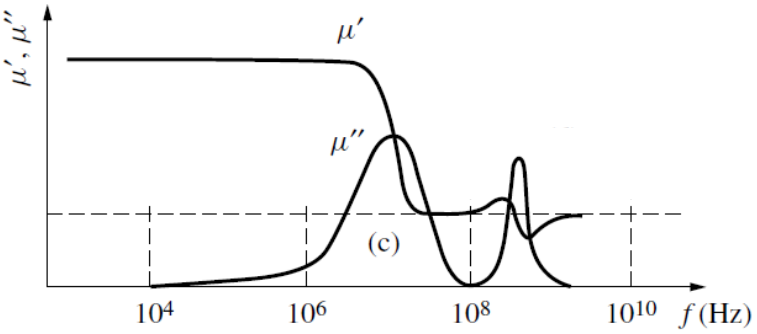

Figure 1.7 Typical behavior of the permeability for a hypothetical ferromagnetic material as a function of frequency [24].

It is seen that different physical phenomena dominate in different frequency ranges. For $f<10^4$ Hz, both the real and imaginary part of permeability do not change with frequency. In the frequency range of $10^4<f<10^6$ Hz, μ' and μ" change a little. In the frequency range of $10^6<f<10^8$ Hz, μ' decreases significantly whereas μ" increases quickly. In the frequency range of $10^8<f<10^{10}$ Hz, ferromagnetic resonance typically

arises. Above the f>10^{10} Hz, the magnetic properties of a material have not been fully investigated.

In order to explain which mechanisms affect the magnetic losses for permeability measurements, the loss mechanisms can be listed as:

- *Hysteresis Loss* from irreversible magnetization. It is negligible in a weak applied field.
- *Magnetic Resonance*
- *Eddy Current Loss* [25].

Hysteresis Loss

Fig. 1.8 shows that the hysteresis loop of a typical magnetic material. The domains are randomly orientated at the starting point 0. Therefore, the net magnetic flux density is zero.

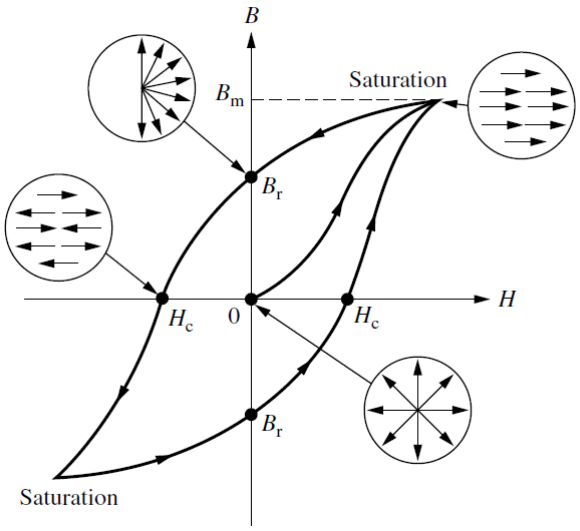

Figure 1.8 The Hysteresis Loop of a magnetic material [4].

The magnetic flux density (**B***)* increases with an increase in the magnetic field strength **H**, as the domains close to the direction of the magnetic field grow. This continues until all the domains are in the same direction as the magnetic field **H** and the material is saturated.

The flux density reaches its maximum value B_m At the saturation state. When the magnetic field strength is reduced to zero, the domains in the material turn to their easy-magnetization directions close to the direction of the magnetic field ***H***, and the material retains a remanence flux density B_r. The domains grow in the reverse direction once we reverse the direction of the magnetic field. When the numbers of the domains in the ***H*** direction and opposite the ***H*** direction are equal, the flux density becomes zero, the value of the applied magnetic field is called *coercive field H*c. Any further increase in the strength of the magnetic field in the reverse direction results in further growth of the domains in the reverse direction until saturation in the reverse direction is achieved. When this field is reduced to zero, and then reversed back to the initial direction, we can get a closed hysteresis loop of the magnetic material.

Magnetic Resonance

It is an important magnetic loss mechanism of magnetic materials. For most of the magnetic materials, the energy dissipation at microwave frequencies (GHz) is related to wall resonance and natural resonance [4].

1.3.3.3 Composite Materials

A composite material is made from two or more constituents, which have significantly different physical and chemical properties. When the constituents combine, they produce a new material with characteristics different from these of the individual components. Composite materials usually consist of a host matrix and fillers. The properties of a composite material are associated with the properties and fractions (mass and/or volume) of the constituents, so the electromagnetic properties of

composites can be tuned up by varying the properties and fractions of the constituents. The study of the electromagnetic properties of composite materials is very appealing because of the potential of developing composites with expected (or desired) electromagnetic properties. In this study, we are focused on composite materials in the classifications of dielectric and magnetic constituents, which are used as a host matrix, and fillers, respectively.

1.3.4 The Properties of Materials

The properties of materials can be classified into two categories: intrinsic and extrinsic. Intrinsic properties of a material are independent of the size of the material. If the electromagnetic properties of a material are associated with the geometry (or geometrical structures) and size are called extrinsic.

1.3.4.1 Intrinsic Properties

Most of the electromagnetic properties discussed above are intrinsic properties. They are controlled by their respective underlying mechanisms (not by geometries). The intrinsic properties are described by the constitutive parameters and the corresponding propagation parameters. As mentioned earlier in this chapter, electromagnetic waves can propagate within low-conductivity materials. The constitutive parameter for low-conductivity materials mainly consist of their permittivity, permeability and conductivity. Additionally, the propagation parameters for low-conductivity materials mainly include the wave impedance and the propagation constant.

1.3.4.2 Extrinsic Properties

The performance of electromagnetic materials/structures is also related to their geometry and property. In order to ensure that the final products (or composite materials) have the specified performance, both the intrinsic and the extrinsic properties need to monitored during the fabrication process.

A typical example of extrinsic performance is given to explain why the geometry (or size) in a RAM studied in this thesis is important for the microwave absorption properties. The dissipation of energy is made by a relatively homogeneous specimen layer backed by a ground plane (metal plate) (Fig.1.9).

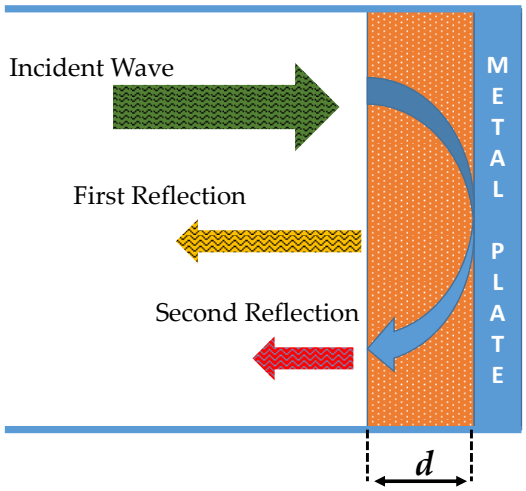

Figure 1.9 The Schematic Illustration of a Waveguide measurement Setup to explain extrinsic performance

The reflectivity of the layer depends on its thickness and the geometry for the microwave absorption measurements, which will be explained in the following chapters. In the design of the system, we have to consider the interferences between the reflections at different interfaces, which are the first reflection and the second reflection, respectively. The first reflection occurs when a part of incoming signal is reflected at the interference between the free space (or air) and the specimen layer. The other part of the incoming

signal propagates into the layer is partly attenuated by the lossy specimen and eventually is reflected at the interface between the layer and the metal plate. That is the second reflection, which after undergoing further attenuation comes out of the layer again. The first reflection can be reduced by choosing a suitable wave impedance for the specimen; the second reflection can be reduced by the loss within the specimen. Both factors contribute to the overall reflection of the RAM configuration.

This page intentionally left blank

Chapter 2

Knitted Radar Absorbing Materials (RAMs) Based on Nickel-Cobalt Magnetic Materials

2. Knitted Radar Absorbing Materials (RAMs) Based on Nickel-Cobalt Magnetic Materials

There has been a long-standing interest in the development of flexible, lightweight, thin, and reconfigurable radar absorbing materials (RAM) for military applications such as camouflaging ground-based hardware against airborne radar observation. The use of polymeric Polyacrylonitrile (PAN) fabrics as a host matrix for magnetic metal nano-particles either at the yarn-stage or after weaving the fabric for shielding and absorbing applications has been described in the literature. In this chapter, the relative concentrations of Nickel and Cobalt as well as the coating time are varied with a view to optimizing the microwave absorption characteristics of the resulting PAN-based composite material in the radar-frequency bands (X, K_u, and K).

2.1 Background & Literature Review

Bogush [26] has discussed the use of PAN fabrics as a host matrix for magnetic NPs either at the yarn stage or after weaving the fabric for the RAM applications. He has extensively discussed in his study how to deposit nano-structured materials on/over PAN fabrics and to evaluate Ni and Co for their absorption properties over wide frequency ranges (1-118GHz). However, there is no information about the relative amounts of Ni and Co materials, an optimization criterion, or a characterization technique in his study. In our experimental investigation, different relative concentrations of Nickel and Cobalt as well as the coating time are used with a view to optimizing the microwave absorption characteristics of the resulting knitted PAN fabrics-based composite material in the radar-frequency bands (X, K_u, and K).

The development of electromagnetic (EM) wave absorbing and shielding nano-structured materials has grown because of their use in the fabrication of thin, lightweight, and flexible radar absorbers for military applications such as camouflaging ground-based hardware against airborne microwave radar observation. The microwave absorption properties are determined by the complex dielectric permittivity and the complex magnetic permeability of the material and need to be tailored for maximum shielding/absorption efficiency. Microwave absorbers based on composite materials are typically composed of a polymeric dielectric matrix with conductive or magnetic filler particles of different shapes and sizes [27]. There are many processes for coating the polymer surface with nano metals such as vacuum deposition and electroless metal deposition method [28, 29]. The electroless metal deposition method has a low cost, has no limitation on the shape and size of the plated substrate, and is a low-temperature (< 100 ^{0}C) process with an industrial-scale high throughput [26]. Deposition is performed from soluble metal salts.

This chapter presents an experimental study of flexible, lightweight, thin, and reconfigurable radar absorbing materials derived from polymeric Polyacrylonitrile (PAN) fabrics coated with highly conductive metals. High-volume fibers such as PAN offer high flexibility and other desirable mechanical properties. Nickel and Cobalt were selected for deposition because of their high stability and a relatively simple deposition procedure. Polymers allow creation of numerous metallic clusters with different size and shape in the pores of the material [30].

The s-parameters of the synthesized materials were measured in the X, K_u, and K bands using a vector network analyzer (NA) in conjunction with a waveguide system incorporating samples of the coated textiles. The electromagnetic constitutive parameters

were calculated from the s-parameters using the Nicolson-Ross-Weir technique [2, 4]. In addition, the return loss (RL) of the samples is estimated from the computed complex permittivity and permeability values.

2.2 Fabrication and Measurement

2.2.1 Fabrication of PAN Samples

First, all PAN fabric samples were cut to an appropriate size to fit in the waveguides. The dimensions of the woven fabrics were 0.9x0.4, 0.6x0.3, and 0.4x0.17 inches for X, K_u, and K Bands, respectively. Second, the PAN fabric samples were cleaned and dried in an oven at 40 ^{0}C. In the next step, the samples were subjected to surface sensitization in a suitable solution. At that point, the samples were ready for electroless deposition from solutions containing metal salts (total 25 % by wt.) in order to coat the activated PAN surfaces for different durations. Finally, the samples were over-coated with a liquid polymer of a low molecular weight to protect the underlying composite from oxidation and corrosion. The coated fabric identification "codes" and the corresponding deposition times are listed in Tables 1 and 2. TA1x and TA2x codes belong to $Ni_{0.2}Co_{0.8}$ and $Ni_{0.8}Co_{0.2}$ metal concentrations (%wt), respectively. The tables contain the fabric codes, the coating times (minutes), the thickness of the fabrics (mm), the center frequency (f_r), and the bandwidth of the return loss (GHz).

The fundamental requirements of deposition bath can be listed as *metal ions/their concentration from producing soluble metal salts, reducing agent, complexing agent, bath stabilizers (control of pH and temperature), and surfactant.* In electroless deposition method, metal ions are reduced by the action of a chemical reducing agent, which is simply

an electron donor. The metal ions are electron acceptors, which receive electrons generated because of reducing agent oxidation reaction, which occurs at catalytic surface of the substrate that typically contains nucleation sites of metals. It is an autocatalytic process, which accelerates the electroless chemical reaction allowing oxidation of the reducing agent used. The process will lead to the growth of metal structures. The basic diagram of the deposition bath is shown in Fig. 2.1.

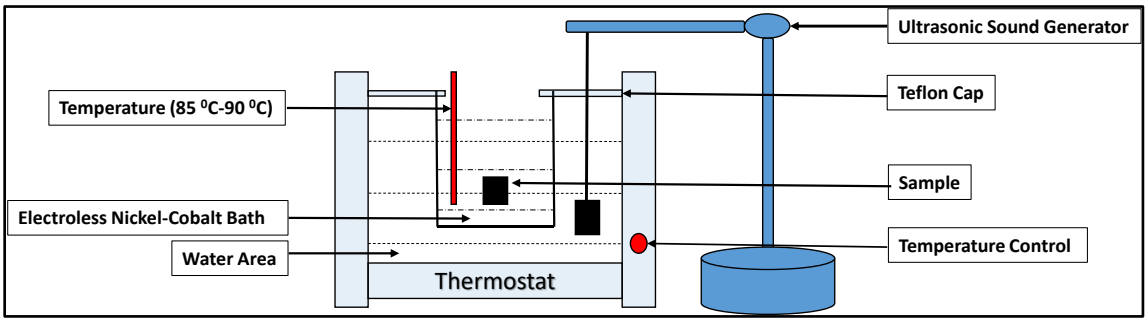

Figure 2.1 The basic diagram of the deposition bath

Deposition is performed from soluble metal salts. Reaction rate is controlled by bath compositions and it runs fast enough to provide high throughput for industrial systems.

Magnetic and highly conductive metals such as nickel and cobalt were selected for deposition due to their high stability and relatively simple deposition procedure. Metallic clusters are formed from ions attached to fiber by chemisorption with reducing in aqueous solution.

Fabrication Stages

Using polymers allows the creation of numerous metallic clusters with different size and shape in nano-size pores of material. That creates a complex three-dimensional conductive and magnetic structure. In addition, polymers prevent any oxidation and corrosion on the textiles. Special type of polymer was used to enhance chemisorption

properties of PAN. Such polymer have been used in applications such as electromagnetic shielding, anticorrosive coatings, manufacturing electrically conducting yarns [31] because of their lightweight, conductivity, flexibility and low cost. Before starting the fabrication process, the PAN textiles were modified after applying the special type of polymer, like transformation, as described in [32].

a. Pre-Treatment

To clean industrial contaminants in/on PAN, PAN textile was washed with a non-ionic detergent (pH=7) for 20 min. The amount of the detergent was 2% of deionized water. Then, PAN is held in an ultrasonic Ethanol bath for 10 min. The ultrasonic bath of Ethanol was intended to clean trapped contaminants between the knots or the corners of the knots using the high frequency sound waves generated by the Sonorex Super 10P model ultrasonic device. Ethanol in the crucible is squeezed and oscillated influenced by the ultrasound waves, resulting in thousands of little bubbles during this process. The resulting bubbles collapse at the bottom of the crucible. PAN textile is ready for sensitization stage after the PAN textile washes with deionized water for 5 min and dried in an oven at 40 °C.

b. Sensitization

Some chemical bonds on the surface of PAN are broken and ready for a new chemical bonding during this process. PAN textile was subjected to surface sensitization in a suitable solution, which was a mixture of the surface sensitizer of Tin (II) Chloride ($SnCl_2$) with 5g/l and hydrochloric acid (HCl) (concentration 37% is equal to 37 g/mol or 12mol/L). Then the solutions was slowly agitated for 10 min at room temperature. The sensitized textile was rinsed with deionized water for 5 min.

c. Activation

Metal nucleation will happen on this stage. The PAN textile was immersed in the activator bath, which was composed of certain amount of Palladium (II) chloride ($PdCl_2$), HCl, and Boric acid (H_3BO_3) to obtain required conditions (pH=2, room temperature (25 ^{0}C) for 5 min) of surface activation. The ingredients and their respective amounts are listed below.

TABLE I
COMPOSITIONS FOR ACTIVATION STAGE

Compositions	**Amount of composition**
Palladium (II) chloride ($PdCl_2$)	0.3 g/l
Hydrochloric acid (HCl)	0.5 ml/l
Boric acid (H_3BO_3)	20 g/l

After the activation stage, the textile needs to be cleaned with deionized water for 5 min.

d. Deposition

Deposition was performed from solutions containing *metal salts, stabilizer and reducing agent*. Growth of metal structures was conducted using either autocatalytic deposition or ion-molecular layering with stirring and correction of main solution components: metal ions and reducing agent. The deposition baths for electroless Ni or Co are composed mainly *Nickel (II) Chloride 7-hydrate or Ni (II) Sulphate* (the source of Ni) *and Cobalt (II) Chloride* (the source of Co). The bath temperature is kept around 85 ^{0}C - 90 ^{0}C. The rate of pH is maintained in acid range for bath stability, but the generation of hydrogen causes the pH value to decrease. To prevent this, alkaline salts of Na are usually added. In this work, we used sodium hydroxide. Fig. 2.2 [33] shows the effect of solution pH and bath temperature on the plating rate of electroless Ni deposits.

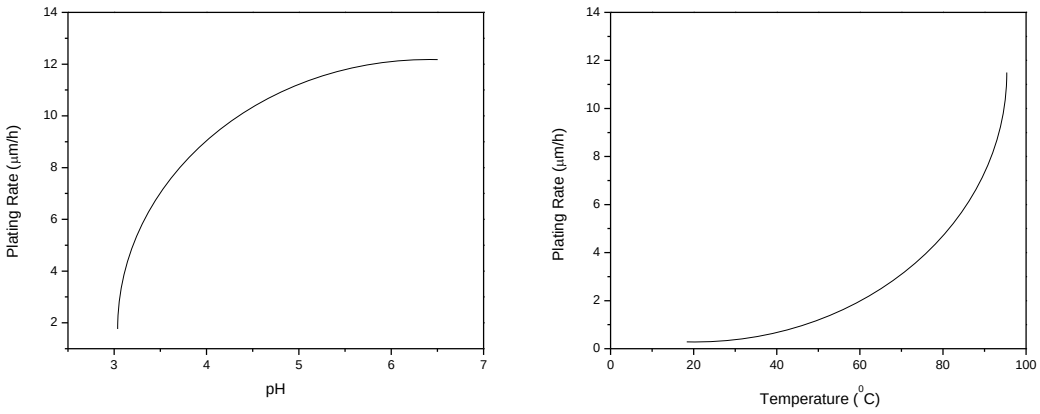

(a) (b)

Figure 2.2 The effect of solution pH and bath temperature on the plating rate of electroless nickel deposits.

Metal Salts

Nickel (II) Chloride 7-hydrate, Ni (II) Sulphate are primary source of Ni. *Cobalt (II) Chloride* is primary source of Co. For this work, two different compositions of Ni–Co alloy, namely of 20/80 and 80/20 weight ratios. Amount of deposited metal was measured via *gravimetric technique* [1].

Reducing Agent

Sodium hypophosphite employed as reducing agents in the case of formation of cluster structure from nickel, cobalt or alloys. It was used in the chemical reduction of Nickel-Cobalt from aqueous solutions.

The reduction of metal ions by hypophosphite involves two reactions (i) hypophosphite ions are catalytically oxidized, (ii) Ni-Co ions are reduced at the catalytic surface. A part of released hydrogen is absorbed onto the catalytic surface, which is called an anodic reaction. Then, The Ni-Co ions at the surface of the catalyst is reduced by the absorbed active hydrogen, which is called a cathodic reaction. Therefore, electroless

deposition mechanism is related to anodic and cathodic reaction. Some absorbed hydrogen reduces small amount of the hypophosphite to water, hydroxyl ion and phosphorus. For an average efficiency of 37%, 1 kg of sodium hypophosphite is needed to reduce 200 g of Ni or Co.

Stabilizers

- **Complexing agent:** It is added to prevent the decomposition of solutions and to control the reaction so that it occurs only on the catalytic surface. Complexing agents are organic acids or their salts, added to control the amount of free electron (Ni or Co) available for reaction. Therefore, ***Tri-sodium citrate*** is used as buffer and complexing agent or pH control agent.

- **Ammonium Chloride** is used as a flux, which is a flowing agent or purifying agent. Fluxes may have more than one function at a time. For this work, it is used to maintain low temperatures in the aqueous solution.

- **Sodium Hydroxide** is utilized for pH regulation in aqueous solution. This material is used since the solutions are cheaper and easier to handle. In small amounts, some of Sodium Hydroxide may increase the rate of deposition. We suggest that it would be better to use one or a couple drops of Sodium Hydroxide. We have to consider that temperature, pH, metal ion concentration and concentration of the reducing agent control the coating rate!

Eventually, all the metallized PAN textiles need to be rinsed with deionized water at 40 ^{0}C for 20 min after deposition treatment.

Bath compositions and operating conditions are listed below.

Bath Compositions	Descriptions	Conditions
15 g/l Sodium hypophosphite monohydrate	Reducing agent	40±1 ^{0}C, pH=9, Different coating times.
Iso-butanol	Low-molecular weight surfactant	
8 g/l tri-sodium citrate	Buffer and complexing agent	
A few drops Sodium Hydroxide	Strong base, which react with acids to form salts	
18g/l ammonium Chloride	To produce low temperature in cooling baths.	
Metals Salts		
15 g/l (for each salt) is preferred.	The source of Ni and Co	

e. Last-Treatment

High activity of metal particles and its oxidation by air oxygen in the presence of residual water from plating solution requires additional protection that was created using low molecular weight surfactants such as **iso-butanol.** Iso-butanol is a major industrial solvent and key to the production of myriad chemicals and polymer intermediates. Bio-based iso-butanol can serve as a key component in coatings, cleaning formulations, anti-wear inhibitors and polymer intermediates while improving upon corporate sustainability targets. The PAN textiles, after deposition process, were over coated with a liquid surfactant of a low molecular weight iso-butanol. Then, the cleaned PAN textiles were cured by steaming machine at 150 ^{0}C for 1 min. All textile samples were conditioned under standard atmospheric pressure at 65±2% relative humidity and room temperature for at least 24 h before evaluation or microwave measurements.

2.2.2 Experimental Methods and Measurement System

The crystal structure of the resultant composites was characterized using X-ray diffractometer (Rigaku DMax-3C diffractometer with Cu Kα radiation of wavelength λ=1.5406 Å) in the 2θ range of 35–90 degrees. Scanning electron microscopy (Philips XL30 SPEG with scanning electron microscopy) was employed to observe the amount of deposited material as nickel and cobalt filler particles. Finally, microwave absorption measurements were carried out in the X, K_u, and K bands via the Transmission Line Technique using a network analyzer (Agilent PNA E8364B) in conjunction with a waveguide system incorporating samples of the coated fabric. The technique involves placing the materials under measurement in a section of the waveguide and measuring the two-port complex scattering parameters with the NA. The set up including the sample holders with coated/uncoated samples is shown in Fig. 2.3.

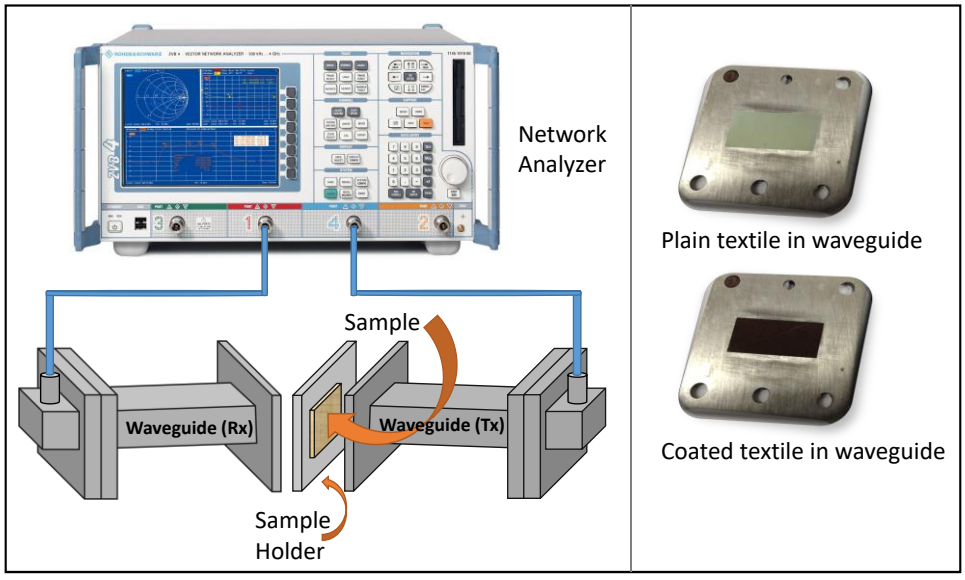

Figure 2.3 Waveguide Measurement System.

Calibration must be carried out with the sample holder holding the non-coated PAN fabric sample before making measurements on the coated fabric samples. The material must fit tightly in the sample holder in order to reduce the measurement uncertainty caused by air gaps. After calibration was done, all samples were put into the holder and s-parameters were measured by using the graphical user interface on the network analyzer. Electromagnetic constitutive parameters for the coated fabrics (ε', ε", μ', μ") were calculated from the measured s-parameters (S_{11} and S_{21}) using the Nicolson-Ross-Weir technique. Finally, the free-space reflection loss (RL) of the conductor-backed samples was calculated from the following equation [34];

$$\mathrm{RL(dB)} = -20\log|(Zin - Zo)/(Zin + Zo)| \qquad (2.1)$$

Here, the effective input impedance of the radar absorbing material sample is $Z_{in}=Z_0\sqrt{\mu_r/\varepsilon_r}\tanh[(-j\,2\pi/c)fd\sqrt{\mu_r\varepsilon_r}]$, where μ_r and ε_r are the measured relative complex permeability and permittivity, respectively, c is the speed of light, f is the frequency of operation, and d is the thickness of the sample. The results are discussed in the following section.

2.3 Results and Discussion

2.3.1 Morphology and Crystal Structure Characterization

The coated fabrics were analyzed by using X-ray powder diffraction (XRD) and Scanning Electron Microscopy (SEM). The XRD patterns of PAN fabrics shown in Fig. 2.4a and b confirm that the deposited particles are composed of Ni-Co alloys. Also, no oxide peaks are detectable in the XRD patterns, indicating that the fabrics coated with Ni-

Co nanoparticles are almost free from oxidation, thanks to the liquid polymer shell with a low molecular weight (from the last step of the treatment process).

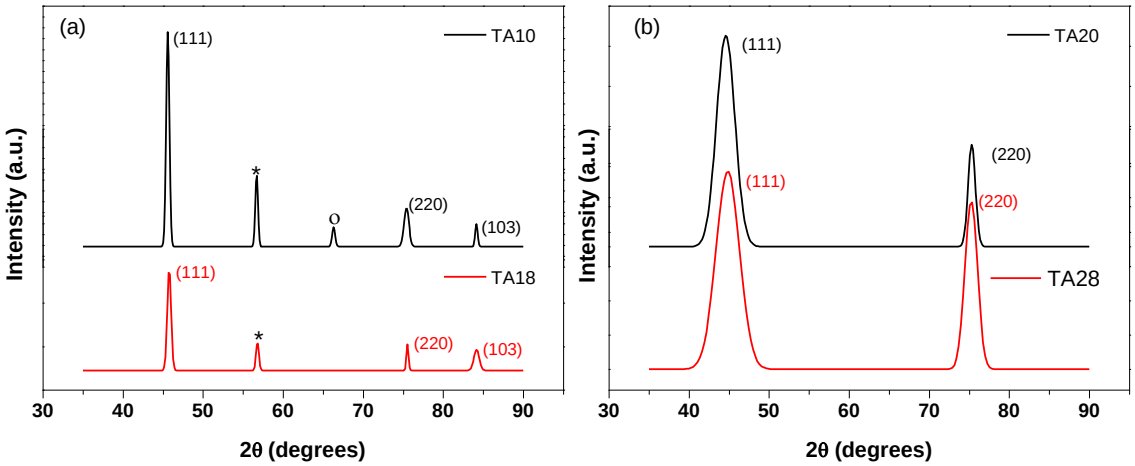

Figure 2.4 XRD patterns of coated fabrics for the shortest and the longest coating times with $Ni_{0.2}Co_{0.8}$ bath, (b) with $Ni_{0.8}Co_{0.2}$ bath.

The observed diffraction peaks (for the fabric with the TA10 code) can be assigned to (111), (110) and (103) crystal planes of Co in the hexagonal close-packed (hcp) structure. Furthermore, they were found to correspond to the following reference XRD patterns: JCPDS 99-101-2978 and [35, 36]. The lattice constants have been calculated as a = 2.505 Å and c = 4.09 Å (c/a =1 .632, the ideal ratio is 1.633). The crystal sizes, calculated by Scherrer`s formula [37], of the fabric with the TA10 code are 15.39 nm for the orientation (111), 23.43 nm for the orientation (110), and 13.76 nm for the orientation (103). For the fabric with the TA18 code, the XRD peaks can be assigned to (111), (220), and (103) crystal planes of Co in the face-centered cubic (fcc) structure. The lattice constant has been calculated as a = 3.546 Å. The crystal size values of the fabric with TA18 code are 18.46 nm for the orientation (111), 13.82 nm for the orientation (220), and 19.92 nm for the orientation (103). The marked peaks indicate the presence of NaCl (*) and of NiS (o) because of the detergent residues resulting from the pretreatment process [26, 32, 38].

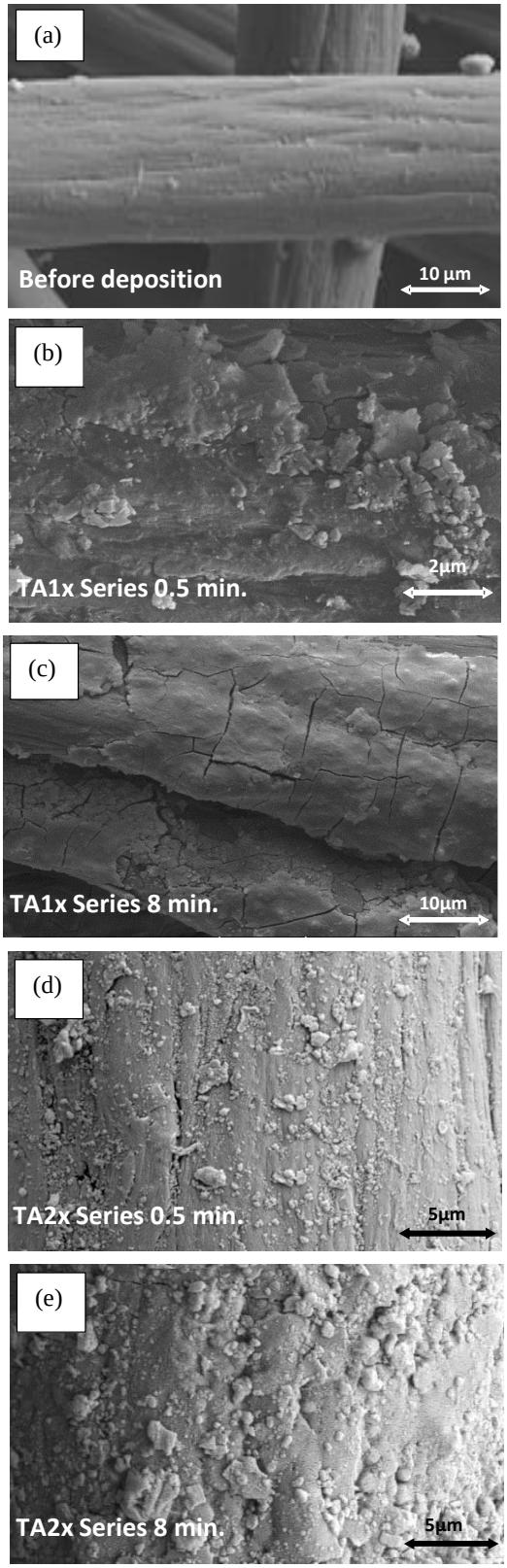

Figure 2.5 SEM Micrographs of (a) Non-coated fabric, (b) TA1x series with the shortest coating duration, (c) TA1x series with the longest coating duration, (d) TA2x series with the shortest coating duration, (e) TA2x series with the longest coating duration.

The fabric samples coated for the shortest duration contain incomplete reduced metal ion forms. The calculated lattice parameters of cobalt phase are in an agreement with the published values [39, 40]. The characteristic diffraction peaks of the samples of $Ni_{0.8}Co_{0.2}$, i.e, with higher Ni content (Fig. 2.4b), show the existence of a face centered cubic (fcc) phase, in good agreement with references JCPDS 99-101-2978 and [41]. The crystal size of the samples have been estimated to be in the range 12-26 nm. The lattice constant (a = 3.526 Å) deviates only by 0.06% from the established value of fcc nickel (3.5238 Å) [42].

SEM micrographs of PAN in Fig.2.5 show that clusters are distributed as particles of different sizes and shapes and it appears that the fabric was coated with the deposited material. The coating duration time varied from 0.5 min to 8 min for the TA1x ($Ni_{0.2}Co_{0.8}$) and the TA2x ($Ni_{0.8}Co_{0.2}$) Series. For the longest coating time, cracked layers were observed for the TA1x ($Ni_{0.2}Co_{0.8}$) Series. The roughness on the surface of the fabrics increased because of the formation of nanoparticles. This is an important parameter for the assessment of the success of the coating process.

2.3.2 Electromagnetic Constitutive Parameters

The electromagnetic constitutive parameters were calculated from the s-parameters by the transmission line method using the Nicolson-Ross-Weir technique [4, 43]. Fig. 2.6 shows the real part of the relative permittivity, permeability, as well as dielectric and magnetic loss tangents [tan $(\delta_e)$and tan(δ_m)] of two different compositions of Ni-Co alloy, namely of 20/80 and 80/20 weight ratios. Fig. 2.6a and 2.6c show that the ε' (epsilon)' of the coated fabrics gradually decreased for frequencies less than 20 GHz and tend to be

constant with nearly no variation throughout the 20-26.5 GHz range for both series of coated fabrics [44-48]. It was observed that the real parts ε' increase as the coating time increases for both the TA1x and the TA2x series.

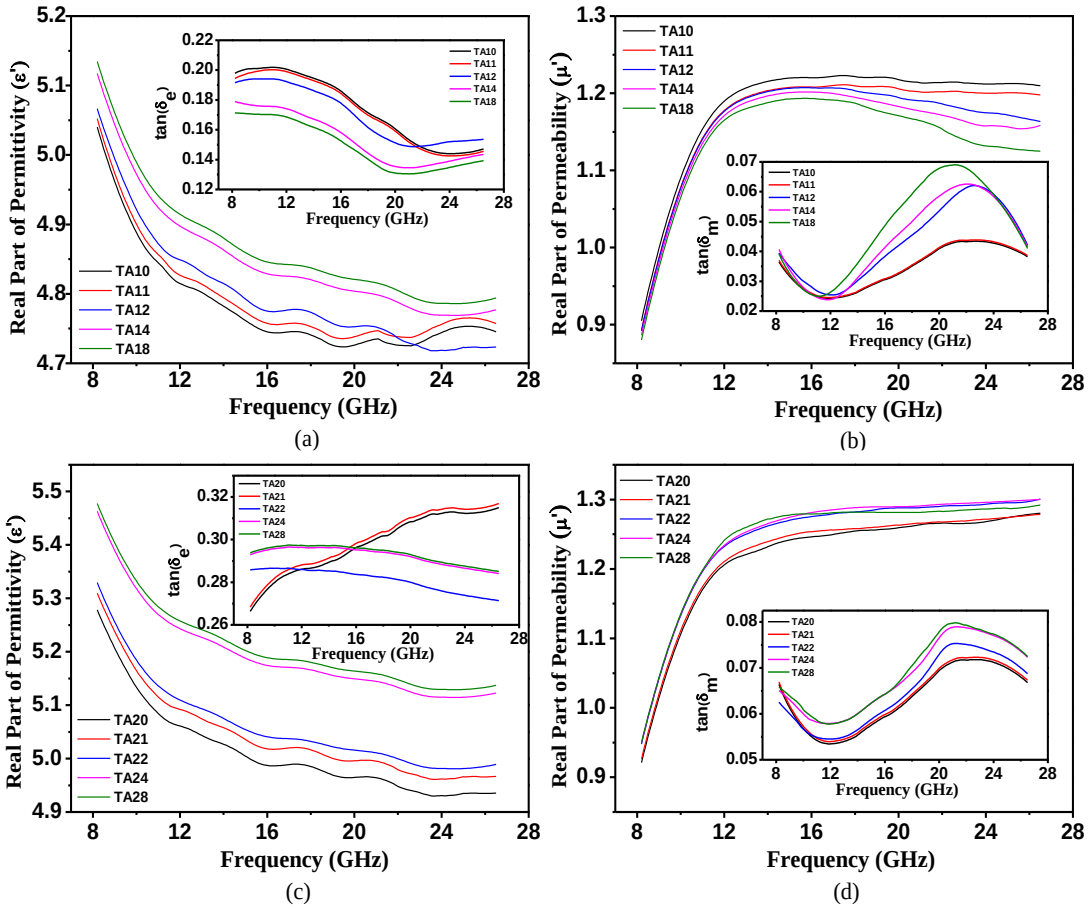

Figure 2.6 Electromagnetic constitutive parameters with (a) Real part of permittivity and dielectric loss for PAN coated with $Ni_{0.2}Co_{0.8}$, (b) Real part of permeability and magnetic loss for PAN coated with $Ni_{0.8}Co_{0.2}$, (c) Real part of permittivity and dielectric loss for PAN coated with $Ni_{0.8}Co_{0.2}$, (d) Real part of permeability and magnetic loss for PAN coated with $Ni_{0.2}Co_{0.8}$.

Fig. 2.6b and 2.6d show the real part of the permeability and the magnetic loss tangent of the coated fabrics. The real part of permeability increases sharply up to 12 GHz, then it tends to be constant around 1.2 and 1.3 for the TA1x and the TA2x series, respectively, while the frequency is increased to 26.5 GHz.

The dissipation factors are represented by dielectric loss ($\tan(\delta_e) = \varepsilon_r'' / \varepsilon_r'$) in Fig.2.4a and c. The magnetic dissipation factors, ($\tan(\delta_m) = \mu_r'' / \mu_r'$) are shown in Fig. 2.4b and d. The magnetic loss of the coated fabrics increases as the coating time increases. The TA2x series fabrics have higher dielectric losses than the TA1x series fabrics. In addition, it is apparent that, the dielectric losses are higher than the magnetic losses, which means that the absorption originates mainly from the dielectric characteristics of the coated fabrics rather than the magnetic characteristics.

2.3.3 Microwave Absorption Properties

The variation of the (computed) free-space return loss (RL) for the conductor-backed PAN fabrics coated with various nano composites Ni-Co alloys of approximately the same thickness (2 mm) are shown in Fig. 2.7.

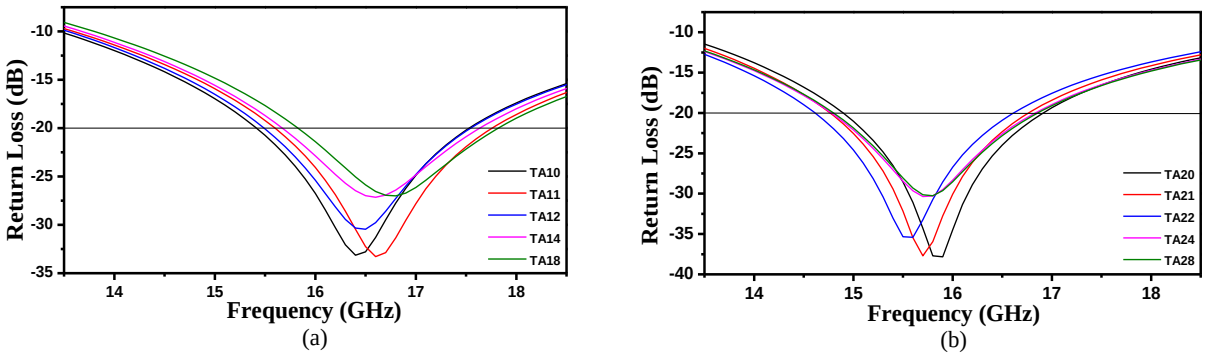

Figure 2.7 Frequency dependence of the RL of PAN fabrics containing Ni-Co alloys (a) $Ni_{0.2}Co_{0.8}$, (b) $Ni_{0.8}Co_{0.2}$

The bandwidth (found to be approximately 2 GHz in this study) is defined here as the frequency range, over which the return loss is less than -20 dB. The return loss was calculated from a transmission-line-theory based computer simulation (MATLAB) using the complex permittivity and the permeability values obtained from the measurements.

The dips in the values of RL versus frequency imply low reflectivity (and good absorption). As reported in the literature [49], the values of $\varepsilon_r^{'}$ and $\varepsilon_r^{''}$ vary with increasing coating time, resulting in a variation in the depth of the RL troughs. Furthermore, the difference between the TA1x and the TA2x series fabric samples is that RL troughs are positioned above or below the 16 GHz reference frequency for the TA1x and the TA2x series, respectively (Fig. 2.7a and 2.7b). This shows that the center frequency (f_r) for the minimum RL can be manipulated simply by changing the coating time and the Ni-Co concentrations for the coated fabrics. The measurement results are summarized in Tables II and III.

TABLE II
FABRICS CODES, CORRESPONDING DEPOSITION TIMES AND RESULTS FOR TA1X SERIES

Code	Coating Time	Thickness d (mm)	f_r (GHz)	Return Loss (dB)	Bandwidth (GHz) (under -20 dB)
TA10	0.5	2.0189	16.39	-33.18	2.10 (15.32-17.42)
TA11	1	2.0299	16.59	-33.32	2.17 (15.59-17.76)
TA12	2	2.0278	16.50	-30.48	2.04 (15.49-17.53)
TA14	4	2.0209	16.58	-27.19	1.97 (15.67-17.64)
TA18	8	2.0248	16.78	-27.05	2.00 (15.82-17.82)

TABLE III
FABRICS CODES, CORRESPONDING DEPOSITION TIMES AND RESULTS FOR TA2X SERIES

Code	Coating Time	Thickness d (mm)	f_r (GHz)	Return Loss (dB)	Bandwidth (GHz) (under -20 dB)
TA20	0.5	2.0188	15.91	-37.91	2.06 (14.89-16.95)
TA21	1	2.0298	15.69	-37.75	2.01 (14.75-16.76)
TA22	2	2.0276	15.55	-35.43	1.99 (14.61-16.62)
TA24	4	2.0206	15.70	-30.43	2.09 (14.74-16.84)
TA28	8	2.0196	15.79	-30.30	2.08 14.79-16.87)

We can compare the RAM performance that we fabricated with similar RAM performance in the literature. Our collaborators had previously investigated coated PAN fabrics with different coating times [8]. The microwave absorption curves show that microwave absorption properties depend on

the coating time. It is seen that the PAN fabrics with the shortest coating time are more effective than the PAN fabrics with the longest coating time in terms of microwave absorption.

2.4 Conclusion

In this study, PAN fabrics coated with different weight fractions of Ni-Co alloys have been investigated. XRD Patterns confirmed the crystal structures with the existence of single Ni and Co phases (fcc for the $Ni_{0.8}Co_{0.2}$ bath and hcp for the $Ni_{0.2}Co_{0.8}$ bath). As expected, it was observed that, as the coating time increased, more metal salts resolved and deposited on the surface of PAN fabrics in a solid state solution, and it was possible to transition from crystal clusters to smooth metallic coatings on PAN fabrics. However, more crystal clusters mean highly ordered metallic coatings, which are not desirable for the broadband radar absorbing characteristics. The microwave absorption depends on coating time. The TA2x series with the shortest coating time have the best RL. However, the bandwidth for the RL values does not change significantly with the coating times. The value of the dielectric tangent loss ($\tan \delta_\varepsilon$) is higher than the value of the magnetic tangent loss ($\tan \delta_\mu$), which indicates that the absorption is more due to dielectric losses rather than due to magnetic losses.

This page intentionally left blank

Chapter 3

Manganese and Zinc Spinel Ferrites Blended with Multi-Walled Carbon Nanotubes as Microwave Absorbing Materials

3. Manganese and Zinc Spinel Ferrites Blended with Multi-Walled Carbon Nanotubes as Microwave Absorbing Materials

Magnetic and dielectric materials can be blended to enhance absorption properties at microwave frequencies, although the materials may have relatively weak attenuation capabilities by themselves. The specific goal of this work is to enhance microwave absorption properties of materials with interesting dielectric behavior by blending them with magnetic materials based on transition metals. In this chapter, the synthesized $Mn_{1-x}Zn_xFe_2O_4$ (x = 0.0 and 1.0) spinel ferrite nanoparticles (MZF NPs) were blended with commercial multi-walled carbon nanotubes (MWCNTs) in various proportions with a binder matrix of paraffin. This simple and efficient process did not cause a significant variation in the energy states of MWCNTs. MZF NPs were synthesized with a citric acid assisted sol–gel method. Their electromagnetic characteristics and microwave absorption properties were investigated. These properties were derived from the microwave scattering parameters measured via the transmission line technique by using a vector network analyzer (VNA) in conjunction with an X band waveguide system. The return loss (RL) values of the samples were obtained from the electromagnetic constitutive parameters (permittivity and permeability).

3.1 Background & Literature Review

Microwave absorbers are widely used in various defense and aerospace applications, such as designing “stealth” aircraft, camouflaging ground-based military assets against air-based radar surveillance, and constructing anechoic chambers (where the radar signatures of aircraft and other targets are experimentally measured). The objective

of “stealth” and camouflage designs is to reduce the radar cross-section (RCS) of potential targets, i.e., to make aircrafts, vehicles, or hardware systems less detectable to hostile radar observation systems. Two approaches may be used to achieve a reduced RCS: shaping the target so that the signal coming from the radar is guided in the desired directions (less “backscatter”) and using radar-absorbing materials (RAMs) for attenuating the incoming signal. In morphing applications, where large shape changes may be expected, the first approach will have obvious limitations. Therefore, reducing RCS by means of adaptive/smart structures incorporating RAMs becomes even more important. In general, the design and application of RAMs has to be constrained by factors such as weight, production costs, and maintenance [1]. Morphing concepts often involve the existence of a suitable flexible skin, which has to be not only soft enough to permit shape changes but also rigid enough to withstand loads [23]. This paper presents novel soft-skin RAMs, which may have many potential applications including those in morphing scenarios.

Nonmetallic materials have been used in aircraft construction, most commonly for wings, tails and control surfaces. Examples [3] of this include boron/epoxy horizontal tail skins (used in the production of F14 aircrafts), boron/epoxy horizontal and vertical tail skins (F15 aircrafts), graphite-epoxy horizontal and vertical skins and control surfaces (F16 aircrafts), graphite-epoxy wing, forward fuselage and control surfaces (Av-8B), and graphite-epoxy control surfaces (Boeing 757). These materials can be integrated/covered with suitable RAMs to enhance microwave absorption or to minimize reflection.

RAMs can be categorized into two types: dielectric and magnetic absorbers, which means that the absorption is primarily due to their dielectric and magnetic characteristics, respectively. The absorption by multi-walled carbon nanotubes (MWCNTs) is related to

their dielectric properties (complex permittivity), which depend on dielectric mechanisms, such as electronic polarization and ion polarization. On the other hand, transition metals, such as Fe, Ni, Co, Mn, and Zn, are magnetic materials, which rely on their magnetic properties (complex permeability) to attenuate microwaves. However, both dielectric and magnetic materials have relatively low absorption when they are used by themselves. It is possible to enhance absorption characteristics when dielectric materials (MWCNTs) are coated or blended with magnetic nanomaterials, such as transition metals or their ferrites, which are known for their microwave absorption properties [6, 7].

Previous studies have used magnetic fillers, such as iron (Fe) [49], nickel (Ni) nanowires [50], hybrid materials consisting of magnetite nanocrystals [6], carbonyl iron particles [51], magnetite nanoparticle and hollow carbon fiber composites [52], carbon-encapsulated cobalt (Co) nanoparticles [53], Co [54] , Ni and Co [55], zinc oxide whiskers [56], in conjunction with CNTs [57] and ZnO [58]. We investigated manganese and zinc spinel ferrite nanoparticles (MZF NPs) as filler materials because of their high flexibility, high electrical resistivity, enhanced magnetic properties at radio frequencies, and their super-paramagnetic behavior attributable to the nano-magnetic-sized particles. Moreover, MZF NPs were blended in the MWCNTs through a simple and efficient process that did not cause a significant variation in the energy states of MWCNTs. Our choice of MZF NPs is consistent with the previous studies that used transition metals without MWCNTs, such as Ni and Co [59], Co [60], nickel ferrite composites [61], NiCoZn spinel ferrites [62], Ni and Zn spinel ferrites [63], and MnZn ferrite/rubber [64]. Gama, Rezende, and Dantas [64] reported on the dielectric, magnetic and microwave absorption properties of rubber radar absorbing materials depending on the Mn–Zn volume fractions (prepared by the usual

ceramic sintering method from a mixture of Fe_2O_3) and the thickness values of RAM in the 2–18 GHz frequency range. Our work differs from [64] in that MZF NPs (synthesized using a citric acid assisted sol–gel method) are used to implement the magnetic materials. Desirable features of spinel ferrites, such as their enhanced magnetic properties in the radio frequency region have attracted great interest in recent years [65]. Manganese ferrite ($MnFe_2O_4$) and zinc ferrite ($ZnFe_2O_4$) are common spinel ferrite materials and they have been used widely in microwave and magnetic recording applications [66]. We investigated the effect of MWCNTs on magnetic, dielectric, and microwave absorption properties of $MnFe_2O_4$ and $ZnFe_2O_4$ spinel ferrite RAMs according to their mass fractions.

To obtain the electromagnetic constitutive parameters (permittivity and permeability), we measured the scattering parameters in the X band with an Agilent PNA E8363B network analyzer (KEYSIGHT Technologies, Santa Rosa, CA, USA), in conjunction with a waveguide system combining samples of MZF NPs blended with MWCNTs. The electromagnetic constitutive parameters of the specimens were calculated from the measured scattering parameters using the Nicolson-Ross-Weir algorithm [67]. The return loss (RL) values for each sample were additionally obtained from the calculated complex permittivity and permeability values in order to assess their suitability as radar-absorbing materials.

3.2 Materials and Methods

3.2.1 Materials

The binder matrix used in this work is paraffin. Commercial MWCNTs, supplied by U.S. Research Nanomaterials, Inc., Houston, TX, USA, were used as a dielectric filler. Their main characteristics, as provided by the supplier, are listed in Table IV [68].

TABLE IV
THE MAIN CHARACTERISTICS OF THE COMMERCIAL MULTI-WALLED CARBON NANOTUBES (MWCNTS) ADOPTED AS FILLER.

MWCNT Dimensions	**Bulk Density**	**Specific Surface Area (m^2/g)**	**Purity (wt %)**	**Aspect Ratio**	**Manufacturing Method**
Inside Diameter 5–10 nm, Outside Diameter 20–30 nm (from HRTEM, Raman), length 10–30 μm (from TEM)	0.28	>110 (from BET)	>95 (carbon nanotubes from TGA and TEM) >97 (carbon content)	10^3	Chemical Vapor Deposition (CVD)

Manganese and zinc spinel ferrites (MZF NPs) have been used as filler magnetic materials after their synthesis by a citric acid assisted sol–gel method, which will be discussed in detail in the next section.

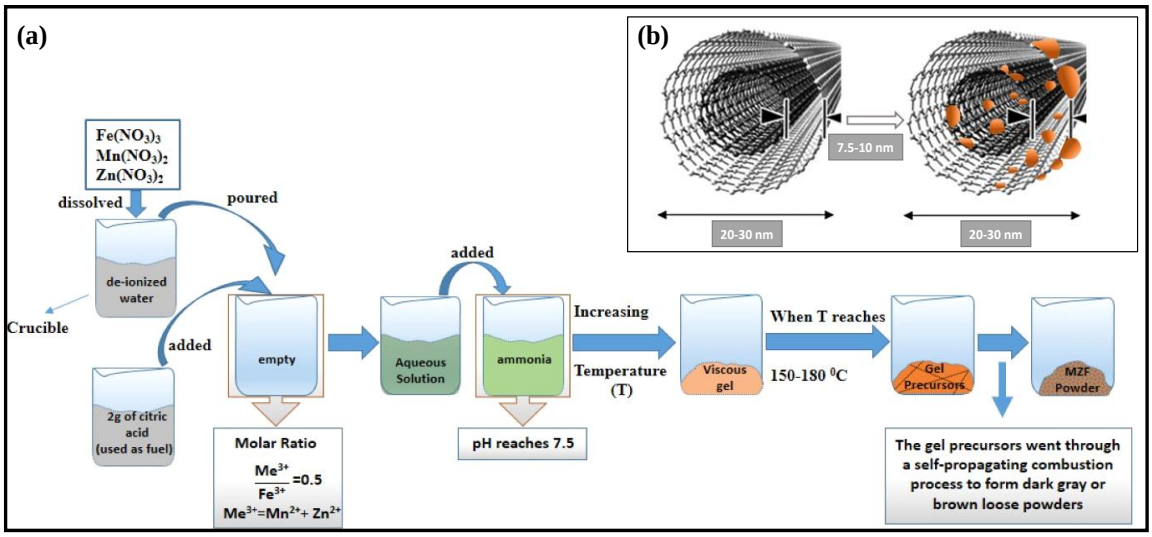

Figure 3.1 Schematic illustration of: (a) The preparation process of manganese and zinc ferrite nanoparticles (MZFs NPs); and (b) MZF NPs blended with multi-walled carbon nanotubes (MWCNTs).

A schematic illustration of MZF NPs blended with MWCNTs in a paraffin host matrix is presented in Fig. 3.1.

3.2.2 Preparation of Manganese and Zinc Ferrites (MZF)

Manganese and zinc ferrite particles in the present study were prepared by a citric acid assisted sol–gel method shown in Figure 1. The sol–gel method has a wide range of applications because of its high efficiency, large productivity, and low production temperatures and costs. Conventional industrial methods for the manufacturing of ceramic and glass need very high temperatures [66]. Therefore, in general, the sol–gel process is known as soft chemistry. In addition, the sol–gel method is a multipurpose process where the morphology, structure, and the composition of the final materials can be tuned by altering the hydrolysis and condensation reaction proportions [69]. Here, we have listed the steps of the sol–gel process, such as the homogeneous precursor solution with solid

materials, jellification, aging step, desiccation step, and densification step [70]. The procedure of material preparation as reported by Demir et al. [71] was followed exactly (for more details on material preparation, please consult [71]). A schematic representation of the synthesis of Mn–Zn ferrite powder particles is given in Fig. 3.1a.

3.2.3 Preparation of Nanocomposite Samples

Six different MWCNTs-based magnetic nanocomposites were prepared with various mass proportions using a binder matrix of paraffin through a simple and efficient process. Obtaining homogeneous samples is crucial for reliable microwave measurements. One important aspect in the use of nanoparticles in composites is a random dispersion inside the matrix with the goal of obtaining homogeneous samples. Furthermore, mixing filler nanoparticles within paraffin and eliminating air bubble formation inside the blend are required to obtain a homogeneous dispersion. The fillers of MWCNTs and MZF NPs were blended together in a proportion of 60 wt % (the total filling amount) with 40 wt % of molten paraffin. In the present work, six absorber samples with different compositions were prepared with the steps of 25%–50%–75% (three of them for the fillers of $MnFe_2O_4$, and three of them for the fillers of $ZnFe_2O_4$). The proportion details for all RAM specimens are shown in Table V. The process was carried out for the molten blend with the help of a “magnetic stirrer”, which includes a heating plate and which uses ultrasound waves to agitate particles. In the next step, the molten blend was poured into the sample holders, which were the same size as the waveguide cross-section.

TABLE V
THE PROPORTIONS USED FOR THE SAMPLE PREPARATION.

Sample Code	Components
#1	75 wt % (MWCNTs) with 25 wt % ($MnFe_2O_4$)
#2	50 wt % (MWCNTs) with 50 wt % ($MnFe_2O_4$)
#3	25 wt % (MWCNTs) with 75 wt % ($MnFe_2O_4$)
#4	75 wt % (MWCNTs) with 25 wt % ($ZnFe_2O_4$)
#5	50 wt % (MWCNTs) with 50 wt % ($ZnFe_2O_4$)
#6	25 wt % (MWCNTs) with 75 wt % ($ZnFe_2O_4$)

Another important practical aspect for solid materials is to eliminate the air gap between the sample and the sample holder. An air gap between them can be a substantial source of error unless the sample face and the edges of sample are machined as flat/fit as the inner walls of the sample holder [72]. For this step, the sample holders, including the molten blend, were flattened with a presser to avoid any airgaps in the waveguide system. Then, the samples were ready for the microwave measurements in Fig. 3.2 [73-75].

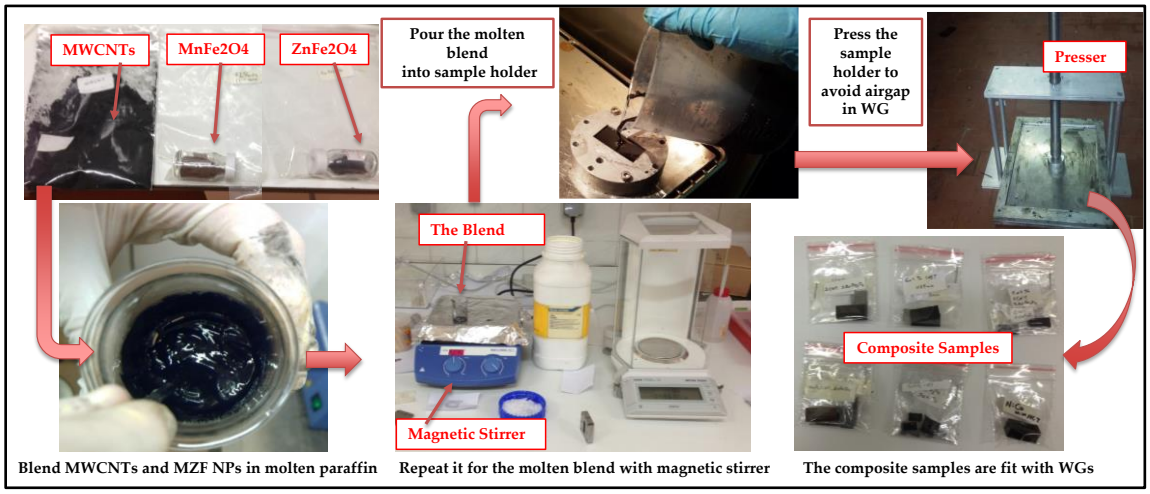

Figure 3.2 Schematic illustration of the manufacturing process of the samples.

3.2.4 Instrumentation

The crystalline structure of the resultant nanoparticles (MZF NPs) was characterized with an X-ray diffractometer (Rigaku D/Max—3C using Cu Kα radiation, Rigaku Innovative Technologies, Inc., Ettlingen, Germany) between 15 and 75 degrees in the 2θ range with a step size of 0.1 (2θ).

Fourier transform infrared (FT-IR) spectra of MZF NPs were carried out on a Bruker α-P by the attenuated total reflection (ATR) technique in transmission mode to explore the nature of the chemical bonds formed in the range between 4000 and 400 cm^{-1}.

By using a vibrating sample magnetometer (LDJ Electronics Inc., Model 9600, Troy, MI, USA), Vibrating Sample Magnetometry (VSM) measurements were done. An external field of up to 15 kOe at room temperature is applied to carry out the magnetization measurements.

Scanning electron microscopy (SEM), was used to observe the amount of deposited material as MZF NPs filler particles. By using a JEOL (JSM-7001F SEM-EDS-EBL, JOEL USA, Inc., Peabody, MA, USA) scanning electron microscope, the surface morphology of the samples was analyzed. SEM was operated at an accelerating voltage of 15 kV.

Energy-dispersive X-Ray spectroscopy (EDX) measurements were performed at 13 keV with INCA Instruments (Oxford Inca system, Oxford Co. Ltd., Belfast, UK).

Microwave S-parameter measurements were done in the 8.2–12.4 GHz frequency range at room temperature using the transmission line technique with an Agilent PNA E8364B network analyzer along with a waveguide system from Agilent (the specific waveguide model is WR90, Santa Rosa, CA, USA).

3.3 Results and Discussion

3.3.1 Morphology and Crystal Structure Characterization

The crystal structure of nanoparticles was identified with X-ray powder diffraction analysis, as shown in Fig. 3.3a and b. The particle sizes for both $MnFe_2O_4$ and $ZnFe_2O_4$ samples were calculated by the well-known Sherrer's formula [76] using the full width at half-maximum of intensity in the (400) plane of the spinel structure: L (nm) = $0.94\lambda/\beta\cos\theta_{hkl}$. Here, L is the average crystallite size, β is the full width of the relevant diffraction peak (FWHM), λ the X-ray wavelength (1.5418 Å), and θ_{hkl} is the angle of the diffraction peaks. The experimental lattice constants (a_{exp}) were calculated with the inter-planner distances; d_{hkl}-values and Miller indices (hkl) based on Bragg's equation:

$$n\lambda = 2d_{hkl}\sin\theta_{hkl} \tag{3.1}$$

$$1/d_{hkl}^2 = \left(h^2 + k^2 + l^2\right)/\left(a_{\exp}\right)^2 \tag{3.2}$$

The diffraction peaks at 29.7°, 35.5°, 36.6°, 42.97°, 53.8°, 57.4°, and 62.65° could be assigned from Fig. 3.3a, which correspond to (220), (311), (222), (400), (422), (511), and (440) planes of $MnFe_2O_4$, respectively. As shown in Fig. 3.3a, the peaks were in good agreement with the standard $MnFe_2O_4$ card (JCPDS cards No. 74-2403, 74-2402, 10-0319), which indicate the samples had a face-centered cubic crystal structure. No secondary impurity phase was detected, hence, the absence of any additional peaks assigned to the graphite plane of MWCNTs. This means MWCNTs with ferrite nano-particles are relatively coated. The broadening of the diffraction peaks indicates the nano-crystalline nature of the materials. As shown in Fig. 3.3a, the XRD peaks marked (*) at 21.46° and 23.82° were caused by the paraffin because of its regular crystallization [37].

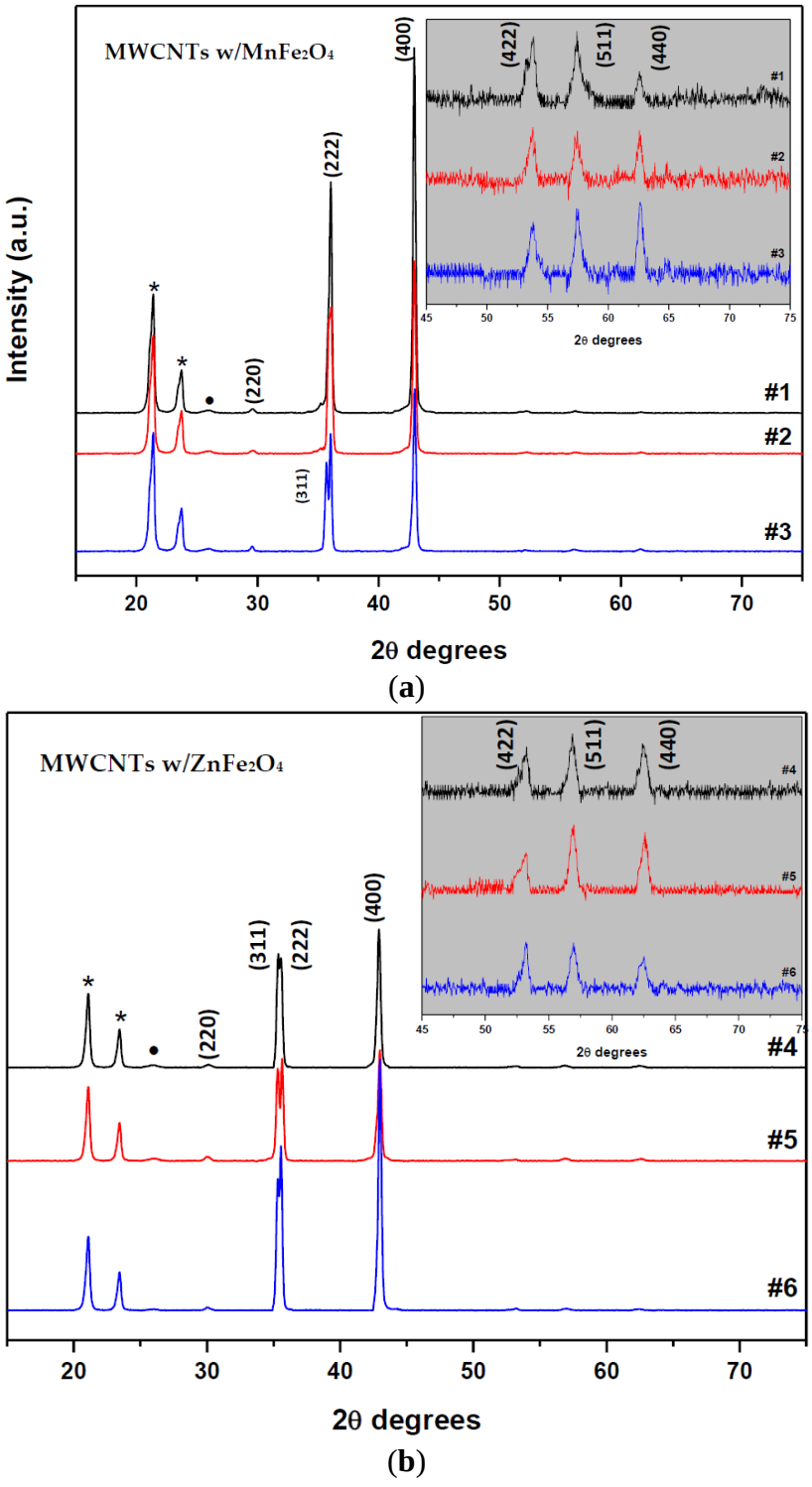

Figure 3.3 XRD patterns of samples fabricated with MZF NPs by blending commercial multi-walled carbon nanotubes (MWCNTs) according to the mass fractions: (a) MWCNTs with $MnFe_2O_4$ samples; and (b) MWCNTs with $ZnFe_2O_4$ samples.

The calculated mean crystallite size value of $MnFe_2O_4$ is found to be about 22 nm. The lattice constant (a_{exp}) was calculated and found to be 8.4215 ± 0.0006.

The diffraction peaks at 30°, 35.3°, 35.5°, 42.9°, 53.2°, 56.9°, and 62.5° could be assigned from Fig. 3.3b, which correspond to (220), (311), (222), (400), (422), (511), and (440) planes of $ZnFe_2O_4$, respectively. As shown in Fig 3.3b, the peaks were in good agreement with the standard $ZnFe_2O_4$ card (JCPDS cards No. 82-1042, 82-1012, 79-1150, and reference code 01-089-4926), indicating the samples had face centered cubic crystal structure. As shown in Fig. 3.3b, the XRD peaks marked (*) at 21.4° and 23.8° were caused by the paraffin due to its regular crystallization. An additional peak, the peak marked (•), was detected at 25.98° which corresponds to (002) planes of the MWCNTs. The calculated mean crystallite size value of $ZnFe_2O_4$ found to be about 29 nm. The lattice constant (a_{exp}) was calculated and found to be 8.4306 ± 0.003 Å.

3.3.2 Fourier Transform Infrared (FT-IR) Analysis

The FT-IR spectra of the synthesized $Mn_{1-x}Zn_xFe_2O_4$ NPs are presented with a step size of 0.2 (x = 0:0.2:1) in Fig. 3.4, including the band positions of the investigated samples (just $MnFe_2O_4$ and $ZnFe_2O_4$) shown in Table VI. The FT-IR spectra has been discussed extensively in [71] and all details on the other step sizes of the FT-IR spectra are found therein. According to the geometrical configuration of the oxygen nearest neighbors in ferrites, the metal ions are located in two different sub-lattices. They are also designated as tetrahedral and octahedral sites [77]. The specimens contained insignificant amounts of organic residue, as shown in Fig. 3.4.

TABLE VI
VIBRATION FREQUENCIES OF THE SAMPLES

Sample	Tetrahedral	Octahedral
$MnFe_2O_4$	433	535
$ZnFe_2O_4$	430	528

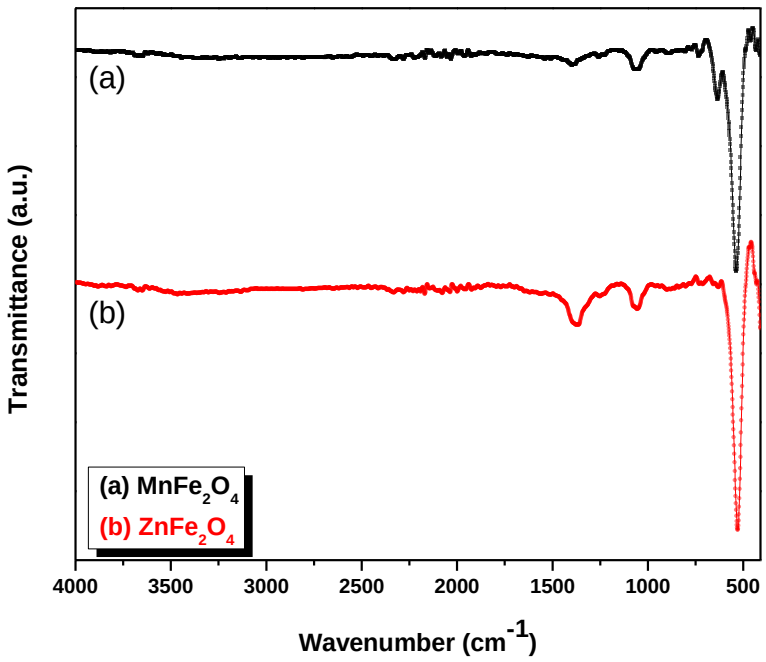

Figure 3.4 Fourier transform infrared (FT-IR) spectra of $Mn_{1-x}Zn_xFe_2O_4$ NPs for (a) $MnFe_2O_4$; and (b) $ZnFe_2O_4$.

The characteristic peaks of $MnFe_2O_4$ for Mn–O, ZnO and Fe–O bond stretching vibrations can be clearly observed at wave numbers 560 cm^{-1} in Fig. 3.4 [78, 79]. The peaks at 1380 and 1600 cm^{-1} are attributed to the C=O stretching modes, respectively, because of the coordination of the carboxylate groups of the citric acid by metal ions. It is believed that the observed two peaks on the left of the 600 cm^{-1} wavenumber belong to organic residues, which were used as fuel during the synthesis.

3.3.3 The Magnetization Measurements (VSM Analysis)

Magnetization curves (M versus H) of MZF NPs were measured at room temperature with an applied field of ±15 kOe. Fig. 3.5b,c show the enlarged views in ±1.5 kOe demonstrating the hysteresis behavior for the synthesized $MnFe_2O_4$ and $ZnFe_2O_4$. The values of M_r, M_s, and H_c were determined versus Zn mole concentrations depending on $Mn_{1-x}Zn_xFe_2O_4$ formula with a step size of 0.2 (0:0.2:1). Here, the values for just the synthesized $MnFe_2O_4$ and $ZnFe_2O_4$ NPs have been reported. The values of saturation magnetization (M_s), coercivity (H_c), and remnant magnetization (Mr) are determined from hysteresis loops. They are listed in Table VII.

The results from the hysteresis loops indicated that all of the composite magnetic spheres were magnetically soft at room temperature, when an external field was applied (Fig. 3.5).

TABLE VII
MAGNETIC PROPERTIES OF THE SYNTHESIZED SPECIMENS

Sample	M_s	H_c	M_r	M_r/M_s
$MnFe_2O_4$	70.52	57	9.72	0.137
$ZnFe_2O_4$	35.90	50	4.03	0.112

Due to these values, it can be argued that all samples exhibited super-paramagnetic behavior at room temperature. The observed M_s and M_r values of $MnFe_2O_4$ NPs were higher than those for $ZnFe_2O_4$ NPs. It can be explained by noting that Zn has no net magnetic moment. The values of M_s of $MnFe_2O_4$ are lower than the reported values for bulk $MnFe_2O_4$ (80 emu/g) [80, 81]. Such behavior is ascribed to surface effects in nanoparticles. The values of M_s of $ZnFe_2O_4$ particles was much higher than the bulk M_s

values of 5 emu/g [82]. Such behavior is related to cation distribution, which can change from a normal spinel structure to a mixed spinel structure [71].

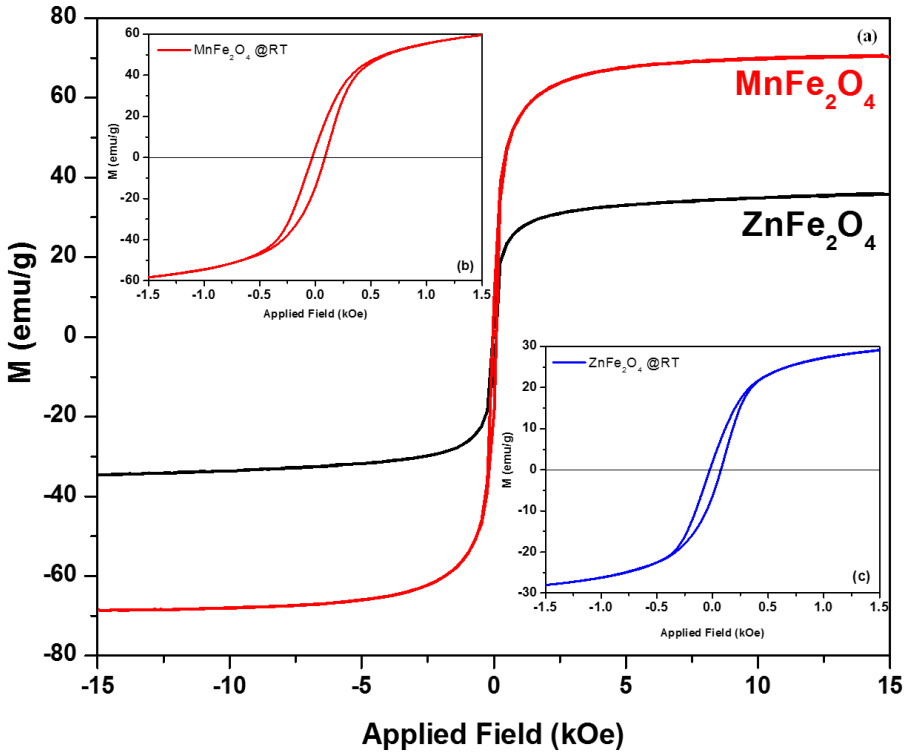

Figure 3.5 (a) Magnetic hysteresis loops of $Mn_{1-x}Zn_xFe_2O_4$ NPs. The close up views for the M–H curves of (b) $MnFe_2O_4$; and (c) $ZnFe_2O_4$.

3.3.4 The Surface Morphology of the Samples (SEM) Analysis and The Energy Dispersive X-Ray (EDX)

SEM images of the nano-structured specimens are shown in Fig. 3.6, which demonstrates the dispersion of MWCNTs particles and $MnFe_2O_4$ NPs as well as $ZnFe_2O_4$ NPs. The fillers were dispersed randomly in the host matrix. In addition, it is clearly seen that some of MWCNTs were coated/filled with MZF NPs. This result agrees with the XRD results, where the absence of any additional peaks implies that MWCNTs were coated with spinel ferrite nanoparticles.

The EDX technique provides the effective atomic concentration of different components in the top surface layers of solids. The energy dispersive X-ray (EDX) analysis of the specimens, as shown in Fig. 3.7, was carried out to confirm the elemental composition of the specimens. The EDX spectrum confirms the presence of Mn, Fe, C, and O elementals, as well as Zn, Fe, C, and O elementals for the samples of $MnFe_2O_4$ with MWCNTs and $ZnFe_2O_4$ with MWCNTs, respectively. The other minor peaks might be due to the impurities in the starting materials. The relative atomic and weight abundance of Mn, Zn, Fe, and O species are presented in the tables on each EDX graph. The atomic ratios of Fe/Mn and Fe/Zn, found to be 2:1 by EDX analyses, confirmed the presence of $MnFe_2O_4$ and $ZnFe_2O_4$ nanoparticles on the MWCNT surfaces.

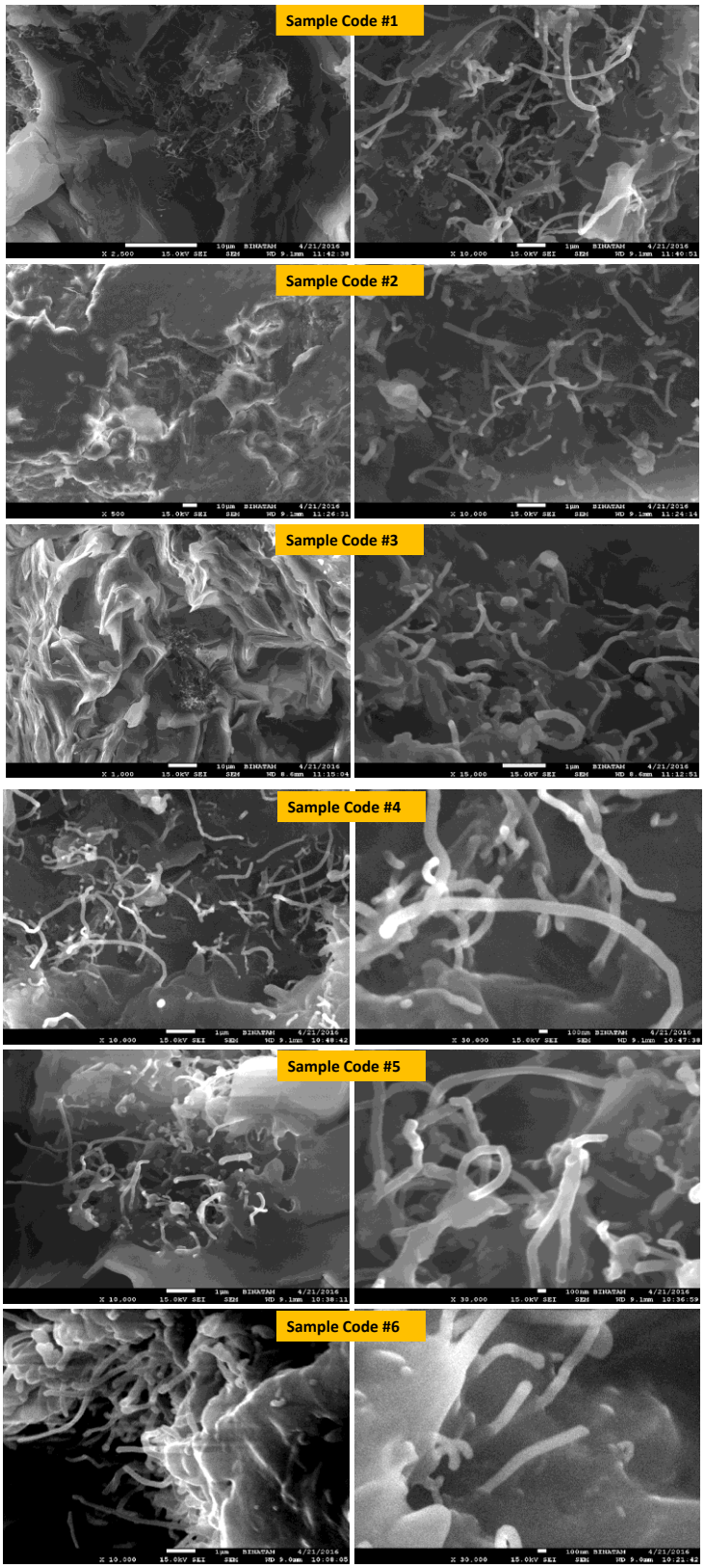

Figure 3.6 SEM micrographs of the specimens including $MnFe_2O_4$ and $ZnFe_2O_4$ blended with MWCNTs.

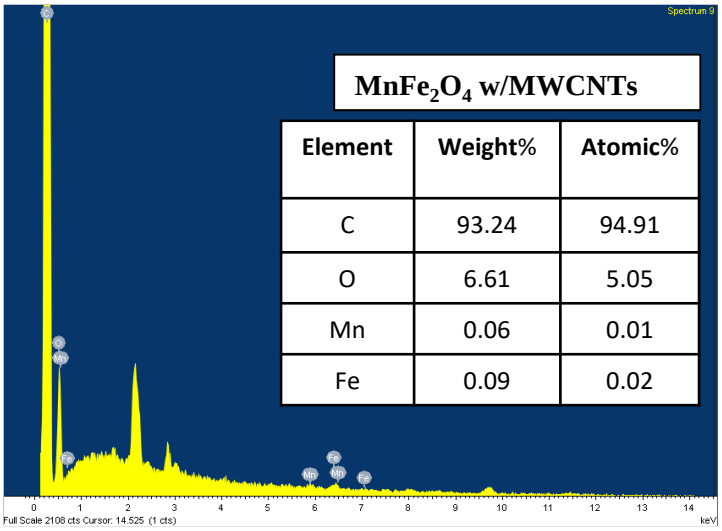

(a)

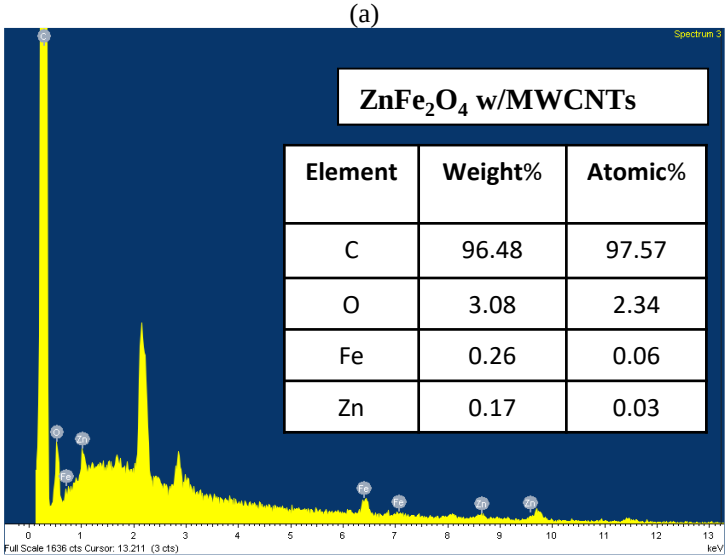

(b)

Figure 3.7 EDX spectrum of: (a) $MnFe_2O_4$ magnetic nanoparticles on multi-walled carbon nanotubes; and (b) $ZnFe_2O_4$ magnetic nanoparticles on multi-walled carbon nanotubes.

3.3.5 Electromagnetic Constitutive Parameters

The values of electromagnetic complex permittivity and permeability were calculated from the scattering parameters, such as S_{11} and S_{21}, using the transmission line method with the Nicolson–Ross–Weir algorithm [4]. Reflection coefficient Γ is given by $\Gamma = K \pm \sqrt{(K^2 - 1)}$ where $K = [(S_{11}^2 - S_{21}^2) + 1]/2S_{11}$. The transmission coefficient T is

given by $T = [(S_{11} + S_{21}) - \Gamma]/[1 - (S_{11} + S_{21})\Gamma]$. The permittivity and the permeability are calculated [4] from:

$$\mu_r = \frac{1+\Gamma}{(1-\Gamma)\Lambda\sqrt{\left[\left(1/\lambda_0^2\right)-\left(1/\lambda_c^2\right)\right]}} \tag{1.3}$$

$$\varepsilon_r = \frac{\lambda_0^2}{\mu_r\left[\left(1/\lambda_c^2\right)-\left(1/\Lambda^2\right)\right]} \tag{3.4}$$

$$\frac{1}{\Lambda^2} = -\left[\frac{1}{2\pi d}\ln\left(\frac{1}{T}\right)\right]^2 \tag{3.5}$$

where λ_0 is the wavelength of free-space; λ_c is the cut-off wavelength of the transmission line. The schematic illustration of microwaves transmitting through, and reflecting from, a sample in a waveguide transmission line is represented in Fig. 3.8.

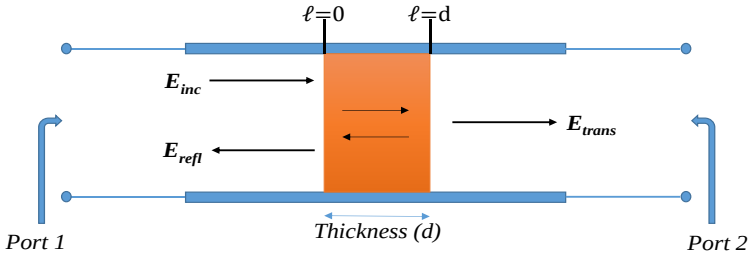

Figure 3.8 Schematic illustration of electromagnetic waves transmitting through and reflecting from a sample in a transmission line (such as a waveguide).

The complex constitutive parameters (dielectric permittivity and magnetic permeability) denote the dielectric and magnetic properties of materials as RAMs. The real components (ε_r' and μ_r') of the electromagnetic constitutive parameters represent the storage capability of electric and magnetic energy. Energy loss in materials is due to the imaginary part of the complex permittivity and complex permeability (ε_r" and μ_r"). Magnetic losses are more effective and sensitive than dielectric losses for microwave

absorption. A small differences in permeability can even affect the microwave absorption properties of the materials [83].

Fig. 3.9 and 3.10 show the real and the imaginary parts of the relative permittivity and permeability of five different compositions of Mn or Zn ferrite and MWCNTs alloys, namely in 25% increments of weight ratios.

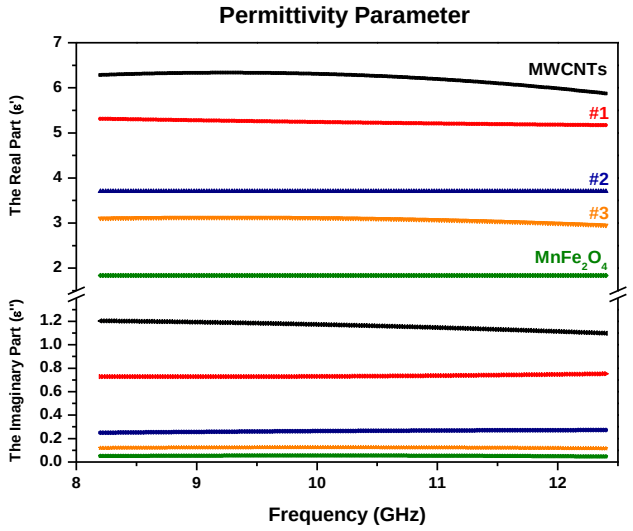

(a)

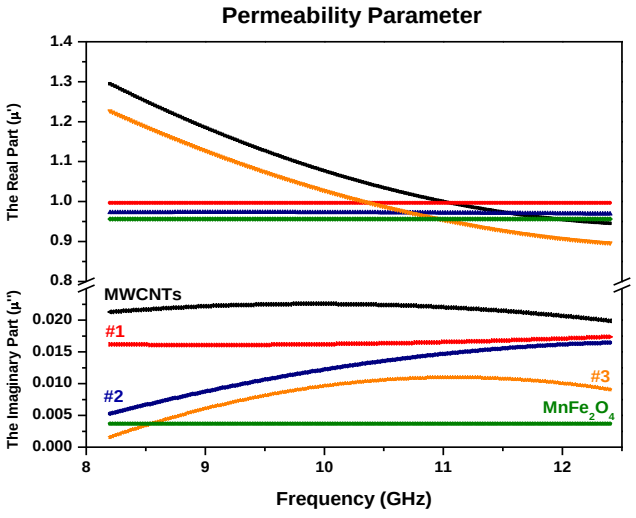

(b)

Figure 3.9 Electromagnetic constitutive parameters with (a) the real and imaginary part of permittivity for MWCNTs with $MnFe_2O_4$ samples; and (b) the real and imaginary part of permeability for MWCNTs with $MnFe_2O_4$ samples *(*samples are color-coded*).*

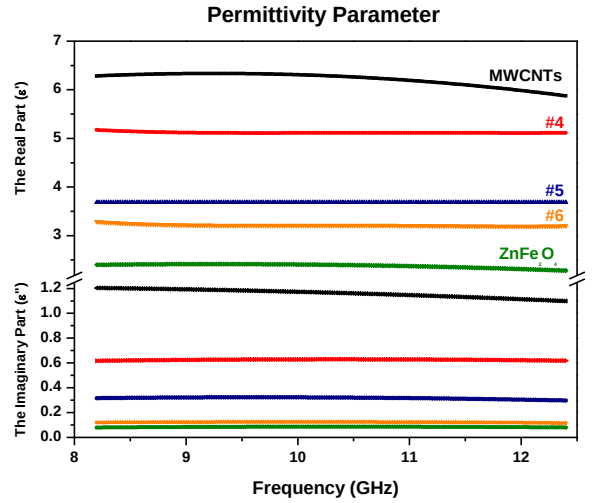

(a)

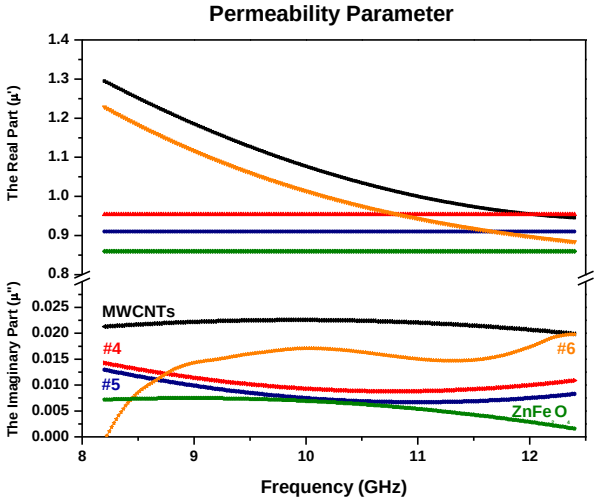

(b)

Figure 3.10 Electromagnetic constitutive parameters with (a) the real and imaginary part of permittivity for MWCNTs with $ZnFe_2O_4$ samples; (b) the real and imaginary part of permeability for MWCNTs with $ZnFe_2O_4$ samples (samples are color-coded).

As shown in Fig. 3.9a and 3.10a, the real part of the permittivity of the specimens remained almost constant in the whole frequency range. The constancy means that there was a dominant polarization, in which the oscillation of the electric dipole moments was in phase or somewhat out of phase with the microwave frequencies [84]. Moreover, the atomic and electronic polarizations may take place within a period shorter than the period of a microwave signal. Both the direct current conductivity and the alternating current

conductivity may cause the dielectric loss of the materials. It can be seen clearly by the following equation:

$$\varepsilon'' = \sigma_{dc} \Big/ \left(\omega \varepsilon_0\right) + \varepsilon_{ac} \tag{3.6}$$

It appears that the direct current conduction loss is inversely proportional to the frequency; hence, the reason for the increase in ε″ for pure MWCNTs with decreasing frequency at lower frequencies. In addition, it is noted that decreasing the loading amount of MWCNTs in the composites, the values of the real and the imaginary part of permittivity (ε′) decreased for both samples of MWCNTs with $MnFe_2O_4$ and $ZnFe_2O_4$.

Figures 9b, 10b, and 11 show the frequency dependence of the relative complex permeability for the samples. It can be seen that the real part and the imaginary part of permeability values (μ' and μ″) lie in the ranges 0.8–1.3 and 0–0.02, respectively. The small values of the latter suggest that the magnetic loss has a low contribution to electromagnetic wave attenuation. In general, the magnetic loss of magnetic materials can be predicted from magnetic hysteresis, eddy current loss, domain wall resonance, neutral resonance, as well as exchange resonance. The eddy current loss is related to the electrical conductivity and the thickness of the samples. It can be expressed by X_{eddy} [85]:

$$X_{eddy} = \mu'' \Big/ f\,(\mu')^2 = 2\pi\mu_0\sigma d^2 \tag{3.7}$$

where μ_0 is the permeability value of a vacuum and σ is the electric conductivity of the material. For the samples here, the eddy-current loss effect is negligible. That means the eddy current loss has no significant effect in terms of microwave absorption properties.

It may be noted that the practical performance (RL value) of a RAM also requires good impedance matching properties between air and the material (Section 3.3.6), which, in turn, are associated with the resultant complex permittivity and permeability. Small

differences in permeability can even affect the microwave absorption properties of the materials [86]. It will be seen later that the magnetic characteristics contributed well to the RL values in Fig. 3.12.

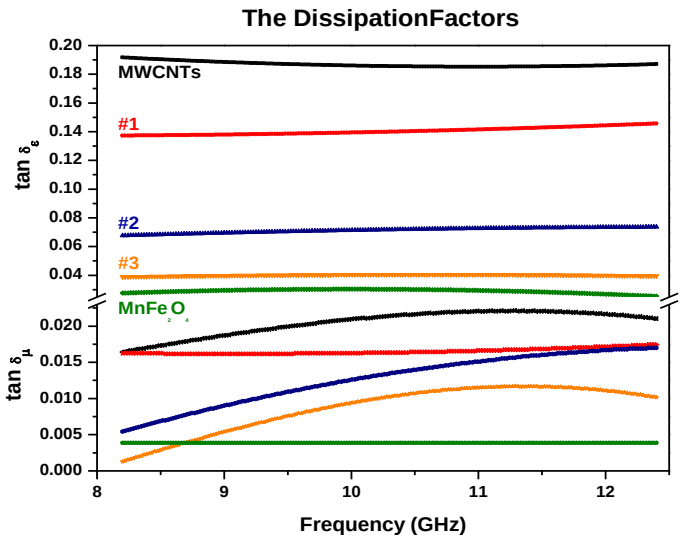

(a)

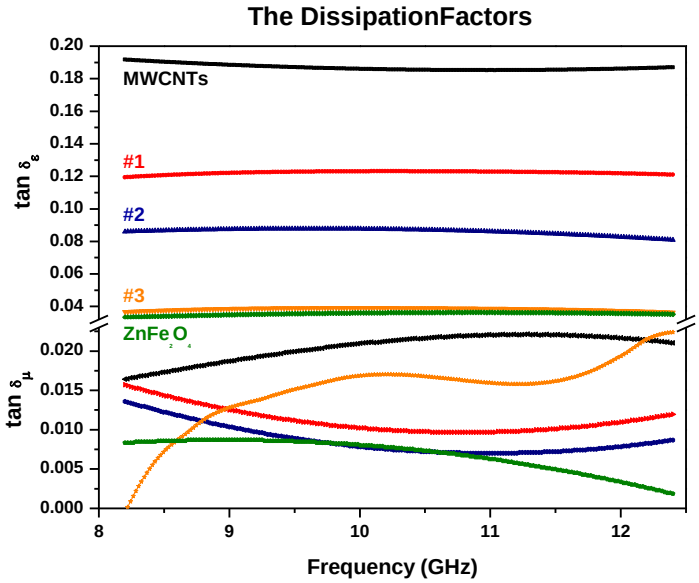

(b)

Figure 3.11 The dielectric and magnetic dissipation factors with (a) MWCNTs with $MnFe_2O_4$ samples; (b) MWCNTs with $ZnFe_2O_4$ samples *(*samples are color-coded*)*.

The dielectric ($\tan(\delta_\varepsilon) = \varepsilon_r''/\varepsilon_r'$) and magnetic ($\tan(\delta_\mu) = \mu_r''/\mu_r'$) dissipation factors are represented in Fig. 3.11a, and b. It is noted that the values of the magnetic dissipation

factors are generally less than the dielectric dissipation factors for the MWCNTs with $MnFe_2O_4$ samples, which means that the absorption originates mainly from the dielectric characteristics of MWCNTs with $MnFe_2O_4$ and $ZnFe_2O_4$ nanoparticles rather than the magnetic characteristics.

In our case, dielectric mechanisms or polarization effects that contribute to its overall complex permittivity may be used to explain why dielectric dissipation factors are more significant than the magnetic dissipation factors. Once an electric field is applied, positive and/or negative charges move in opposite directions, which contributes to the dominant dipole polarization. The number of surface atoms with unsaturated bonds in Mn, Zn, and Fe will increase as their sizes are at the nanoscale, resulting in an increase in dipole polarization. The increased dipole polarization can contribute to the dielectric dissipation factors (or dielectric loss). Another possible contribution to the dielectric dissipation is a reasonable distribution of MZF NPs in MWCNTs. That can introduce extra interfaces resulting in interfacial polarization. In addition, relaxation may occur at the MZF NPs/MWCNTs interfaces, which contributes to the dielectric loss [87]. The space-charge polarization can contribute an extra relaxation, resulting in an increase of the dielectric loss to some degree [88]. For ferrite materials, it should be noted the value of ε' is considerably bigger than that of μ', which is related to loss tangent factors [89].

The permeability graphs do not show an ordered structure as compare with the permittivity parameters because Zn has no magnetic moment.

3.3.6 Microwave Absorption Properties

The return loss (RL) curves of the conductor-backed samples was obtained from the following equation [2, 90]:

$$RL\,(dB) = -20\log\left|\left(Z_{in} - Z_0\right)\Big/\left(Z_{in} + Z_0\right)\right| \tag{8}$$

Here, the effective input impedance of the sample is $Z_{\text{in}} = Z_0\sqrt{\mu_r/\varepsilon_r}\tanh[(-\mathrm{j}\,2\pi/c)fd\sqrt{\mu_r\varepsilon_r}]$, where μ_r and ε_r are the relative complex permeability and permittivity, respectively, c is the speed of light, f is the frequency, and d is the thickness of each sample.

The computed return loss (RL) for the various compositions of synthesized MZF NPs in/on MWCNTs samples of approximately the same thickness (3 mm) is shown in Fig. 3.12. The lowest RL value and the bandwidth change with different loadings of manganese and zinc spinel ferrite nanoparticles. A minimum RL of −56 dB at 11.41 GHz with a bandwidth of 3.38 GHz (RL < −20 dB) was obtained in MWCNTs with $MnFe_2O_4$ NPs (x = 0.0). A minimum RL of −42.06 dB at 11.05 GHz with an absorption bandwidth of 3.34 GHz (RL < −20 dB) was observed in MWCNTs with $ZnFe_2O_4$ NPs (x = 1.0). These results are summarized in Table VIII.

TABLE VIII
SAMPLE CODES AND ABSORPTION RESULTS

Code	f_r (GHz)	Return Loss (dB)	Bandwidth (GHz) (under −20 dB)
Sample #1	10.44	−32.84	1.88 (9.42–11.3)
Sample #2	11.00	−41.20	2.2 (9.84–12.04)
Sample #3	11.41	−56.00	3.38 (9.7–13.08)
Sample #4	-	-	-
Sample #5	11.05	−42.06	3.34 (9.38–12.72)
Sample #6	10.55	−36.72	2.8 (9.00–11.80)

The table contains the sample codes, the center frequencies (f_r), the values of minimum achievable return loss (dB), and the corresponding bandwidths (GHz). It should be noted that the dips in the values of RL versus frequency indicate low reflectivity (or a good microwave absorption). Furthermore, the minimum RL values shifted to higher frequencies and the bandwidths increased with an increasing amount of (manganese) ferrite material in the blend (Samples #1, #2, and #3 in Fig. 3.12a). However, the minimum RL values shifted to lower frequencies with an increasing amount of (zinc) ferrite material in the blend (Samples #5 and #6 in Fig. 3.12b).

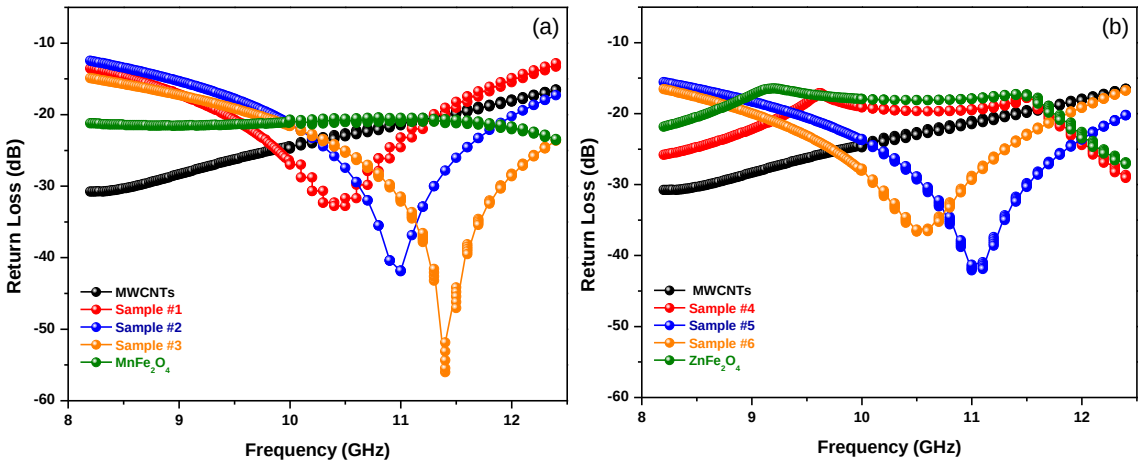

Figure 3.12 Frequency dependence of the return loss (RL) of MWCNTs with MZF NPs alloys; (a) MWCNTs with $MnFe_2O_4$ samples; and (b) MWCNTs with $ZnFe_2O_4$ samples.

In comparison, our previous article [62] reported an RL of −38 dB with a bandwidth of 2 GHz at 16 GHz for a purely magnetic absorbing material. In addition, the results show that the dielectric (MWCNTs) materials and the magnetic materials (MZF NPs) can mutually reinforce in terms of enhancing microwave absorption properties at microwave frequencies. In order to investigate the claim that dielectric or magnetic materials by themselves have relatively low RL values, dielectric samples (only MWCNTs

samples in the same wt % of total concentration of Samples #1, #2, and #3) were prepared and the values of their RL versus frequency were computed. It was observed form Fig. 3.12a and 3.12b that dielectric or magnetic materials have low RL performance when they are used by themselves.

The results of these composite samples showed that the microwave absorption is enhanced once the dielectric and the magnetic materials are combined. In the literature, there exist similar studies such as those for graphene oxide/strontium ferrite/polyaniline (R-GOSF/PANI) [99]. The authors investigated samples of R-GOSF/PANI with different weight ratios of GO and SF. Their results also exhibited the synergic effect between R-GO (as dielectric materials) and strontium ferrite (as magnetic materials) in enhancing the microwave absorption properties of the samples.

3.4 Conclusion

In this chapter, the synthesized Mn–Zn ferrites in/on MWCNTs with different weight ratios were investigated. All synthesized samples exhibit super-paramagnetic behavior at room temperature. XRD patterns are in good agreement with the JCPDS cards. No secondary impurity phase was detected. The absence of any additional peaks attributed to the graphite plane of MWCNTs, which indicated MWCNTs with ferrite nano-particles are relatively coated. The return loss (RL) results show that the microwave absorption properties of MWCNTs were enhanced by blending with magnetic materials. The minimum RL value shifted to higher frequencies with an increasing amount of manganese ferrite material in the blend. However, the minimum RL value tends to shift to lower frequencies with an increasing amount of zinc ferrite material in the blend.

This page intentionally left blank

Chapter 4

The Measurement of Microwave Absorption Characteristics of Nanocomposites Using a Coaxial Line Technique

4. The Measurement of Microwave Absorption Characteristics of Nanocomposites Using A Coaxial Line Technique

Microwave absorption properties (MAP) of manganese soft spinel ferrite ($MnFe_2O_4$) nanoparticles (MSF NPs) mixed with multi-walled carbon nanotubes (MWCNTs) and molded as toroid-shaped pellets were experimentally studied using a coaxial line technique in the frequency range of 2-18 GHz in this chapter. The coaxial line technique was used because of the smaller sample size, a wider frequency range, and a uniform cross section. The MAP were derived from the measured constitutive parameters, according to the transmission line theory.

4.1 Introduction

It has been reported that, in applications requiring radar absorbing materials (RAM), both dielectric and magnetic materials have relatively low microwave absorption when they are used by themselves [91, 92]. It is possible to enhance absorption characteristics when magnetic powder nanoparticles are blended with dielectric nanomaterials [2]. For microwave absorption properties measurements, there exist several different techniques such as waveguide, coaxial line, resonant cavity, and free-space[2, 59, 93-95]. In this study, we have adopted a reflection/transmission technique in a coaxial line because of the smaller sample size, a wider frequency range, and a uniform sample cross section. The coaxial line is especially suitable for solid (powder) materials. The method is also preferable for measurements on powder samples because it uses less paraffin in the sample than the waveguide method.

4.2 Fabrication and Measurement Setup

4.2.1 Preparation of Manganese Spinel Ferrite Nanoparticles (MSF NPs) and the other additives of composites

Manganese and Zinc ferrite particles in the present study were prepared by a citric acid assisted sol-gel method using a procedure reported by Demir et al. [71]and Teber et al [2]. The steps of the sol-gel process are the formation of the homogeneous precursor solution, sol, gel, aging, desiccation, and densification. MWCNTs were used as dielectric materials in order to create conductive paths within composite samples. The MWCNTs were purchased from US Research Nanomaterials, Inc., USA.

4.2.2 Fabrication of Nanocomposite Samples

For coaxial line measurements, the samples have to have a toroidal shape. The material must fit tightly in the sample holder in order to reduce the measurement uncertainty caused by air gaps. We designed our own manufacturing setup as shown in Fig. 4.1a.

The dielectric and magnetic nanoparticles were blended in a crucible with paraffin, and then the process was repeated for the molten blend with the help of a magnetic stirrer, which includes a heating plate and uses ultrasound waves to agitate particles. The molten blends were uniformly dispersed by stirring at 1000 rpm for 30 seconds. In the next step, the molten blend was poured into the sample holders, which are the same size as a coaxial line cross section. The blends in the sample holder were pre-cured at room temperature for half an hour. For the last step, the sample holders

including the pre-cured blends were flattened with a presser to avoid any air gaps in the coaxial line system. The composite samples were fabricated into toroid-shaped samples with an inner diameter of 3.5mm, an outer diameter of 7mm, and a thickness of 3mm. A gold plated coaxial airline with a precision 7mm connector was used to hold the sample [51, 96]. Then, the samples were ready for the microwave measurements of Fig. 4.1c.

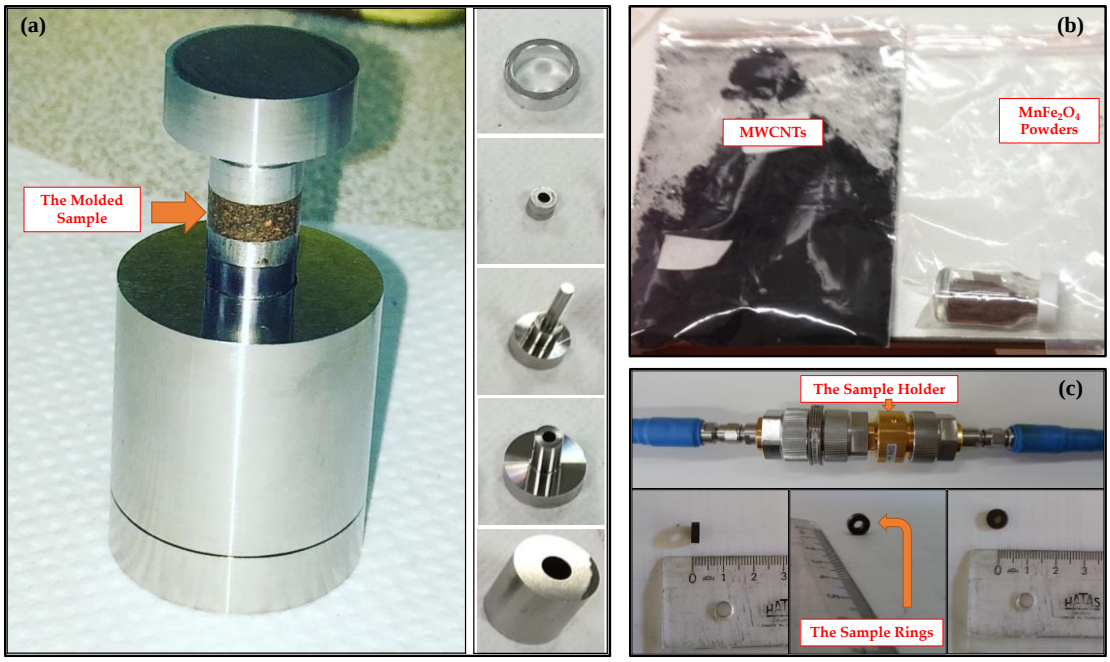

Figure 4.1 (a) The manufacturing mold system; (b) The powders of MWCNTs, manganese spinel ferrites spinel ferrites; (c) The toroidal shape of the samples.

Three different samples (MWCNTs-based magnetic nanocomposites of MSF NPs) were fabricated by incorporating in a proportion of 80 wt. percentage (the total filling amount) into 20 wt. percentage of a host matrix of molten paraffin. The filler materials (ferrite particles and MWCNTs) were blended in various mass proportions with the steps of 25-50-75%.

4.2.3 The Method of Microwave Measurements

4.2.3.1 Coaxial Line Measurements

The complex scattering parameters corresponding to reflection (S_{11}) and transmission (S_{21}) parameters of a transverse electromagnetic (TEM) wave were measured using a vector network analyzer (Agilent PNAE8364B) in conjunction with a coaxial line system (Keysight Tech. 85050C 7mm coaxial connectors) incorporating samples of MSF NPs blended with MWCNTs for the frequency range of 2-18 GHz. Then, the electromagnetic constitutive parameters (ε and μ) were extracted from s-parameters using the material measurement software of 85071E (Keysight Tech.). In addition, the return loss (RL) of the samples was estimated from the computed complex permittivity and permeability values in order to assess their suitability as microwave absorbing materials. Fig. 2 indicates that the sample is placed between two parts of the coaxial line using a sample holder.

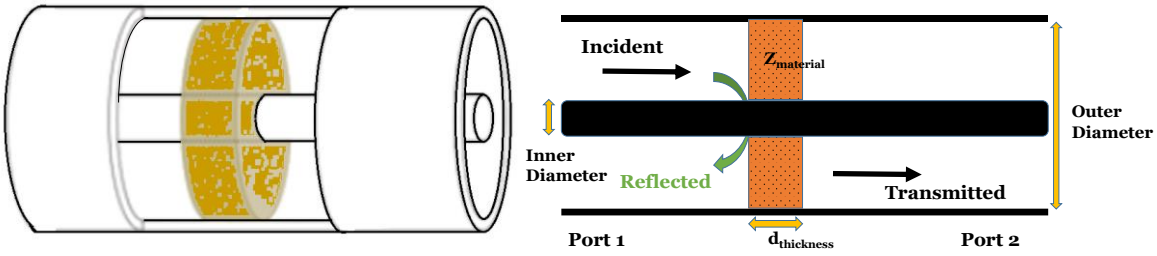

Figure 4.2 The Measurement schematic of (a) Coaxial line and sample (b) the side view of measurement setup.

4.2.3.2 The Computation of Return Loss

The microwave absorption properties of the absorber samples can be defined by the reflection loss (RL). The RL of a ground-plane-backed samples can be calculated

from the measured values of complex relative permittivity and permeability for the given frequency and absorber thickness using the following equations:

$$RL\,(dB) = -20\log\left|\frac{(Z_{in}-1)}{(Z_{in}+1)}\right| \tag{4.1}$$

while the normalized input impedance (Zin) is calculated by:

$$Z_{in} = \sqrt{\frac{\mu_r}{\varepsilon_r}}\tanh\left(-j\frac{2\pi fd}{c}\sqrt{\mu_r\varepsilon_r}\right) \tag{4.2}$$

where f is the microwave frequency, d is the thickness of the sample, and c is the velocity of electromagnetic wave in a vacuum. ε_r and μ_r are the complex relative permittivity and permeability, respectively, which can be calculated by ε_r (= ε' - jε'') and μ_r (= μ' - jμ'').

4.3 Results and Discussion

4.3.1 The Structure and Morphology of the Samples and the Energy Dispersive X-Ray (EDX)

The crystal phases of the resultant composites were investigated using the model of Rigaku D/Max-3C using CuKα radiation (Rigaku Innovative Technologies, Inc., Germany) in the 2θ range of 20-80^0 with a step size of 0.1 (Fig. 4.3).

Fig. 4.4 shows the SEM images of the nano-structured samples, which demonstrates the dispersion of MWCNTs particles and $MnFe_2O_4$ NPs. The morphology features of the nanocomposites were characterized by scanning electron microscopy (SEM) with the model of JSM-7001F SEM-EDS-EBL, JOEL USA, Inc., MA,USA, that operated with an accelerating voltage of 5kV as well as the different magnification from 100x (200μm) to 2000x (10μm).

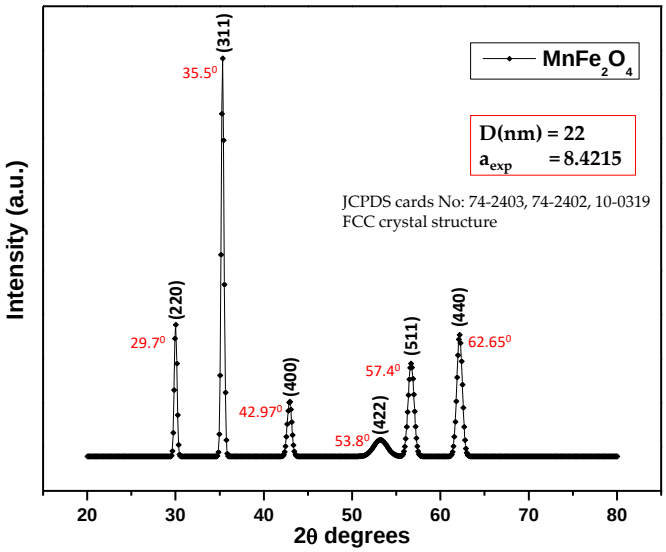

Figure 4.3 XRD patterns of samples fabricated with MZF NPs by blending MWCNTs.

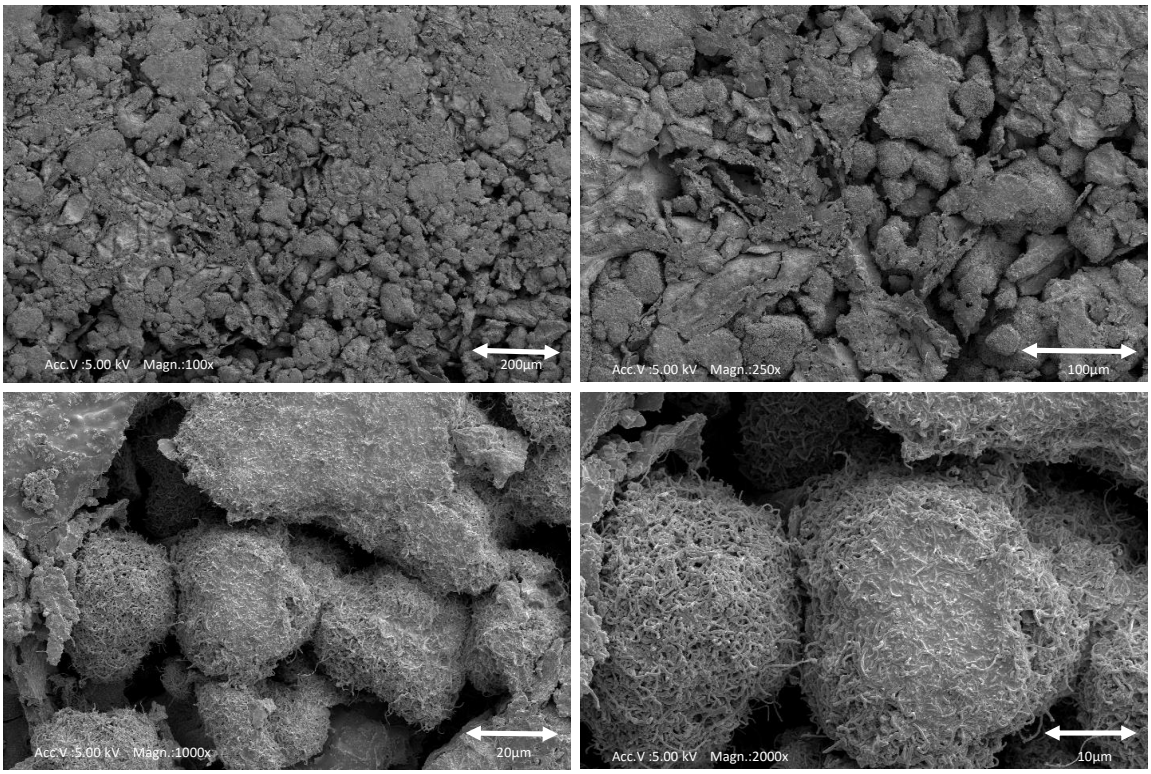

Figure 4.4 The Surface Morphology of the specimens ($MnFe_2O_4$ blended with MWCNTs).

SEM was examined observing the amount of deposited filler nanoparticles of manganese spinel ferrites and MWCNTs. The fillers were dispersed randomly in the host

matrix. In addition, it is clearly seen that some of MWCNTs were coated/filled with MSF NPs. This result agrees with the XRD results, where the absence of any additional peaks implies that MWCNTs were coated with spinel ferrite nanoparticles.

Fig. 4.5 shows the EDX technique supplies the effective atomic concentration of different constituents in the top surface layers of solids. The energy dispersive X-ray (EDX) analysis of the specimens was carried out to confirm the elemental composition of the specimens. Energy-dispersive X-Ray spectroscopy (EDX) measurements were employed at 10 keV with INCA Instruments (Oxford Inca System, Oxford Co. Ltd., UK). The EDX spectrum confirms the presence of Mn, Fe, C, and O elementals for the samples of $MnFe_2O_4$ with MWCNTs. The other minor peaks might be due to the impurities in the starting materials. The relative atomic and weight abundance of Mn, Fe, and Oxygen species are presented in the table on EDX graph. The atomic ratios of Fe/Mn are found to be 2:1 by EDX analyses, confirmed the presence of $MnFe_2O_4$ nanoparticles on the MWCNT surfaces.

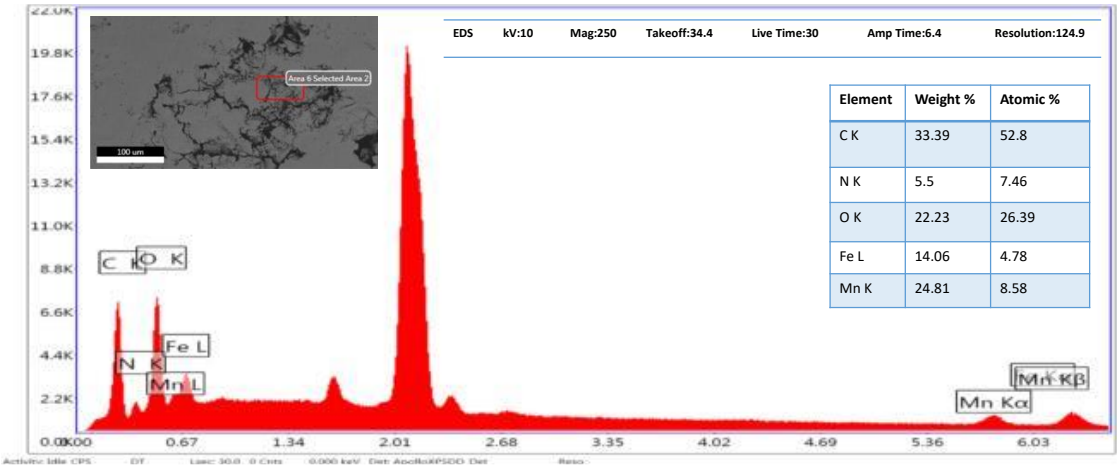

Figure 4.5 The energy dispersive X-Ray (EDX) Spectrum of $MnFe_2O_4$ Magnetic Nanoparticles on Multi-walled Carbon Nanotubes.

4.3.2 The Electromagnetic Properties of Composite Samples

The electromagnetic constitutive parameters were extracted using an Agilent PNA E8364B network analyzer (Keysight Tech.) in conjunction with a coaxial line system (Keysight Tech. 85050C 7mm coaxial connectors) at 2.4-18 GHz frequency range at room temperature. The real (ε_r' and μ_r') and the imaginary part (ε_r" and μ_r") of relative complex permittivity and permeability as well as the dielectric loss tangent (tan (δ_ε) =ε_r"/ε_r') and the magnetic loss tangent (tan (δ_μ) =μ_r"/ μ_r') for nano-structured composites were extracted with the help of the software (85071E Keysight Tech.), pre-installed in the network analyzer. The real part of relative complex permittivity and permeability are associated with the storage capability of electric and magnetic energies. The ε'' and μ'' are associated with energy loss within materials, resulting from dielectric and magnetic mechanisms such as conduction, resonance, interfaces, relaxation and atomic, electronic and/or dominant polarization.

The relative permittivity real part (ε'), the relative permeability real part (μ'), the dielectric loss tangent (tan $\delta\varepsilon = \varepsilon''/\varepsilon'$), and the magnetic loss tangent (tan $\delta\mu = \mu''/\mu'$) of manganese spinel ferrites blended with MWCNTs with different weight percentages are presented in Fig. 4.6. The weight percentages are namely in 25% increments of weight ratios (Table IX).

TABLE IX
THE PROPORTIONS USED FOR THE SAMPLE (MWCNTS WITH MSF NPS) PREPARATION

Sample Code	Proportions
1	75 wt % (MWCNTs) with 25 wt % ($MnFe_2O_4$)
2	50 wt % (MWCNTs) with 50 wt % ($MnFe_2O_4$)
3	25 wt % (MWCNTs) with 75 wt % ($MnFe_2O_4$)

In Fig. 4.6a and 4.6b, the ε′ values of the samples slightly decrease in the range of 10.4−1.1. The dielectric tangent loss slightly decreases in the range of 0.22-0.04 within the frequency range 2.0-8.3 GHz. It increases in the range of 0.04-0.16 within the frequency range 8.3-12.5 GHz. The dielectric tangent loss of the samples in the rest of the frequency range exhibits almost a constant value with only a small fluctuation. The constancy in the values of the real part of permittivity suggests that there was a dominant polarization, in which the oscillation of the electric dipole moments was in phase or somewhat out of phase with the microwave frequencies [96].

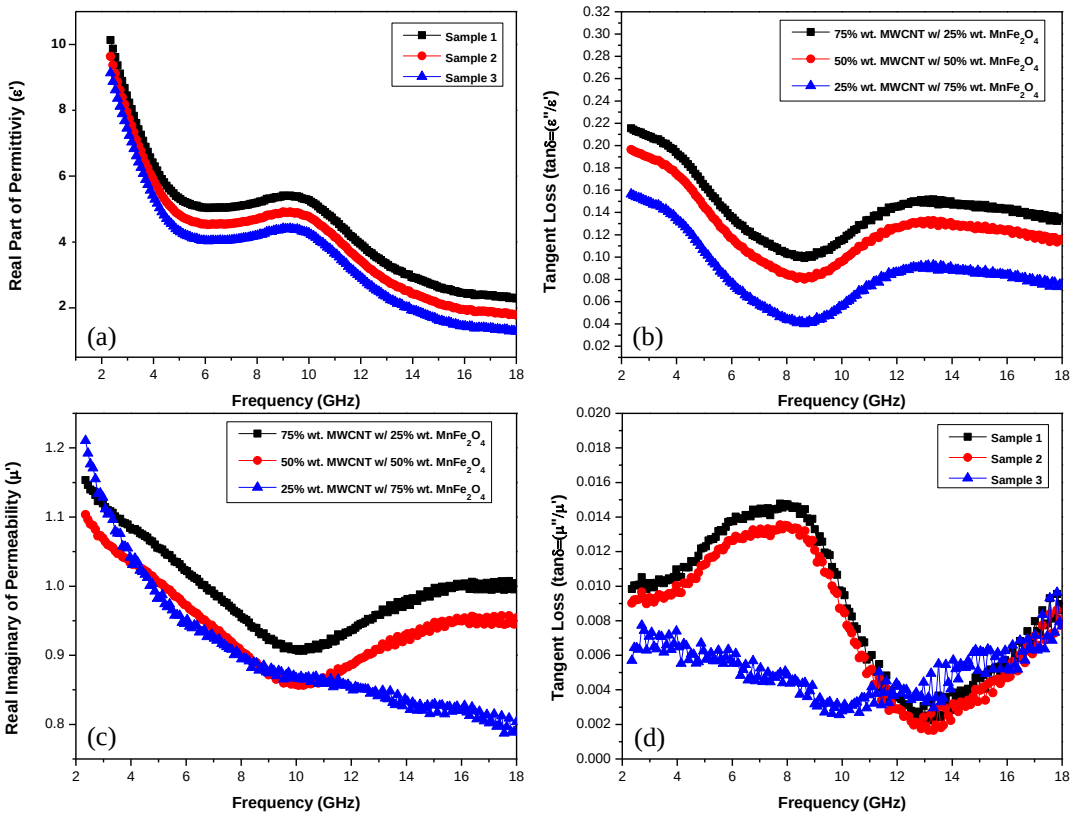

Figure 4.6 The electromagnetic constitutive parameters (a) the relative real part of permittivity (b) The Dielectric tangent loss of the samples, (c) the relative imaginary part of permeability (d) The Magnetic tangent loss of the samples, resulting from $MnFe_2O_4$ magnetic nanoparticles on multi-walled carbon nanotubes.

As demonstrated in Fig. 6c and d, we can observe that the μ′ values of the samples slightly decreased in the frequency range of 2-10 GHz, whereas its values increased between 10-18 GHz. The μ″ values (or tan δμ) of the samples indicate broad resonance peak in the whole frequency range, which is related to the small size effect, surface effect, and spin wave excitations [97].

It is observed that the tan δε values are higher than tan δμ, suggesting that the magnetic loss is low. MWCNTs are often used as an additive coating with manganese spinel ferrites to increase its conductivity [98]. According to the free-electron theory, increased conductivity of a composite could result in strong dielectric loss, and thus, the blend of MWCNTs and MSF NPs show a stronger dielectric loss in 2−18 GHz.

4.3.3 Microwave Absorption Properties

First, the results obtained by the previous waveguide[1] and the present coaxial-line methods over the common frequency range (8-12 GHz) are compared below in Fig. 4.7 and Table IX and show good agreement.

TABLE X
THE MICROWAVE ABSORPTION RESULTS

Code	**f_r (GHz)**		**Return Loss (dB)**		**Bandwidth (under −20 dB)**	
	Present Work	Previous Work	Present Work	Previous Work	Present Work	Previous Work
1	10.08	10.44	−34.07	-32.84	1.98 GHz	1.88 GHz
2	11.00	11.00	−45.16	-41.20	2.55 GHz	2.20 GHz
3	11.26	11.41	−53.31	-56.00	3.49 GHz	3.38 GHz

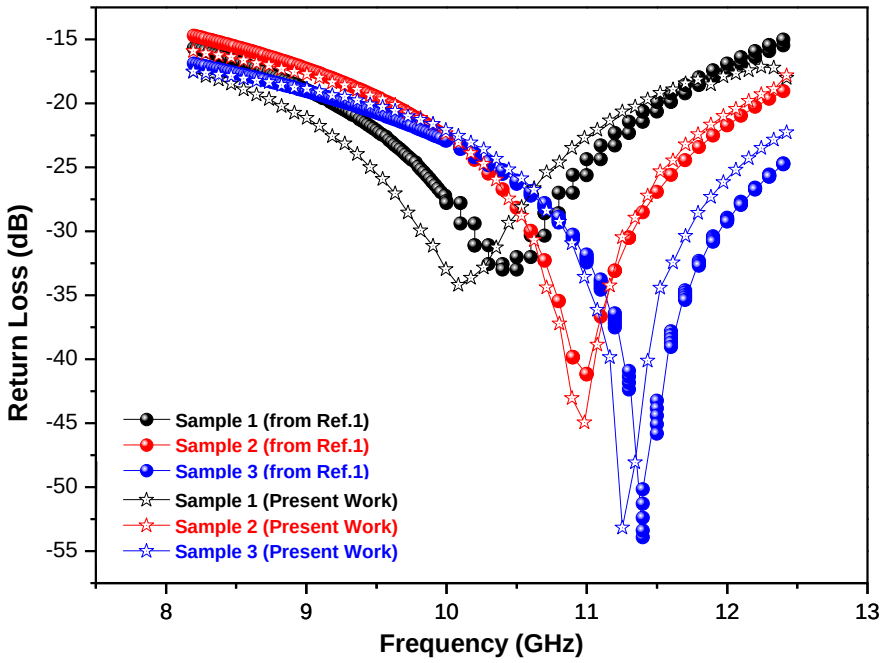

Figure 4.7 Comparison Return Losses of Coaxial Line and Waveguide Measurements in the frequency range of 8-12 GHz.

Fig. 4.8 presents the calculated return loss (RL) of the samples for the various compositions of additives over the frequency range 2-18 GHz. The samples thickness are approximately the same thickness (3 mm). It can be observed that the plots of RL versus frequency indicate good microwave absorption. The minimum RL values shifted to higher frequencies and the bandwidths increased with an increasing amount of manganese ferrite material in the mixture. The lowest RL value and the bandwidth change with different loadings of manganese and zinc spinel ferrite nanoparticles. A minimum RL of −53.31 dB at 11.26 GHz with a bandwidth of 3.49 GHz (RL < −20 dB) was obtained in MWCNTs with $MnFe_2O_4$ NPs.

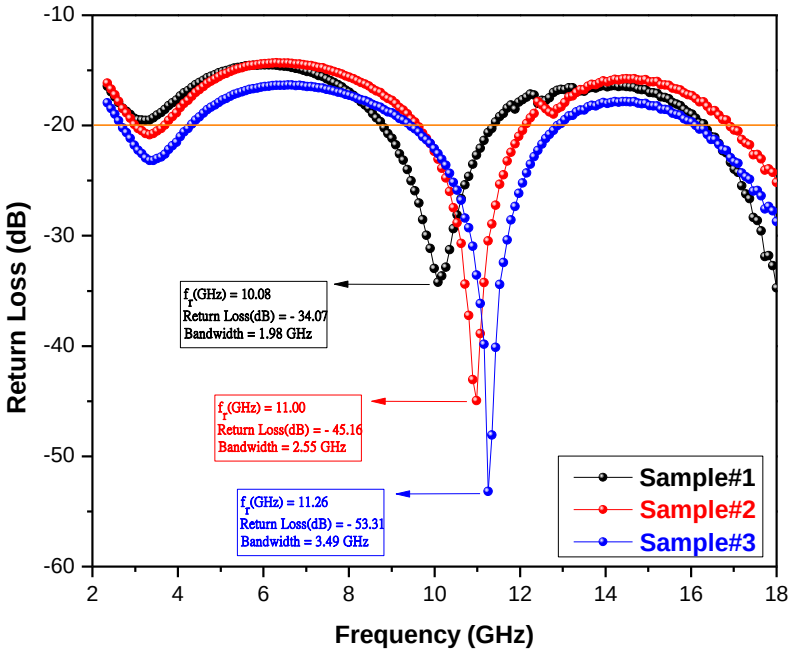

Figure 4.8 Return Loss versus frequency of MWCNTs with MSF NPs alloy with Coaxial Line Technique.

These comparison results are summarized in Table X, including the sample codes, the center frequencies (f_r), the values of minimum achievable return loss (dB), and the corresponding bandwidths (GHz).

4.4 Conclusion

Because of both dielectric and magnetic contributions to microwave absorption properties at microwave frequencies, the composite samples exhibited desirable microwave absorption properties in terms of the minimum RL values and the broad absorption bandwidths. The minimum RL value tends to shift to higher frequencies with an increasing amount of manganese ferrite material in the mixture.

5. Conclusion of Thesis

This work focused on developing radar absorbing materials (RAMs) based on nano-structured magnetic materials with the goal of contributing to a better understanding of the applications of flexible, reconfigurable, lightweight RAMs, which are camouflaging ground-based hardware against hostile airborne radar observation and enhancement of microwave absorption properties of the RAMs.

First, Polyacrylonitrile (PAN) textiles coated with different weight fractions of Ni-Co alloys using electroless metal deposition method are investigated. Deposition is performed with soluble metal salts. Reaction rare is contrilled by bath compositions and it runs fast enough to provide high throughput for industrial systems. Magnetic and higly conductive metals such as nickel and cobalt were selected for deposition due to their high stability and relatively simple deposition procedure. Metallic clusters are formed from ions attached to fiber by chemisorption with reducing in aqueous solution. XRD results confirmed the crystal structures with the existence of single Ni and Co phases, which are face-centered cubic (fcc) for the $Ni_{0.8}Co_{0.2}$ bath and hexagonal close-packed (hcp) for the $Ni_{0.2}Co_{0.8}$ bath. As expected, it was observed that, as the coating time increased, more metals resolved and deposited on the surface of PAN textiles in a solid state solution, and it was possible to transition from crystal clusters to smooth metallic coatings on PAN textiles. However, more crystal clusters mean highly ordered metallic coatings, which are not desirable for the broadband radar absorbing characteristics. The microwave absorption depends on coating time.

Second, Manganese and Zinc ferrites are synthesized using a citric acid assisted sol-gel method. Mn-Zn ferrites in/on MWCNTs with different weight ratios were

investigated to enhance microwave absorption properties (low reflection). All synthesized samples exhibited super-paramagnetic beahvior at room temperature as expected. XRD patterns are in good agreements with the JCPDS cards in the literature. No secondary impurity phase was detected. The return loss (RL) results indicated that microwave absorption of MWCNTs were enhanced by blending magnetic materials as expected. The significant finding of minimum reflection values shoed that the microwave absorption is about 99.99%.

Then, the microwave absorption properties of Mn-Zn ferrites in/on MWCNTs were measured using non-resonant methods including a waveguide and a coaxial line techniques in order to cross-validate the absroption results. The scattering parameters (s-parameters) of the RAMs were measured in the radar frequency bands by using a network analyzer. The electromagnetic constitutive parameters were computed from the measured s-parameters using Nicolson-Ross-Weir Algorithm (NRW) with the help of a MATLAB code. In addition, the return loss of the RAMs is estimated from the computed permittivity and permeability values.

The experimental results presented in this thesis are expected to encourage further development of magnetic nano-particle coated textile absorbers for broadband microwave absorber applications and to support a promising role for MWCNTs blended with ferrite nano-particles for broadband applications.

6. Appendices

6.1 Nicholson-Ross-Weir Technique

Microwave Absorption Measurement flow chart is exhibited in the Fig. A.1;

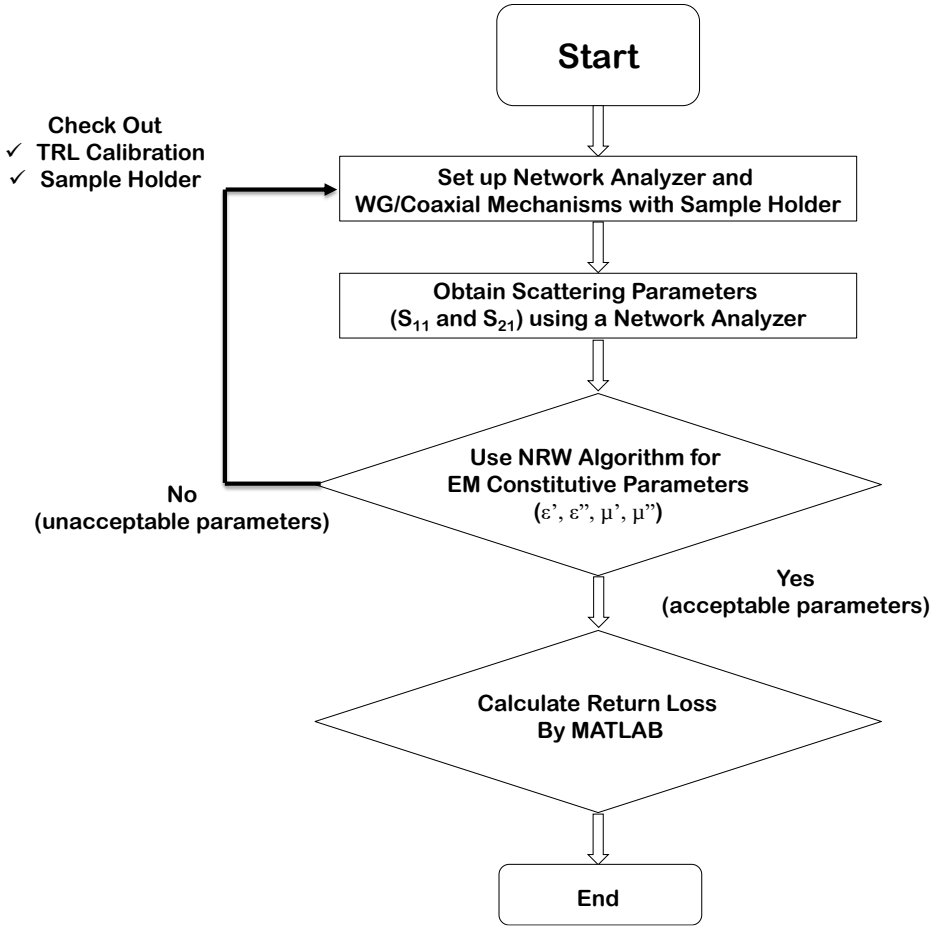

Figure A.1 Flow Chart of Microwave Absorption Measurements

Energy absorption in materials is due to their dielectric and magnetic properties depending on the ε_r (=ε'-jε") and μ_r (=μ'-jμ"). The real parts of the permittivity and permeability show the storage capability of electric and magnetic energy. The imaginary part of permittivity and permeability represent the loss of the dielectric and magnetic energy. S-parameters (S_{11} and S_{21}) are experimentally obtained by network analyzer between 2 ports. S_{11} parameter shows how much energy reflect by the material. S_{21}

parameter means how much energy pass through the material. Those two parameters are related to complex permittivity and permeability. It will be explained the measurement and calculation process in this flow chart in detail. First, we set up a vector network analyzer in conjunction with waveguide system including the samples. Before making microwave measurements we have to do calibration. It allows TRL calibration for this measurement. **Thru** calibration is to connect directly Port1 and Port2, **Reflect** Calibration is to connect metal plate with a high reflection coefficient to each port. **Line** calibration is to insert a short length of transmission line between port 1 and port 2. Then, It is followed the flow chart steps. NRW algorithm is used to calculate electromagnetic constitutive parameters. Then if we get acceptable EM constitutive parameters. Later, we keep going to calculate RL by MATLAB code. If not, we have to check it out the calibration and the sample holder if there is airgap between the sample and sample holder.

Nicholson-Ross-Weir (NRW) technique provides a direct calculation of both the complex relative permittivity and permeability from scattering parameters. The technique is applicable for waveguide and coaxial line methods. The measurement of reflection and transmission coefficient requires all four parameters of S_{11}, S_{21}, S_{22}, and S_{12} or a pair of S_{11}, S_{21} of the material under the test (MUT) to be measured [4]. The procedure for the NRW conversion process:

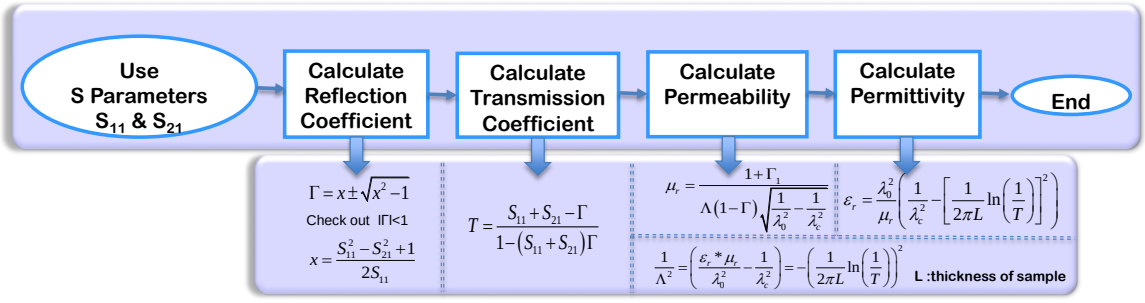

Figure A.2 Computation Steps of Nicholson-Ross-Weir Algorithm

The S_{11} and S_{21} parameters can be directly obtained by a vector network analyzer (VNA).

$$S_{11} = \frac{\Gamma\left(1-T^2\right)}{\left(1-\Gamma^2T^2\right)} \text{ and } S_{21} = \frac{T\left(1-\Gamma^2\right)}{\left(1-\Gamma^2T^2\right)} \tag{A.1}$$

The reflection coefficient can be deduced as $\Gamma = x \pm \sqrt{x^2-1}$ where $|\Gamma|\langle 1$ is required for finding the correct root and

$$x = \frac{S_{11}^2 - S_{21}^2 + 1}{S_{11}} \tag{A.2}$$

X factor can be defined by reflection coefficient (Γ);

$$\begin{aligned} \mathrm{x} &= \frac{1-(S_{21}^2 - S_{11}^2)}{2S_{11}} \\ &= \frac{1-\Gamma^2T^2 - T^2 + \Gamma^2}{2\left(1-T^2\right)\Gamma} = \frac{\Gamma^2\left(1-T^2\right)+\left(1-T^2\right)}{2\left(1-T^2\right)\Gamma} = \frac{\left(1-T^2\right)\left(\Gamma^2+1\right)}{2\left(1-T^2\right)\Gamma} \\ &= \frac{1+\Gamma^2}{2\Gamma} \end{aligned} \tag{A.3}$$

The transmission coefficient can be written by

$$T = \frac{S_{11} + S_{21} - \Gamma}{1-(S_{11}+S_{21})\Gamma} \tag{A.4}$$

The permeability is given as

$$\mu_r = \frac{1+\Gamma}{\Lambda(1-\Gamma)\sqrt{\frac{1}{\lambda_0^2} - \frac{1}{\lambda_c^2}}} \tag{A.5}$$

where λ_0 is free space wavelength and λ_c is cut-off wavelength of the transmission line section, and for a coaxial line $\lambda_c = \infty$.

$$\frac{1}{\Lambda^2} = \left(\frac{\varepsilon_r * \mu_r}{\lambda_0^2} - \frac{1}{\lambda_c^2}\right) = -\left(\frac{1}{2\pi L}\ln\left(\frac{1}{T}\right)\right)^2 \tag{A.6}$$

The permittivity can be defined as

$$\varepsilon_r = \frac{\lambda_0^2}{\mu_r\left[\left(1/\lambda_c^2\right)-\left(1/\Lambda^2\right)\right]} \tag{A.7}$$

6.2 Microwave Measurement System

6.2.1 A Vector Network Analyzer and Its Principles

A vector Network Analyzer (VNA) is an instrument that measures network parameters of electrical networks as a measurement of the reflection and/or transmission through a material with the help of its physical dimensions, according to the transmission line theory [25, 75]. That provides the information to characterize permittivity and permeability of a material.

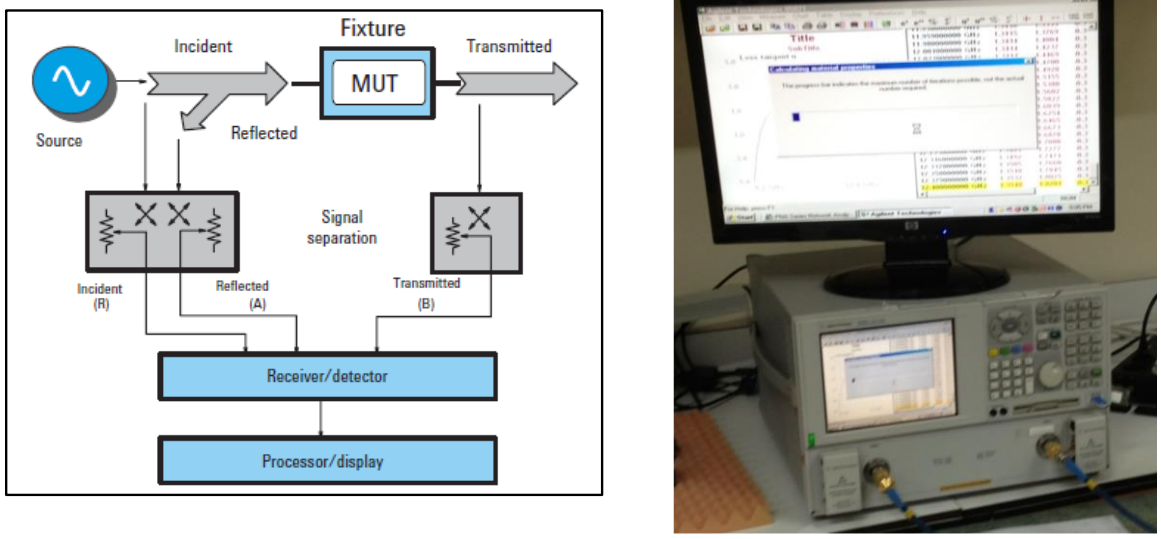

(a) (b)

Figure A.3 The Diagram of A Vector Network Analyzer (VNA)

A VNA consists of a signal generator, a receiver and a display. The generator sends a signal at a single frequency to the material. The receiver is tuned to that frequency to detect the reflected/transmitted signals from the material. The measured reaction produces

a magnitude and a phase data at the desired frequency. Then, its generator is stepped to the next frequency and the measurement is repeated to display the reflection/transmission measurement responses as a function of frequency. VNA can have different frequency ranges depending on model and manufacturer.

Agilent Technologies (Keysight Tech.) produces different type of dielectric measurements instruments. Frequency coverage versus the instrument are showed in Fig. A.3.

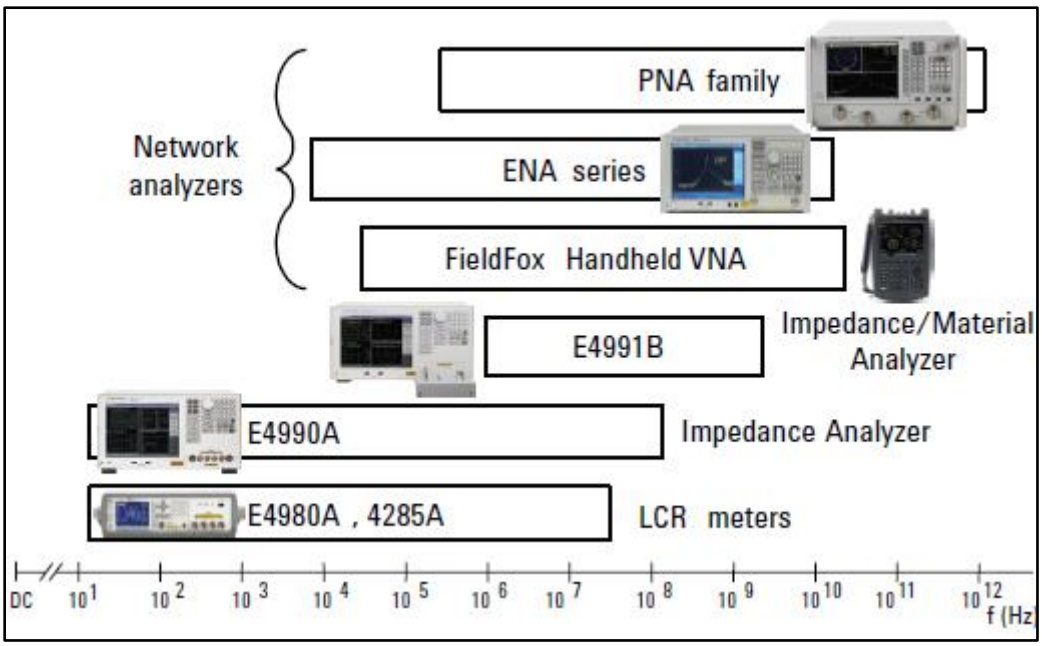

Figure A.4 The Frequency Coverage of Agilent Technologies Instruments.

The common VNA expressions has the incident wave measured with the R (for reference) receiver. The reflected wave is measured with the A receiver whereas the transmitted wave is measured with the B receiver. The reflection and transmission characteristics of material can be quantified with amplitude and phase information. The phase part is ignored or not measured (scalar in nature), while both magnitude and phase are measured (vector). For example, return loss is a scalar measurement of reflection,

while impedance results from a vector reflection measurement. Proportional reflection is often displayed as A/R and proportional transmission is often shown as B/R, relating to the measurement receivers used in the vector network analyzer (Fig. A.5).

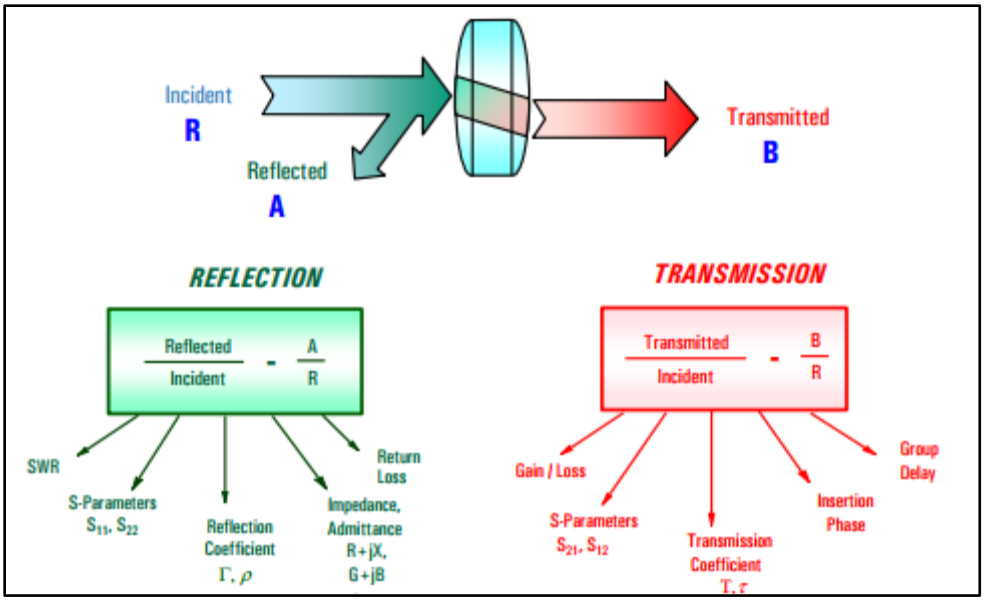

Figure A.5 The Network Analyzer Terminology with the parameters of reflection and transmission.

6.2.2 Software (Agilent 85071E)

The measured data from the VNA is not presented in the convenient format for microwave absorption properties. Therefore, software is required to convert the measured data of scattering parameters to permittivity and permeability. The Agilent Technologies 85071E materials measurement software determines the intrinsic electromagnetic properties of dielectric and magnetic materials. The measurement is based on the material` response to microwave energy. The divided screen and indicators assistance in data analysis. Results can be generated in variety formats of electromagnetic constitutive parameters and loss tangents values.

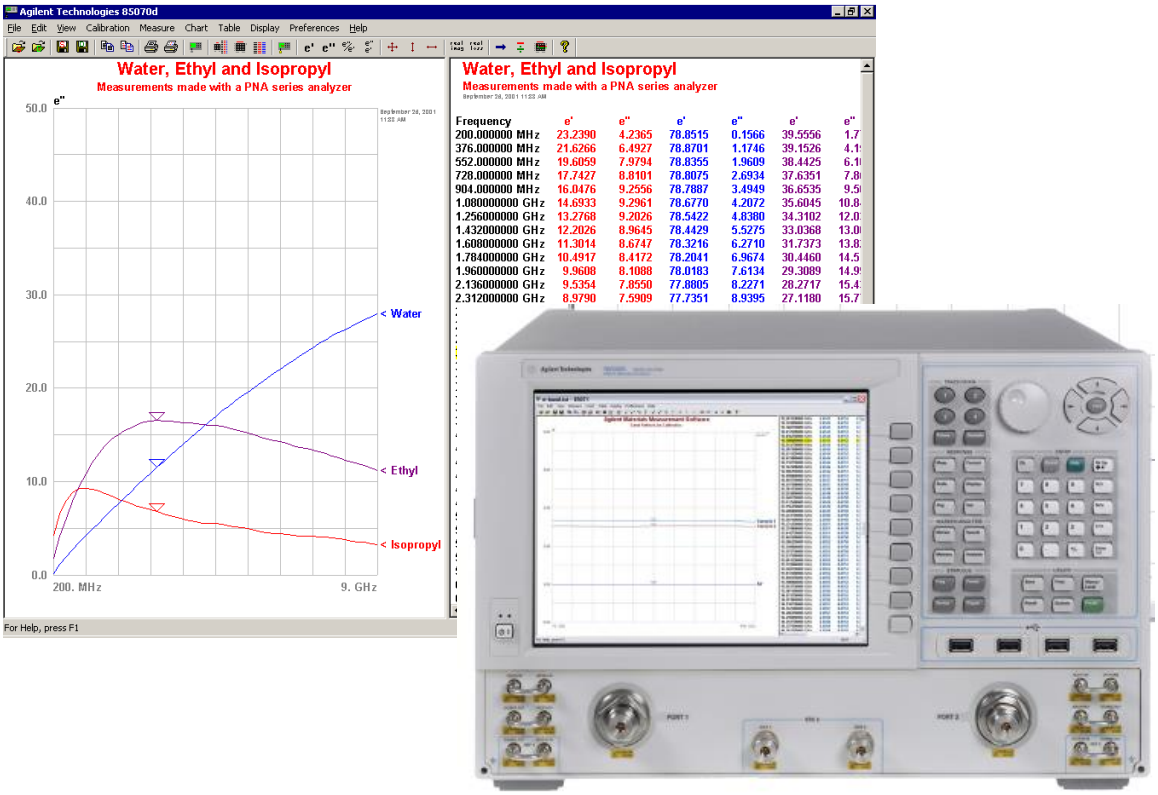

Figure A.6 85071E Materials Measurement Software

6.2.3 Scattering Parameters (s-parameters)

S-parameters are calculated using the transmitted and reflected wave values on a transmission line that connects a microwave circuit to an external circuit. S-parameters are used in such measurements, especially since current and voltage measurements cannot be made in the measuring instruments where waveguides are used.

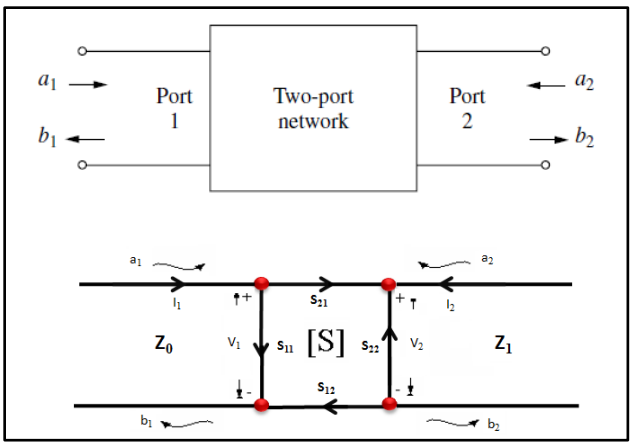

Figure A.7 A two-port network with "a" and "b" defined.

S-parameters can be calculated from the voltage values of the waves at the connection points once a two port linear circuit is placed in a transmission line as shown in Fig. A.7. The reflected and transmitted signals occur contrary to the stimulus signal from the source. The voltage values of the reflected and transmitted signal are calculated as follows:

$$V_1 = V_1^+ + V_1^- \qquad V_2 = V_2^+ + V_2^- \tag{A.8}$$

The current values (Eq. A.9) at these connection points are obtained from voltage values using the characteristic impedance (Z_0) of the transmission line:

$$I_1 = \frac{1}{Z_0}(V_1^+ - V_1^-)$$
$$I_2 = \frac{1}{Z_0}(V_2^+ - V_2^-) \tag{A.9}$$

where the impedance is typically 50 ohm in microwave circuits. The voltages values of transmitted and reflected wave can be substituted with Eq. A.8 and A.9 as Eq. A.10.

$$V_1^+ = \frac{V_1 + Z_0 I_1}{2}$$
$$V_2^+ = \frac{V_2 + Z_0 I_2}{2}$$
$$V_1^- = \frac{V_1 - Z_0 I_1}{2} \qquad \text{(A.10)}$$
$$V_2^- = \frac{V_2 - Z_0 I_2}{2}$$

When the incoming and reflected voltage values are normalized dividing by the square root of the characteristic impedance of the transmission line, the normalized voltage waveforms are obtained as follows in the variables a and b:

$$a_1 = \frac{V_1^+}{\sqrt{Z_0}} \ ,$$
$$a_2 = \frac{V_2^+}{\sqrt{Z_0}} \qquad \text{(A.11)}$$
$$b_1 = \frac{V_1^-}{\sqrt{Z_0}} \ , \ b_2 = \frac{V_2^-}{\sqrt{Z_0}}$$

S-parameters can be calculated using the normalized waveforms (Eq. A.11) from the following identities:

$$b_1 = S_{11} a_1 + S_{12} a_2$$
$$b_2 = S_{21} a_1 + S_{22} a_2 \qquad \text{(A.12)}$$

Eq. A.12 can be written by a matrix form:

$$\begin{bmatrix} b_1 \\ b_1 \end{bmatrix} = \begin{bmatrix} S_{11} & S_{12} \\ S_{21} & S_{22} \end{bmatrix} \begin{bmatrix} a_1 \\ a_2 \end{bmatrix} \qquad \text{(A.13)}$$

S-parameters are obtained for a two-port network given in Fig. A.7. If the reference plane where placed the transmission line and the characteristic impedance of the transmission line are known, the network can be fully characterized by the Eq. A.13.

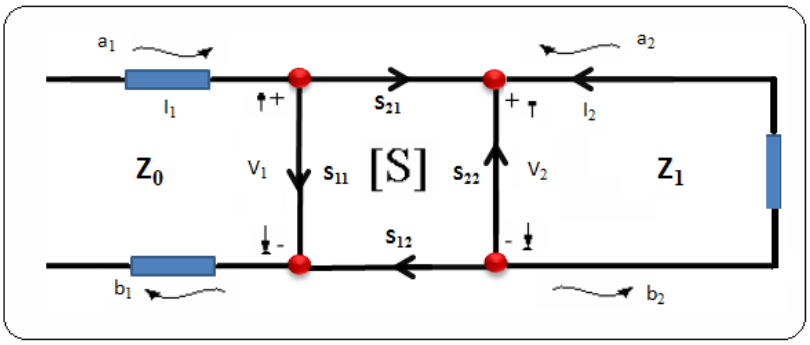

Figure A.8 A two-port network ended up a load.

In the network (Fig. A.7), the applied signal is fully consumed when an impedance of transmission line is equal to the Z_1 at port 2. Since there is no reflected signal $a_2=0$. Depending on that condition, the Eq. A.12 can be recalculated, then, S_{11} and S_{21} can be formatted as follows:

$a_2 = 0$ için; $$S_{11} = \frac{b_1}{a_1} \ , \ S_{21} = \frac{b_2}{a_1} \qquad \text{(A.14)}$$

The applied signal is fully consumed when an impedance of transmission line is equal to the Z_1 at port 1. Since there is no reflected signal $a_1=0$. Depending on that condition, the Eq. A.12 can be recalculated, then, S_{11} and S_{21} can be formatted as follows:

$a_1 = 0$ için; $$S_{22} = \frac{b_2}{a_2} \ , \ S_{12} = \frac{b_1}{a_2} \qquad \text{(A.15)}$$

6.2.4 Measurement Techniques

There are several measurement techniques to measure dielectric and magnetic properties of materials. Researchers need to know which technique is more appropriate for their materials.

Coaxial Probe

It is the best technique for the liquids and semi-solid (powder) materials. This technique is simple, convenient, non-destructive and with one measurement. The measurement system consists of a VNA or impedance analyzer, a coaxial probe and software. The acceptable frequency range of this technique is between 10 MHz and 50 GHz.

Transmission Line

It is a broadband technique for machine-able solids. It puts the material inside a portion of an enclosed transmission line. ε_r and μ_r are calculated from the measurement of the reflected signal (S_{11}) and transmitted signal (S_{21}). Materials assumptions can be listed as (i) Sample fills fixture cross section, (ii) No air gaps at fixture walls, (iii) Smooth, flat faces, perpendicular to long axis, (iv) homogeneous.

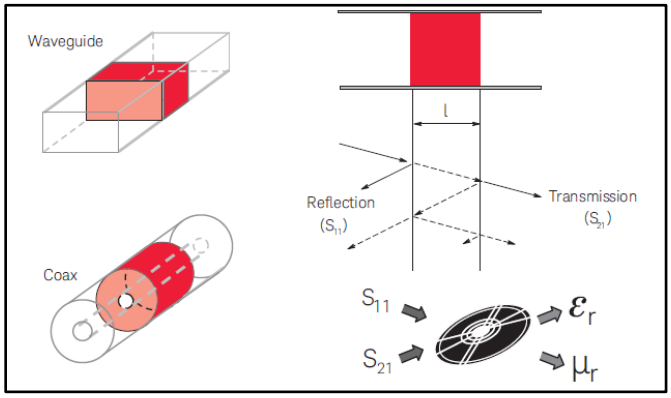

Figure A.9 Transmission Line Method; waveguide and coaxial line scenario

Figure A.10 Waveguide Measurement Setup (from lab)

Coaxial transmission line cover a broad frequency range, but a toroidal-shape sample is more difficult to manufacture. A typical measurement system using transmission line method consists of a VNA, a coaxial or waveguide transmission line and software to calculate permittivity and permeability.

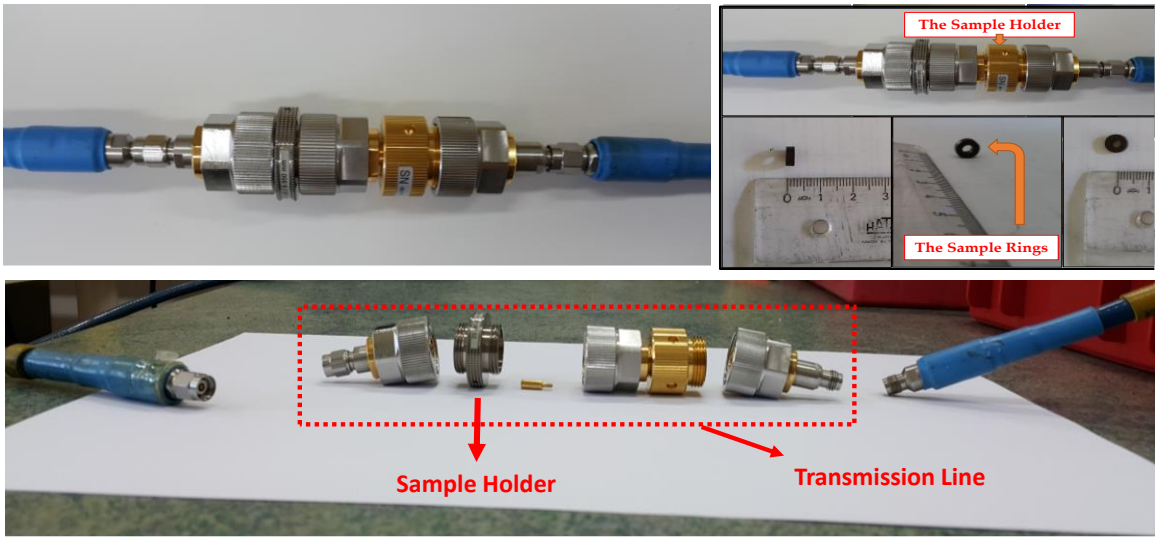

Figure A.11 Coaxial Line Measurement Setup (from lab)

Free-Space

Material assumptions are large scale, flat, parallel-faced samples. The technique features are non-contacting, non-destructive, high frequency-low end limited by practical sample size, useful for high temperature measurements, and measures magnetic materials. Free-Space techniques use antennas to focus microwave energy at the material. It has two typical setups: (i) S-parameter free space transmission configuration (ii) an NRL arch reflectivity configuration. A typical system consists of a VNA, convenient free space transmission reflectivity with the arch method, software.

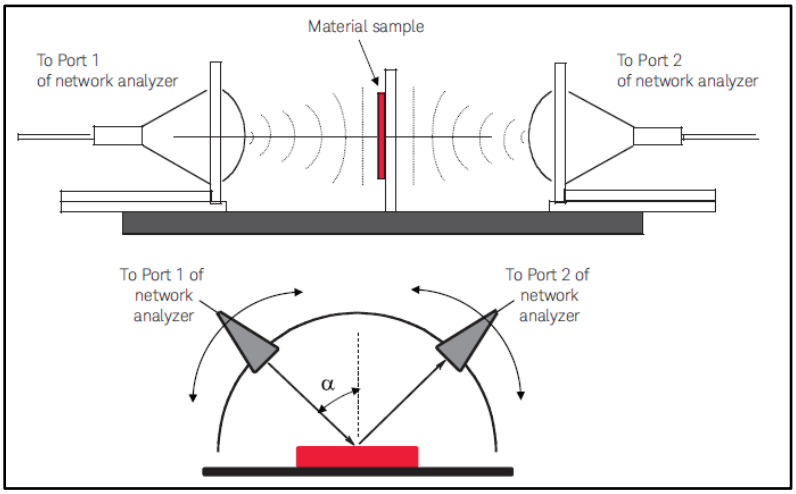

Figure A.12 Free-Space Measurement Setups

The manufactured NRL arch system is shown in Fig. A.13. It is geometrically designed depending on far field or near field conditions using different type of semi-circular cast polyamide material, which is one of the materials involved in polyamide group. It is manufactured by casting; it has a tight structure and hardness and low reflection values against to microwaves. Therefore, it is preferred to use for the arch system to make less reflection from the measurement environment.

Figure A.13 Free-Space Measurement Setups (from lab)

The other measurement techniques (Resonant Cavity, Parallel Plate, and Inductance measurement) are summarized in Fig. A.14.

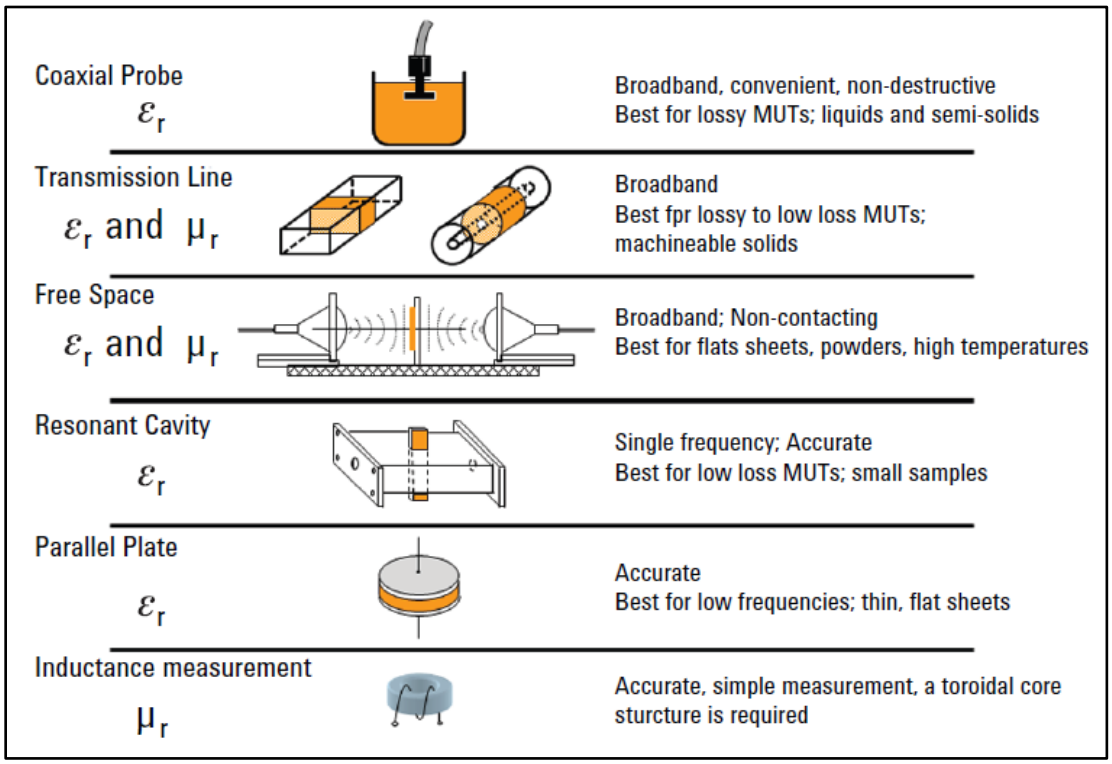

Figure A.14 A Summary of Measurement Techniques.

Bibliography

[1] G. Rao, S. Mahulikar, Integrated review of stealth technology and its role in airpower, The aeronautical journal. 106 (2002) 629-642.

[2] A. Teber, K. Cil, T. Yilmaz, B. Eraslan, D. Uysal, G. Surucu, A.H. Baykal, R. Bansal, Manganese and Zinc Spinel Ferrites Blended with Multi-Walled Carbon Nanotubes as Microwave Absorbing Materials, Aerospace. 4 (2017) 2.

[3] I. Specialty Materials, Manufacturers of Boron and SCS Silicon Carbide Fibers and Boron Nanopowder.

[4] L. Chen, C. Ong, C. Neo, V. Varadan, V.K. Varadan, Microwave electronics: measurement and materials characterization, John Wiley & Sons, 2004.

[5] P. Liu, Y. Huang, J. Yan, Y. Yang, Y. Zhao, Construction of CuS nanoflakes vertically aligned on magnetically decorated graphene and their enhanced microwave absorption properties, ACS applied materials & interfaces. 8 (2016) 5536-5546.

[6] Z. Wang, L. Wu, J. Zhou, W. Cai, B. Shen, Z. Jiang, Magnetite nanocrystals on multiwalled carbon nanotubes as a synergistic microwave absorber, The Journal of Physical Chemistry C. 117 (2013) 5446-5452.

[7] T. Giannakopoulou, L. Kompotiatis, A. Kontogeorgakos, G. Kordas, Microwave behavior of ferrites prepared via sol–gel method, J Magn Magn Mater. 246 (2002) 360-365.

[8] A. Jänis, R.T. Olsson, S. Savage, U.W. Gedde, U. Klement, Microwave absorbing properties of ferrite-based nanocomposites. 6526 (2007) 65261P.

[9] O. Akman, H. Kavas, A. Baykal, M.S. Toprak, A. Çoruh, B. Aktaş, Magnetic metal nanoparticles coated polyacrylonitrile textiles as microwave absorber, J Magn Magn Mater. 327 (2013) 151-158.

[10] L. Solymar, D. Walsh, Electrical properties of materials, OUP Oxford, 2009.

[11] W. Zachariasen, C. Kittel, Introduction to solid state physics (1966).

[12] A. Von Hippel, Dielectrics and Waves , Artech House, Inc., Norwood, MA (1995).

[13] S. Nelson, Dielectric properties measurement techniques and applications, Trans. ASAE. 42 (1999) 523.

[14] D.C. Jiles, Introduction to the electronic properties of materials, CRC Press, 2001.

[15] P. Robert, Electrical and magnetic properties of materials, Artech House Publishers, 1988.

[16] D. Jiles, Recent advances and future directions in magnetic materials, Acta Materialia. 51 (2003) 5907-5939.

[17] M. Tinkham, Introduction to superconductivity, Courier Corporation, 1996.

[18] M.E. Lines, A.M. Glass, Principles and applications of ferroelectrics and related materials, Oxford university press, 1977.

[19] M.I. Montrose, EMC and the printed circuit board: design, theory, and layout made simple, John Wiley & Sons, 2004.

[20] S. Ramo, J.R. Whinnery, T. Van Duzer, Fields and waves in communication electronics, John Wiley & Sons, 2008.

[21] C.A. Balanis, Advanced engineering electromagnetics, John Wiley & Sons, 1999.

[22] Agilent, Basics of Measuring the Dielectric Properties of Materials Application Note.

[23] E. Nyfors, P. Vainikainen, Industrial microwave sensors, Artech House Publishers, 1989.

[24] C. Brosseau, J.B. Youssef, P. Talbot, A. Konn, Electromagnetic and magnetic properties of multicomponent metal oxides heterostructures: Nanometer versus micrometer-sized particles, J. Appl. Phys. 93 (2003) 9243-9256.

[25] Y. Yin, M. Zeng, J. Liu, W. Tang, H. Dong, R. Xia, R. Yu, Enhanced high-frequency absorption of anisotropic Fe3O4/graphene nanocomposites, Scientific reports. 6 (2016) 25075.

[26] V. Bogush, Application of electroless metal deposition for advanced composite shielding materials, Journal of Optoelectronics and Advanced Materials. 7 (2005) 1635-1642.

[27] R.J.W. Donald, and M. Mardiguian, A Handbook Series on Electromagnetic Interference and Compatibility: Electromagnetic Shielding, Interference Control Technologies, ISBN-13:978-0944916032 . (1988).

[28] J.I. Duffy, M.W. Ranney, Electroless and other nonelectrolytic plating techni ques: recent developments, Noyes Data Corp., 1980.

[29] D. Tsai, S. Kim, T. Corrigan, R.J. Phaneuf, M.R. Zachariah, Electrostatic-directed deposition of nanoparticles on a field generating substrate, Nanotechnology. 16 (2005) 1856.

[30] V. Bogush, V. Glybin, L. Lynkov, Synthesis of inorganic nanoparticles in fiber polymers and their properties, Physics, Chemistry and Application of Nanostructures (1999) 251-254.

[31] A.V. Pandya, Study of the comparison of Conducting Behavior of doped Macromolecules and Semiconductors, Imperial Journal of Interdisciplinary Research. 2 (2016).

[32] L. Lynkov, V. Glybin, T. Selivyorstova, and V. Bogush, A method for ion-exchanging fibre material production. (2003).

[33] F.A. Lowenheim, Electroplating--Fundamentals of Surface Finishing, McGraw-Hill Book Co., New York.1978, 560 (1978).

[34] Y. Naito, K. Suetake, Application of ferrite to electromagnetic wave absorber and its characteristics, IEEE Trans. Microwave Theory Tech. 19 (1971) 65-72.

[35] N. Bensebaa, N. Loudjani, S. Alleg, L. Dekhil, J. Suñol, M. Al Sae, M. Bououdina, XRD analysis and magnetic properties of nanocrystalline Ni 20 Co 80 alloys, J Magn Magn Mater. 349 (2014) 51-56.

[36] A. Taylor, R.W. Floyd, Precision measurements of lattice parameters of non-cubic crystals, Acta Crystallogr. 3 (1950) 285-289.

[37] B. Cullity, Elements of X-ray Diffraction. Addison and Wesley Publishing Company Inc, Reading, USA (1978) 32-106.

[38] E. Jeon, Y. Cho, Mechanochemical synthesis and thermal decomposition of zinc borohydride, J. Alloys Compounds. 422 (2006) 273-275.

[39] M. Spasojević, L. Ribić-Zelenović, A. Maričić, The phase structure and morphology of electrodeposited nickel-cobalt alloy powders, Science of Sintering. 43 (2011) 313-326.

[40] L.D. Rafailović, D.M. Minić, Deposition and characterisation of nanostructured nickel–cobalt alloys, Hem.ind. 63 (2009) 557-569.

[41] R.W.G. Wyckoff, R.W. Wyckoff, Crystal structures, Interscience New York, 1960.

[42] Y. Li, L. Li, H. Liao, H. Wang, Preparation of pure nickel, cobalt, nickel–cobalt and nickel–copper alloys by hydrothermal reduction, Journal of Materials Chemistry. 9 (1999) 2675-2677.

[43] W.B. Weir, Automatic measurement of complex dielectric constant and permeability at microwave frequencies, Proc IEEE. 62 (1974) 33-36.

[44] A. Aslam, M. Islam, I. Ali, M. Awan, M. Irfan, A. Iftikhar, High frequency electrical transport properties of CoFe 2 O 4 and Sr 2 NiMnFe 12 O 22 composite ferrites, Ceram. Int. 40 (2014) 155-162.

[45] X. Liu, B. Li, D. Geng, W. Cui, F. Yang, Z. Xie, D. Kang, Z. Zhang, (Fe, Ni)/C nanocapsules for electromagnetic-wave-absorber in the whole Ku-band, Carbon. 47 (2009) 470-474.

[46] Z. Xie, D. Geng, X. Liu, S. Ma, Z. Zhang, Magnetic and microwave-absorption properties of graphite-coated (Fe, Ni) nanocapsules, Journal of Materials Science & Technology. 27 (2011) 607-614.

[47] X. Liu, Z. Ou, D. Geng, Z. Han, H. Wang, B. Li, E. Brück, Z. Zhang, Enhanced absorption bandwidth in carbon-coated supermalloy FeNiMo nanocapsules for a thin absorb thickness, J. Alloys Compounds. 506 (2010) 826-830.

[48] O. Akman, H. Kavas, A. Baykal, M.S. Toprak, A. Çoruh, B. Aktaş, Magnetic metal nanoparticles coated polyacrylonitrile textiles as microwave absorber, J Magn Magn Mater. 327 (2013) 151-158.

[49] H. Lin, H. Zhu, H. Guo, L. Yu, Investigation of the microwave-absorbing properties of Fe-filled carbon nanotubes, Mater Lett. 61 (2007) 3547-3550.

[50] T. Zou, H. Li, N. Zhao, C. Shi, Electromagnetic and microwave absorbing properties of multi-walled carbon nanotubes filled with Ni nanowire, J. Alloys Compounds. 496 (2010) L22-L24.

[51] Y. Qing, W. Zhou, F. Luo, D. Zhu, Epoxy-silicone filled with multi-walled carbon nanotubes and carbonyl iron particles as a microwave absorber, Carbon. 48 (2010) 4074-4080.

[52] J. Qiu, T. Qiu, Fabrication and microwave absorption properties of magnetite nanoparticle–carbon nanotube–hollow carbon fiber composites, Carbon. 81 (2015) 20-28.

[53] D. Zhang, F. Xu, J. Lin, Z. Yang, M. Zhang, Electromagnetic characteristics and microwave absorption properties of carbon-encapsulated cobalt nanoparticles in 2–18-GHz frequency range, Carbon. 80 (2014) 103-111.

[54] H. Lin, H. Zhu, H. Guo, L. Yu, Microwave-absorbing properties of Co-filled carbon nanotubes, Mater. Res. Bull. 43 (2008) 2697-2702.

[55] D. Shi, P. He, P. Zhao, F.F. Guo, F. Wang, C. Huth, X. Chaud, S.L. Bud'ko, J. Lian, Magnetic alignment of Ni/Co-coated carbon nanotubes in polystyrene composites, Composites Part B: Engineering. 42 (2011) 1532-1538.

[56] G. Liu, L. Wang, G. Chen, S. Hua, C. Ge, H. Zhang, R. Wu, Enhanced electromagnetic absorption properties of carbon nanotubes and zinc oxide whisker microwave absorber, J. Alloys Compounds. 514 (2012) 183-188.

[57] K.R. Paton, A.H. Windle, Efficient microwave energy absorption by carbon nanotubes, Carbon. 46 (2008) 1935-1941.

[58] M. Lu, W. Cao, H. Shi, X. Fang, J. Yang, Z. Hou, H. Jin, W. Wang, J. Yuan, M. Cao, Multi-wall carbon nanotubes decorated with ZnO nanocrystals: mild solution-process synthesis and highly efficient microwave absorption properties at elevated temperature, Journal of Materials Chemistry A. 2 (2014) 10540-10547.

[59] A. Teber, I. Unver, H. Kavas, B. Aktas, R. Bansal, Knitted radar absorbing materials (RAM) based on nickel–cobalt magnetic materials, J Magn Magn Mater. 406 (2016) 228-232.

[60] K. Khan, Microwave absorption properties of radar absorbing nanosized cobalt ferrites for high frequency applications, Journal of Superconductivity and Novel Magnetism. 27 (2014) 453-461.

[61] V. Sunny, P. Kurian, P. Mohanan, P. Joy, M. Anantharaman, A flexible microwave absorber based on nickel ferrite nanocomposite, J. Alloys Compounds. 489 (2010) 297-303.

[62] J. Xie, M. Han, L. Chen, R. Kuang, L. Deng, Microwave-absorbing properties of NiCoZn spinel ferrites, J Magn Magn Mater. 314 (2007) 37-42.

[63] D. Zhao, Q. Lv, Z. Shen, Fabrication and microwave absorbing properties of Ni–Zn spinel ferrites, J. Alloys Compounds. 480 (2009) 634-638.

[64] A.M. Gama, M.C. Rezende, C.C. Dantas, Dependence of microwave absorption properties on ferrite volume fraction in MnZn ferrite/rubber radar absorbing materials, J Magn Magn Mater. 323 (2011) 2782-2785.

[65] S.H. Hosseini, A. Asadnia, Synthesis, characterization, and microwave-absorbing properties of polypyrrole/MnFe 2 O 4 nanocomposite, Journal of Nanomaterials. 2012 (2012) 3.

[66] R. Sui, P. Charpentier, Synthesis of metal oxide nanostructures by direct sol–gel chemistry in supercritical fluids, Chem. Rev. 112 (2012) 3057-3082.

[67] L. Chen, C. Ong, C. Neo, V. Varadan, V.K. Varadan, Microwave electronics: measurement and materials characterization, John Wiley & Sons, 2004.

[68] I. U.S. Research Nanomaterials, The Advanced Nanomaterials Provider.

[69] D.P. Debecker, V. Hulea, P.H. Mutin, Mesoporous mixed oxide catalysts via non-hydrolytic sol–gel: a review, Applied Catalysis A: General. 451 (2013) 192-206.

[70] J. Feng, H. Zhang, Hybrid materials based on lanthanide organic complexes: a review, Chem. Soc. Rev. 42 (2013) 387-410.

[71] A. Demir, S. Güner, Y. Bakis, S. Esir, A. Baykal, Magnetic and optical properties of Mn1−xZnxFe2O4 nanoparticles, Journal of Inorganic and Organometallic Polymers and Materials. 24 (2014) 729-736.

[72] Agilent Literature, Agilent Basics of Measuring the Dielectric Properties of Materials, Application Note. .

[73] D. Micheli, R. Pastore, G. Giannini, A. Vricella, M. Marchetti, Low-cost low-observable satellites made of carbon nanostructured multilayers: Numerical investigation of scattering. (2013).

[74] D. Micheli, C. Apollo, R. Pastore, R.B. Morles, M. Marchetti, G. Gradoni, Electromagnetic characterization of composite materials and microwave absorbing modeling, in: Advances in nanocomposites-synthesis, characterization and industrial applications, InTech, 2011.

[75] D. Micheli, C. Apollo, R. Pastore, R.B. Morles, S. Laurenzi, M. Marchetti, Nanostructured composite materials for electromagnetic interference shielding applications, Acta Astronaut. 69 (2011) 747-757.

[76] G. Fang, Z. Chen, H. Li, Synthesis and properties of microencapsulated paraffin composites with SiO 2 shell as thermal energy storage materials, Chem. Eng. J. 163 (2010) 154-159.

[77] F. Gözüak, Y. Köseoğlu, A. Baykal, H. Kavas, Synthesis and characterization of CoxZn 1− xFe 2 O 4 magnetic nanoparticles via a PEG-assisted route, J Magn Magn Mater. 321 (2009) 2170-2177.

[78] K. Kanade, D. Amalnerkar, H. Potdar, B. Kale, Nanocrystalline Mn–Zn–ferrite by novel oxalato-hydrazinated complex method, Mater. Chem. Phys. 117 (2009) 187-191.

[79] S. Apte, S. Naik, R. Sonawane, B. Kale, J. Baeg, Synthesis of Nanosize-Necked Structure α-and γ-Fe2O3 and its Photocatalytic Activity, J Am Ceram Soc. 90 (2007) 412-414.

[80] G. Brahmachari, S. Laskar, P. Barik, Magnetically separable MnFe 2 O 4 nano-material: an efficient and reusable heterogeneous catalyst for the synthesis of 2-substituted benzimidazoles and the extended synthesis of quinoxalines at room temperature under aerobic conditions, RSC Advances. 3 (2013) 14245-14253.

[81] Z. Tang, C. Sorensen, K. Klabunde, G. Hadjipanayis, Size-dependent Curie temperature in nanoscale MnFe 2 O 4 particles, Phys. Rev. Lett. 67 (1991) 3602.

[82] T.M. Clark, B. Evans, Enhanced magnetization and cation distributions in nanocrystalline ZnFe/sub 2/O/sub 4: a conversion electron Mossbauer spectroscopic investigation, IEEE Trans. Magn. 33 (1997) 3745-3747.

[83] A. Jänis, R.T. Olsson, S. Savage, U.W. Gedde, U. Klement, Microwave absorbing properties of ferrite-based nanocomposites. 6526 (2007) 65261P.

[84] S.H. Ahmad, M.H. Abdullah, D. Hui, A.N. Yusoff, D. Puryanti, Magnetic and microwave absorbing properties of magnetite–thermoplastic natural rubber nanocomposites, J Magn Magn Mater. 322 (2010) 3401-3409.

[85] Y. Yin, M. Zeng, J. Liu, W. Tang, H. Dong, R. Xia, R. Yu, Enhanced high-frequency absorption of anisotropic Fe3O4/graphene nanocomposites, Scientific reports. 6 (2016) 25075.

[86] H. Zhao, Z. Fu, H. Chen, M. Zhong, C. Wang, Excellent electromagnetic absorption capability of Ni/carbon based conductive and magnetic foams synthesized via a green one pot route, ACS applied materials & interfaces. 8 (2016) 1468-1477.

[87] J. Xiang, J. Li, X. Zhang, Q. Ye, J. Xu, X. Shen, Magnetic carbon nanofibers containing uniformly dispersed Fe/Co/Ni nanoparticles as stable and high-performance electromagnetic wave absorbers, Journal of Materials Chemistry A. 2 (2014) 16905-16914.

[88] X. Liu, Z. Ou, D. Geng, Z. Han, J. Jiang, W. Liu, Z. Zhang, Influence of a graphite shell on the thermal and electromagnetic characteristics of FeNi nanoparticles, Carbon. 48 (2010) 891-897.

[89] H. Sözeri, Z. Mehmedi, H. Kavas, A. Baykal, Magnetic and microwave properties of BaFe 12 O 19 substituted with magnetic, non-magnetic and dielectric ions, Ceram. Int. 41 (2015) 9602-9609.

[90] Y. Naito, K. Suetake, Application of ferrite to electromagnetic wave absorber and its characteristics, IEEE Trans. Microwave Theory Tech. 19 (1971) 65-72.

[91] Z. Wang, L. Wu, J. Zhou, W. Cai, B. Shen, Z. Jiang, Magnetite nanocrystals on multiwalled carbon nanotubes as a synergistic microwave absorber, The Journal of Physical Chemistry C. 117 (2013) 5446-5452.

[92] T. Giannakopoulou, L. Kompotiatis, A. Kontogeorgakos, G. Kordas, Microwave behavior of ferrites prepared via sol–gel method, J Magn Magn Mater. 246 (2002) 360-365.

[93] Sotirios K. Goudos (Ed.), Microwave Systems and Applications, InTech, Chapters published January 11, 2017 under CC BY 3.0 license, 2017.

[94] A. Öztürk, R. Süleymanli, B. Aktaş, A. Teber, Propagation of microwaves in periodic layered media (2010) 4-7.

[95] A. Ozturk, R. Suleymanli, B. Aktas, A. Teber, Effect of Thin Metallic Layers on the Refractive Index of a Multilayer System, Chinese Physics Letters. 29 (2012) 027301.

[96] S. Abbas, A. Dixit, R. Chatterjee, T. Goel, Complex permittivity, complex permeability and microwave absorption properties of ferrite–polymer composites, J Magn Magn Mater. 309 (2007) 20-24.

[97] P. Liu, Y. Huang, J. Yan, Y. Yang, Y. Zhao, Construction of CuS nanoflakes vertically aligned on magnetically decorated graphene and their enhanced microwave absorption properties, ACS applied materials & interfaces. 8 (2016) 5536-5546.

[98] M. Wu, Y. Zhang, S. Hui, T. Xiao, S. Ge, W. Hines, J. Budnick, G. Taylor, Microwave magnetic properties of Co 50/(SiO 2) 50 nanoparticles, Appl. Phys. Lett. 80 (2002) 4404-4406.

[99] J. Luo, P. Shen, W. Yao, C. Jiang, J. Xu, Synthesis, characterization, and microwave absorption properties of reduced graphene oxide/strontium ferrite/polyaniline nanocomposites, Nanoscale research letters, 11 no:1 (2016) 141.